



VNIVERSITAT
DE VALÈNCIA

1

2 **Search for associated production of a Higgs**
3 **boson and a single top quark in $2\ell + \tau_{had}$**
4 **final state using proton-proton collisions**
5 **at $\sqrt{s} = 13$ TeV with the ATLAS detector**

6

PhD Thesis

7

Pablo Martínez Agulló

8

Instituto de Física Corpuscular (IFIC)
Departament de Física Atòmica, Molecular i Nuclear
Programa de Doctorat en Física

9

10

Under the supervision of

11

Carlos Escobar Ibáñez
and
Susana Cabrera Urbán

12

13

14

15

València, 5th May 2022

¹⁶ **Carlos Escobar Ibáñez,**
¹⁷ investigador científico del Consejo Superior de Investigaciones Científicas, y
¹⁸

¹⁹ **Susana Cabrera Urbán,**
²⁰ científica titular del Consejo Superior de Investigaciones Científicas,

²¹ **Certifican:**

²² Que la presente memoria, **Search for associated production of a**
Higgs boson and a single top quark in $2l + \tau_{had}$ final state
using proton-proton collisions at $\sqrt{s} = 13$ TeV with the ATLAS
detector, ha sido realizada bajo su dirección en el Instituto de Física
Corpuscular, centro mixto de la Universitat de València y del CSIC, por
Pablo Martínez Agulló, y constituye su Tesis para optar al grado de
Doctor en Física.

²⁹ Y para que así conste, en cumplimiento de la legislación vigente, presenta
³⁰ en el Departamento de Física Atómica, Molecular y Nuclear de la Univer-
³¹ sidad de Valencia la referida Tesis Doctoral, y firman el presente certificado.

³²

³³ València, a DD de MES de 2022,

³⁴

³⁵ Carlos Escobar Ibáñez

Susana Cabrera Urbán

36

37

38

39

C'est quoi ce bordel ???

—DANIEL BOSSON,

⁴⁰ Preface

⁴¹ The Standard Model of particle physics is both incredibly successful and
⁴² glaringly incomplete. Among the questions left open is the striking imbalance
⁴³ of matter and antimatter in our universe, which inspires experiments to
⁴⁴ compare the fundamental properties of matter/antimatter conjugates with
⁴⁵ high precision.

⁴⁶ The discovery of a Higgs boson by the ATLAS and CMS experiments in
⁴⁷ 2012 opened a new field for exploration in the realm of particle physics.

- ⁴⁸ - ttbar sensitive to the y_t module
- ⁴⁹ - thq sesntive to the sign

⁵⁰ Poner algo bonito del top y el Higgs

⁵¹ The top quark is the heaviest elementary particle discovered so far, with
⁵² a mass of $m_{top} = 172.76 \pm 0.30$ GeV [1], followed by the Higgs boson, with
⁵³ $m_H = 125.25 \pm 0.17$ GeV [2].

⁵⁴ This thesis describes the search for the associated production of a Higgs
⁵⁵ boson and a single top quark (tHq) in the final state with three leptons,
⁵⁶ being two of them light leptons (e/μ) and the other one a hadronically-
⁵⁷ decaying tau quark (τ_{had}). The examined channel is referred as $2\ell + 1\tau_{had}$
⁵⁸ and is further divided in two sub-channels attending to the relative electric
⁵⁹ charge between the light leptons ($2\ell SS + 1\tau_{had}$ and $2\ell OS + 1\tau_{had}$). The
⁶⁰ research carried targets SM Higgs bosons decaying to $H \rightarrow \tau\tau$, $H \rightarrow WW$
⁶¹ and $H \rightarrow ZZ$.

⁶² This analysis uses an integrated luminosity of 139 fb^{-1} of proton-proton
⁶³ collision data at centre-of-mass energy of 13 TeV collected by ATLAS during
⁶⁴ LHC Run 2. The ATLAS detector is one of the four detectors at the Large
⁶⁵ Hadron Collider (LHC) of the European Organization for Nuclear Research
⁶⁶ (CERN).

⁶⁷ This analysis presents a great challenge due to the difficulty of distinguishing
⁶⁸ the tHq production in the $2\ell + 1\tau_{had}$ channels from other SM processes
⁶⁹ with much higher cross-sections. The tHq process has an extremely small

70 cross-section (70 fb at 13 TeV) and the $2\ell + 1\tau_{\text{had}}$ channel accounts only for
71 the 3.5% of the total production.

72 In order to help separating the signal events for the background pro-
73 cesses that mimic the $2\ell + 1\tau_{\text{had}}$ signature a reconstruction of the events is
74 approached by determining the information about the top quark first and
75 the Higgs boson secondly. This is a complex task due the presence of, at
76 least, four neutrinos in the final state that difficult determining the linear
77 momentum of both the top quark and Higgs boson.

78 Additional studies are carried to assign origin the light-flavoured leptons,
79 i.e. whether these came form the Higgs boson or the top quark. To do so,
80 a gradient boosted decision tree is used.

81 Moreover, due to the arduousness of separating the the tHq from the
82 backgrounds, multivariate techniques are used. With them are defined
83 signal-enriched regions and control regions to constrain the most important
84 background processes, which are those related to top-quark-antiquark-pair
85 production ($t\bar{t}$, $t\bar{t}H$, $t\bar{t}W$ and $t\bar{t}Z$) and Z boson plus jets.

86 The possible observation of a an excess of signal events with respect to
87 the Standard Model predictions, would be a clear evidence of new physics
88 in terms of \mathcal{CP} -violating Yukawa couplings between the top quark and the
89 Higgs boson.

90 Furthermore, other channels (defined by their final state) are being stud-
91 ied in the context of tHq research

92 During this thesis the “god-given” units are used. In this system (name
93 natural system) the Planck constant and the speed of light have the same
94 magnitude and dimensions ($\hbar = c = 1$), implying that:

$$95 \quad [\text{length}] = [\text{time}] = [\text{energy}]^{-1} = [\text{mass}]^{-1}.$$

96 In the international system (SI) units, the values are $\hbar = 1.055 \times 10^{-34}$ Js
97 and $c = 2.998 \times 10^8$ m/s. An exception is made for the Chapter 2, where
98 the SI is used for describing the design of the LHC and ATLAS.

99 **Conceptos triviales que también debería introducir en**
100 **algún momento [http://opendata.atlas.cern/books/current/
101 get-started/_book/GLOSSARY.html](http://opendata.atlas.cern/books/current/get-started/_book/GLOSSARY.html)**

¹⁰² **Acknowledgements**

¹⁰³ This work would not have been possible without the invaluable help of a
¹⁰⁴ large number of people, whom I have been fortunate to meet, and to whom
¹⁰⁵ I would like to thank and dedicate this thesis.

¹⁰⁶ Gracias gracias

¹⁰⁷ Contents

¹⁰⁸	Preface	v
¹⁰⁹	Acknowledgements	vii
¹¹⁰	1 Theoretical Framework	1
¹¹¹	1.1 The Standard Model of particle physics	1
¹¹²	1.1.1 Introduction to the SM and its elementary particles	2
¹¹³	1.1.2 Quantum electrodynamics	6
¹¹⁴	1.1.3 Electroweak interactions	8
¹¹⁵	1.1.4 Quantum chromodynamics	15
¹¹⁶	1.1.5 Particle masses	19
¹¹⁷	1.1.6 Charge-Parity	26
¹¹⁸	1.1.7 Wrap up	26
¹¹⁹	1.2 Top quark	32
¹²⁰	1.2.1 Top quark discovery	34
¹²¹	1.2.2 Top quark production at LHC	35
¹²²	1.2.3 Top quark decay	41
¹²³	1.2.4 Top quark polarisation	44
¹²⁴	1.2.5 Top quark physics	45
¹²⁵	1.3 Higgs boson	46
¹²⁶	1.3.1 Higgs boson discovery	46
¹²⁷	1.3.2 Higgs boson production at LHC	46

128	1.3.3	Higgs boson decay	48
129	1.3.4	Higgs boson physics	49
130	1.4	Top quark and Higgs boson interplay	50
131	1.4.1	$t\bar{t}H$	51
132	1.4.2	tHq	52
133	2	The ATLAS experiment at the Large Hadron Collider of CERN laboratory	57
134	2.1	CERN	57
135	2.2	Large Hadron Collider	59
136	2.2.1	Machine design	59
137	2.2.2	Accelerator complex	63
138	2.2.3	LHC Experiments	64
139	2.2.4	LHC Computing grid	67
140	2.2.5	Energy, Luminosity and Cross-section	69
141	2.2.6	The Pile-up effect	74
142	2.2.7	Phenomenology of proton-proton collisions	75
143	2.3	ATLAS	79
144	2.3.1	Coordinate system	82
145	2.3.2	Inner Detector	83
146	2.3.3	Calorimeters	88
147	2.3.4	Muon Spectrometer	93
148	2.3.5	Magnet system	95
149	2.3.6	Trigger and Data Acquisition System	98
150	2.3.7	ATLAS upgrade towards HL-LHC	99
151	2.4	Alignment of the inner detector	104
152	2.4.1	Alignment requirements	104
153	2.4.2	Track based alignment	104
154	2.4.3	Alignment results during Run-2	104
155	2.4.4	Alignment towards Run-3	104

157	3 Data and simulated events and object reconstruction	105
158	3.1 Data	105
159	3.2 Monte Carlo	105
160	3.2.1 MC simulations	106
161	3.2.2 MC generators	106
162	3.3 Object reconstruction and identification	106
163	3.3.1 Tracking	107
164	3.3.2 Vertices	108
165	3.3.3 Electrons and photons	108
166	3.3.4 Muons	108
167	3.3.5 Jets	108
168	3.3.6 Missing transverse energy	109
169	3.3.7 Overlap removal	109
170	4 Probing the top-quark polarisation in the single-top t-channel production	111
171		
172	4.1 Introduction	111
173	4.2 Top quark polarisation observables	112
174	4.3 Simulated event samples	112
175	4.4 Object reconstruction	112
176	4.5 Trigger requirements and event preselection	112
177	4.6 Top quark reconstruction	112
178	5 Search for rare associate tHq production	113
179		
180	5.1 Introduction	113
181	5.2 Data and simulated events	114
182	5.3 Object definition and reconstruction	115
183	5.4 Signal	115
184	5.4.1 Signal generation and validation	115
	5.4.2 Parton-level truth validation	115

185	5.4.3 Lepton assignment	115
186	5.4.4 Top quark and Higgs boson reconstruction	120
187	5.5 Background estimation	120
188	5.5.1 Fakes estimation	120
189	5.5.2 Prompt backgrounds	121
190	5.6 Event selection	122
191	5.6.1 Preselection	122
192	5.6.2 BDT	122
193	5.6.3 Signal Region	123
194	5.6.4 Control Regions	123
195	5.7 Systematic uncertainties	124
196	5.7.1 Theoretical uncertainties	124
197	5.7.2 Modelling uncertainties	124
198	5.7.3 Experimental uncertainties	124
199	5.8 Fit results	124
200	5.8.1 Likelihood fit	124
201	5.8.2 Strategy	126
202	5.8.3 Fit with Asimov data	126
203	5.8.4 Fit to data	126
204	5.8.5 Results	126
205	5.8.6 Data fit	126
206	5.9 Combination results	126
207	5.10 Conclusions	126
208	6 Conclusion	127
209	A Effect of negative weights	129
210	A.1 Negative weights uncertainties	129
211	A.2 Statistical uncertainty of negative weights	129
212	A.2.1 Errors in binned histograms	131

213	A.3 Negative weights in MVA methods	132
214	Appendices	128
215	B Boosted Decision Tree	133
216	B.1 Intro	133
217	B.2 How does a BDT work	133
218	B.2.1 Training	133
219	B.2.2 Evaluation	133
220	B.2.3 Overtraining	134
221	B.2.4 Application	135
222	B.3 Treatment of negative weights	135
223	B.4 Cross validation and k -folding	135
224	Abbreviations	138
225	Bibliography	141
226	Summary of the results	155
227	Resum de la tesi	157
228	1 Marc teòric	157
229	1.1 El Model Estàndard	157
230	1.2 La física del quark top	157
231	1.3 La física del bosó de Higgs	157
232	2 L'experiment ATLAS del LHC al CERN	157
233	2.1 El gran col·lisionador d'hadrons	157
234	2.2 El detector ATLAS	157
235	3 Mesura de la polarització del quark top al canal- t	157
236	3.1 Selecció d'esdeveniments	158
237	3.2 Estimació del fons	158

238	3.3	Fonts d'incertesa	158
239	3.4	Resultats	158
240	4	Recerca de processos tH amb un estat final $2\ell + 1\tau_{\text{had}}$	158
241	4.1	Selecció d'esdeveniments	158
242	4.2	Estimació del fons	158
243	4.3	Fonts d'incertesa	158
244	4.4	Resultats	158
245	5	Conclusions	158

²⁴⁶ Chapter 1

²⁴⁷ Theoretical Framework

²⁴⁸ 1.1 The Standard Model of particle physics

²⁴⁹ Since the very first moment of our history, the humankind has pursued
²⁵⁰ the knowledge of nature, has tried to understand and describe how the
²⁵¹ universe works at a fundamental level. In fact, the word physics comes
²⁵² from the Greek “*φυσική*” which means “nature” [3][4]. Most of the enquires
²⁵³ regarding this, can be boiled down to two basic questions: What are the
²⁵⁴ ultimate building blocks of reality? and which are the rules that govern
²⁵⁵ them?

²⁵⁶ In the 7th century BCE, the pre-Socratic philosopher Thales of Miletus
²⁵⁷ already proclaimed that every event had a natural cause [5]. Later, to un-
²⁵⁸ derstand how the basic components of the matter were formed, the ancient
²⁵⁹ Indian philosophers such as Kanada and Dignaga on the 6th century BCE
²⁶⁰ and Greeks Democritus and Leucippus on the 5th century BCE, developed
²⁶¹ the atomism, which comes from “*ατομον*” meaning uncuttable or indivisible
²⁶² [6][7].

²⁶³ From then to our days, the search for the minute fragments that comprise
²⁶⁴ the matter and its interactions has led us to the Standard Model (SM) of
²⁶⁵ particle physics, one of the most successful scientific theories cultivated
²⁶⁶ so far. This understanding of the universe can explain phenomena from
²⁶⁷ behaviour of atoms to how stars burn.

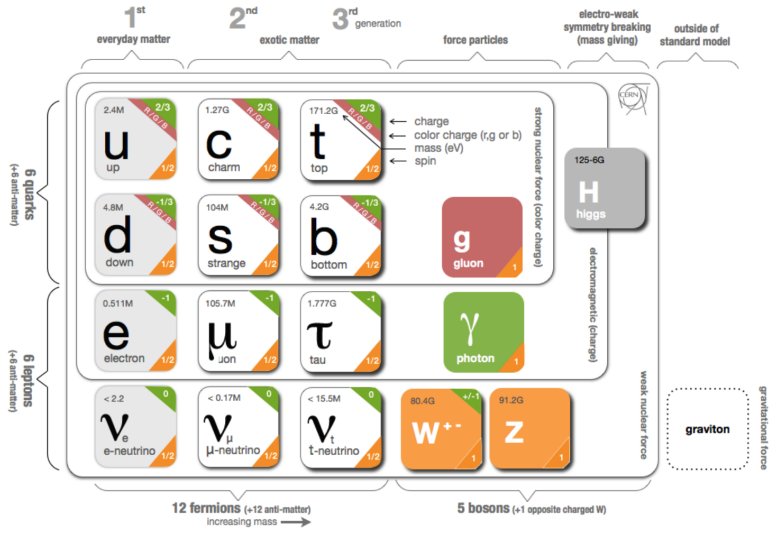


Figure 1.1: Fundamental particles of the Standard Model.

268 1.1.1 Introduction to the SM and its elementary 269 particles

270 Based on Quantum Field Theory (QFT), the SM of particle physics
271 provides the theoretical framework that constitutes what is currently ac-
272 cepted as the best description of particles physics. It aims to explain both
273 all particles of matter and their interactions. The completion of the SM
274 was a collaborative effort of several scientists during the second half of the
275 20th, being the current formulation finalised in the decade of 1970. A rep-
276 resentation of the fundamental particles, i.e. particles that are not made
277 of anything else, that compose the SM is presented in Figure 1.1. Most of
278 these particles are unstable and decay to lighter particles within fractions
279 of a second. As the scheme in Figure 1.1 indicates, the 12 fermions have
280 their corresponding 12 anti-fermions and the quarks and gluons carry colour
281 charge.

282 The SM is a gauge theory based on the symmetry group
283 $SU(3)_C \otimes SU(2)_L \otimes U(1)_Y$, which describes all fundamental interactions
284 except from the gravitational force¹. This theory provides an explana-
285 tion to strong, weak and electromagnetic interactions via the exchange of
286 the corresponding vector² bosons (spin-1 gauge fields). The mediation for
287 the electromagnetic interaction (explicated in 1.1.2) is done by one mass-
288 less photon (γ), this force is invariant under the $U(1)$ symmetry group.

¹The gravitational interaction is described by Einstein's General Relativity (GR) [8].

²“Vector bosons” refer to all bosons that have spin 1 in contrast to the “scalar boson’s” which have spin 0.

Interaction	Theory	Mediator	Relative strength	Range (m)
Strong	QCD	g	1	10^{-15}
Electromagnetic	QED/EW	γ	$1/137$	∞
Weak	EW	W^\pm, Z	10^{-6}	10^{18}
Gravitational	GR	-	6×10^{-39}	∞

Table 1.1: Typical strength of the fundamental interactions with respect to the strong interaction. Here the strength is understood as the coupling constant. In GR the gravitational interaction is not a force but the effect of the four-dimensional spacetime curvature and, hence, it has no mediator in this formalism.

While for the weak interactions, guided by $SU(2)$, three massive bosons, W^+ , W^- and Z , act as mediators ($m_{W^\pm} = 80.385 \pm 0.015$ GeV and $m_Z = 91.1876 \pm 0.02$ GeV). Although the electromagnetic and weak interactions seem completely different at low energies, they are two aspects of the same force and can be described simultaneously by the $SU(2)_L \otimes U(1)_Y$ symmetry group, which represents the so called Electro-Weak (EW) sector (detailed in Section 1.1.3). The strong force, with its 8 massless gluons (g), is described by the $SU(3)_C$ colour group (see Section 1.1.4). All these interactions differ in their magnitude, range and the physical phenomena that describe. These features are summarised in Table 1.1, where not only the interactions of the SM are included but the gravitation is as well.

Apart from the vector bosons, there is one massive scalar boson, the Higgs boson ($m_H = 125.25 \pm 0.17$ GeV). Through the interaction with this particle, all massive particles of Figure 1.1 gain their mass via the EW spontaneous symmetry breaking. This mechanism is described in Section 1.1.5.1.

Before describing the fundamental interactions of the SM in the QFT formalism, let's introduce the main two types of particles according to their spin, i.e. intrinsic angular momentum: fermions and bosons.

308 Fermions

The fermions are the particles that follow the Fermi-Dirac statistics, i.e. obey the Pauli exclusion principle [9], resulting in a distribution of particles over energy levels in which two elements with the same quantum numbers cannot occupy the same states. The fermions include all particles with half-integer spin: quarks, leptons and baryons. A baryon is a non-fundamental particle composed of an odd number of valence quarks³ (consequently hav-

³The hadrons (baryons are mesons) are understood as a sea of partons being the valence quarks those which are more probable to be found in the hadron according to the parton distribution functions.

ing half-integer spin) and nearly all matter that may be encountered or experienced in everyday life is baryonic matter. Some examples of baryons are⁴ the proton ($u\ u\ d$), the neutron ($d\ d\ u$), Λ ($u\ d\ s$), Λ_c^+ ($u\ d\ c$) and Σ^+ ($u\ u\ s$). Apart from the 3-quark baryons, an exotic pentaquark state has been observed at LHCb experiment of the LHC [10].

The fundamental fermionic matter (Table 1.2) is organised in the three families of leptons and quarks:

$$\begin{bmatrix} \nu_e & u \\ e^- & d \end{bmatrix}, \begin{bmatrix} \nu_\mu & c \\ \mu^- & s \end{bmatrix}, \begin{bmatrix} \nu_\tau & t \\ \tau^- & b \end{bmatrix}$$

.

These three generations, which are defined as the columns in Figure 1.1, exhibit the same kind of gauge interactions and they only differ in their mass [11]. According to the EW symmetry, each family can be classified as:

$$\begin{bmatrix} \nu_\ell & q_u \\ \ell^- & q_d \end{bmatrix} \equiv \begin{pmatrix} \nu_\ell \\ \ell^- \end{pmatrix}_L, \begin{pmatrix} q_u \\ q_d \end{pmatrix}_L, \ell^-_R, q_{uR}, q_{dR}$$

(plus the corresponding antiparticles) where the subindices L and R stand from left and right handed particles respectively. This structure responds to the fact that left-handed particles convert different than right-handed ones under $SU(2)$ transformations. The left-handed fields are $SU(2)_L$ doublets and the right-handed ones $SU(2)_R$ singlets. This difference is explained with more detail in Section 1.1.3.

The fundamental representation of $SU(3)$ is a triplet, this is why each quark can appear in three different colours, whereas each antiquark can exhibit one of the corresponding “anticolours”.

The SM fermions properties are summarised in Table 1.2. As can be seen in its last rows, the neutrino flavour states do no correspond to the mass states (ν_1, ν_2, ν_3). What happens is that each flavour state is a quantum mechanical combination of neutrinos of different masses and viceversa. More details about the neutrino masses can be found in a dedicated text in Section 1.1.7.2

The fundamental fermions are usually understood as the fundamental building blocks of matter. However, while the building blocks are important, there is a point that also has to be taken into account, the force. Without force these fermions would not interact which each other. The particles that mediate these interactions are the gauge bosons.

⁴Between round brackets, the valence quarks are shown.

Family	Name	Mass	Q
Quarks	Up (u)	$2.16^{+0.49}_{-0.26}$ MeV	2/3
	Down (d)	$4.67^{+0.48}_{-0.17}$ MeV	-1/3
	Charm (c)	1.27 ± 0.02 GeV	2/3
	Strange (s)	93^{+11}_{-5} MeV	-1/3
	Top (t)	172.76 ± 0.30 GeV	2/3
	Bottom (b)	$4.18^{+0.03}_{-0.02}$ GeV	-1/3
Leptons	Electron (e^-)	$0.5109989461 \pm 0.0000000031$ MeV	-1
	Muon (μ)	$105.6583745 \pm 0.0000024$ MeV	-1
	Tau (τ)	776.86 ± 0.12 MeV	-1
	Electron neutrino (ν_e)	ν_e, ν_μ, ν_e	0
	Muon neutrino (ν_μ)	\neq	0
	Tau neutrino (ν_τ)	ν_1, ν_2, ν_3	0

Table 1.2: Properties of the quarks and leptons. The electric charge is represented here by Q. The ν_1, ν_2, ν_3 are the neutrino mass eigenstates.

348 **Bosons**

349 Bosons differ from fermions by obeying the Bose-Einstein statistics, thus,
 350 bosons are not limited to single occupancy for a determined state. In other
 351 words, the Pauli exclusion principle is not applied. All particles with integer
 352 spin are bosons; from the particles shown on the right columns of Figure 1.1
 353 to the mesons. Mesons, along with baryons, are part of the hadron family,
 354 i.e. particles composed of quarks (see Section 1.1.4). The particularity
 355 of mesons is that they are formed from an equal number of quarks and
 356 antiquarks (usually one of each) bound together by strong interactions.
 357 Some examples of mesons are π^+ ($u \bar{d}$), π^0 ($\frac{u\bar{u}-d\bar{d}}{\sqrt{2}}$), K^+ ($u \bar{s}$) and J/ψ
 358 ($c \bar{c}$).

359 The elementary vector bosons are the force carriers and presented in
 360 Table 1.1 while Higgs boson is a fundamental particle as well.

361 **Gauge Invariance**

362 Constituting one of the most successful theories of Physics, the SM is able
 363 to provide an elegant mathematical framework to describe the experimental
 364 physics results with great precision. Another key element to understand the
 365 SM is the concept of gauge invariance. As it is illustrated during the rest of
 366 the Section 1.1, by demanding that the Lagrangian remains invariant under
 367 local gauge transformations, the existence of the SM force-carrier bosons
 368 (γ, W^+, W^-, Z and g).

369 1.1.2 Quantum electrodynamics

370 The gauge invariance refers to the invariance of a theory under trans-
371 formations which the theory is said to posses internal symmetry. The trans-
372 formations which are applied in all space-time locations simultaneously are
373 known as “global” transformations while the ones that vary from one point
374 to another are “local”. Each local symmetry is the basis of a gauge theory
375 and requires the introduction of its own gauge bosons as it is discussed in
376 the following pages.

In QFT, particles are described as excitations of quantum fields that satisfy the corresponding mechanical field equations. The Lagrangians in QFT are used analogous to those of classical mechanics, where the equation of motion can be derived from the Lagrangian density function (\mathcal{L}) and the Euler-Lagrange equations for fields:

$$\frac{\partial \mathcal{L}}{\partial \phi} - \partial_\mu \frac{\partial \mathcal{L}}{\partial (\partial_\mu \phi)} = 0$$

377, where $\partial_\mu = \frac{\partial}{\partial x^\mu}$ denotes the partial derivatives with respect to the four-
378 vector x^μ and $\phi = \phi(\vec{x}, t)$ is the quantum field of a fermion or boson. The
379 Lagrangian density (or just Lagrangian, for simplicity) is used to express
380 the dynamics of the quantum field. In QFT, Noether’s theorem [12] relates
381 a symmetry in the \mathcal{L} to a conserved current.

382 The Dirac equation, $(i\gamma^\mu \partial_\mu - m)\Psi(x) = 0$, is one of the simplest relativistic field equations. Its Lagrangian describes a free Dirac fermion:

$$\mathcal{L}_0 = i\bar{\Psi}(x)\gamma^\mu \partial_\mu \Psi(x) - m\bar{\Psi}(x)\Psi(x) \quad (1.1)$$

384, being Ψ the wave function (spinor represented by four complex-valued
385 components) of the particle, γ^μ are the Dirac or gamma matrices,
386 $\{\gamma^0, \gamma^1, \gamma^2, \gamma^3\}$, m the mass of the fermion and $\bar{\Psi} = \Psi^\dagger \gamma^0$, the hermitic
387 conjugate of the wave function. The gamma matrices build a set of ortho-
388 gonal basis vectors for covariant vectors in a Minkowski space. The first
389 term of \mathcal{L}_0 is the kinetic term while the second is the mass term.

This Lagrangian is invariant under $U(1)$ global transformations such as:

$$\Psi(x) \xrightarrow{U(1)} \Psi'(x) \equiv \exp\{iQ\theta\}\Psi(x) \quad (1.2)$$

390, where $Q\theta$ is a real constant. The phase of $\Psi(x)$ is a pure convention-
391 dependent quantity without a physical meaning since the observables de-
392 pend on $|\Psi(x)|^2$.

However, if θ was x dependent, the transformation 1.2 would be:

$$\Psi(x) \xrightarrow{U(1)} \Psi'(x) \equiv \exp\{iQ\theta(x)\}\Psi(x) \quad (1.3)$$

, which is not longer a global transformation but a local transformation instead. The transformation in 1.3 would not let the \mathcal{L}_0 in 1.1 invariant because the derivative in the kinetic term would go as:

$$\partial_\mu \Psi(x) \xrightarrow{U(1)} \exp\{iQ\theta\}(\partial_\mu + iQ\partial_\mu\theta)\Psi(x) \quad (1.4)$$

393 .

The gauge principle is the requirement that the $U(1)$ phase invariance should hold locally. In order to do so, it is necessary to introduce an additional term to the Lagrangian so that when one applies $\Psi'(x) \equiv \exp\{iQ\theta(x)\}\Psi(x)$, the $\partial_\mu\theta$ term is canceled in 1.4. To achieve this invariance, a term with the vector gauge field A_μ is inserted. This field transforms as

$$A_\mu(x) \xrightarrow{U(1)} A'_\mu(x) \equiv A_\mu(x) + \frac{1}{e}\partial_\mu\theta \quad (1.5)$$

with a new covariant derivative:

$$D_\mu\Psi(x) \equiv [\partial_\mu + ieQA_\mu(x)]\Psi(x) \quad (1.6)$$

which transforms like the field:

$$D_\mu\Psi(x) \xrightarrow{U(1)} (D_\mu\Psi)'(x) \equiv \exp\{iQ\theta\}D_\mu\Psi(x)$$

394 .

The Lagrangian density can be defined by replacing the partial derivatives in \mathcal{L}_0 (1.1) by the covariant derivative in 1.6:

$$\begin{aligned} \mathcal{L}_{QED} &\equiv i\bar{\Psi}(x)\gamma^\mu D_\mu\Psi(x) - m\bar{\Psi}(x)\Psi(x) \\ &= i\bar{\Psi}(x)\gamma^\mu[\partial_\mu + ieQA_\mu(x)]\Psi(x) - m\bar{\Psi}(x)\Psi(x) \\ &= i\bar{\Psi}(x)\gamma^\mu\partial_\mu\Psi(x) - \bar{\Psi}(x)\gamma^\mu eQA_\mu\Psi(x) - m\bar{\Psi}(x)\Psi(x) \\ &= \mathcal{L}_0 - eQA_\mu\bar{\Psi}(x)\gamma^\mu\Psi(x) \end{aligned} \quad (1.7)$$

395 .

396 The resulting Lagrangian is invariant under $U(1)$ local transformation.
 397 When the conversions 1.3 and 1.5 take place, the effects of the transformation
 398 are canceled out. Along with the original Lagrangian (\mathcal{L}_0), the \mathcal{L}_{QED}
 399 has an additional term describing the interaction between the fermion Ψ
 400 and the gauge field A_μ with a strength proportional to the charge eQ . This
 401 term, $eQA_\mu\bar{\Psi}\gamma^\mu\Psi$, that has been generated only by demanding the gauge
 402 invariance under $U(1)$, is not other than the vertex of Quantum Electrodynamics
 403 (QED) (Figure 1.2).

This new A_μ term is the electromagnetic field and its quanta is the photon. A mass term containing $A^\mu A_\mu$ is forbidden because it would violate

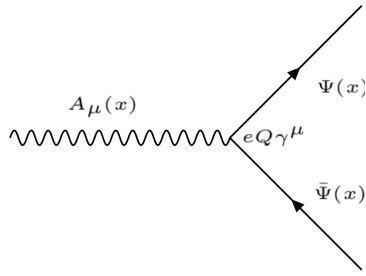


Figure 1.2: Three-point interaction vertex of QED.

the $U(1)$ local invariance. In consequence, the mediator of the new A_μ field, the photon, is predicted to be a massless particle. To make A_μ a propagating field it is necessary to add the kinetic term of the field A_μ :

$$\mathcal{L}_{kin} \equiv -\frac{1}{4}F_{\mu\nu}(x)F^{\mu\nu}(x) \quad (1.8)$$

, where $F^{\mu\nu} \equiv \partial_\mu A_\nu - \partial_\nu A_\mu$. The kinetic term $F_{\mu\nu}F_{\mu\nu}F^{\mu\nu}$ is already invariant under local $U(1)$ phase transformations. From the QED Lagrangian in 1.7 and the kinetic term in 1.8, the Maxwell equations can be derived to describe electromagnetism, the infinite range⁵ interaction that occurs between particles with electrical charge. The \mathcal{L}_{QED} with this kinetic term is written as:

$$\mathcal{L}_{QED} = \bar{\Psi}(x)(i\gamma^\mu\partial_\mu - m)\Psi(x) - eQ\bar{\Psi}(x)\gamma^\mu A_\mu\Psi(x) - \frac{1}{4}F_{\mu\nu}(x)F^{\mu\nu}(x) \quad (1.9)$$

404 1.1.3 Electroweak interactions

405 1.1.3.1 Weak interactions and Symmetries

406 The weak interaction is mediated by the W^+ , W^- and Z massive gauge
 407 bosons. Due their large mass ($m_{W^\pm} = 80.4$ GeV and $m_Z = 91.2$ GeV), the
 408 range of the interactions is restricted to $\sim 10^{-18}$ m. It is responsible for
 409 radioactive decays, nuclear fusions and flavour changing⁶ decays of fermions
 410 such as the decay of the muon ($\mu^- \rightarrow e^-\bar{\nu}_e\nu_\mu$).

411 Another particularity of this interaction is that it is the only interaction
 412 that violates several fundamental symmetries. There is a relation between
 413 symmetries and conservations laws which is known as Noether's theorem.
 414 Classical physics examples of how the symmetries leads to conserved quant-
 415 ities are:

⁵Since the photon is (predicted to be) massless, the electromagnetic interaction has an infinite range.

⁶The leptonic charges are conserved.

- ⁴¹⁶ • Invariance under change of time → Conservation of energy
⁴¹⁷ • Invariance under translation in space → Conservation of momentum
⁴¹⁸ • Invariance under rotation → Conservation of angular momentum

⁴¹⁹ The three discrete symmetries that are fundamental for the SM formulation and are always hold for electromagnetic and strong interactions are:

- **Charge conjugation (\mathcal{C}):** Replace positive quantum charges by negative charges and vice versa. It does not affect mass, energy, momentum or spin. Essentially, it is a transformation that switches all particles with their corresponding antiparticles.

$$\mathcal{C}\Psi(\vec{r}, t) = \bar{\Psi}(\vec{r}, t)$$

- **Parity (\mathcal{P}):** Parity involves a transformation that changes the algebraic sign of the spatial coordinate system. It does not reverse time, mass, energy or other scalar quantities.

$$\mathcal{P} : \begin{pmatrix} x \\ y \\ z \end{pmatrix} \rightarrow \begin{pmatrix} -x \\ -y \\ -z \end{pmatrix} \quad \mathcal{P}\Psi(\vec{r}, t) = \Psi(-\vec{r}, t)$$

- **Time reversal (\mathcal{T}):** Consists in flipping the sign of the time

$$\mathcal{T} : t \rightarrow -t \quad \mathcal{T}\Psi(\vec{r}, t) = \Psi(\vec{r}, -t)$$

⁴²¹ The simultaneous combination of this three symmetries mentioned above
⁴²² results in the \mathcal{CPT} symmetry, a profound symmetry of QFT which is
⁴²³ consistent through all experimental observations [13]. Meanwhile, the \mathcal{P} -
⁴²⁴ symmetry and the \mathcal{C} -symmetry can be combined to create the \mathcal{CP} -symmetry,
⁴²⁵ the product of the two transformations. The weak interaction violates \mathcal{P}
⁴²⁶ and \mathcal{C} symmetries. It also violates the combined \mathcal{CP} -symmetry. Therefore,
⁴²⁷ through the CPT theorem [14], if the \mathcal{CP} is violated, \mathcal{T} is violated as well
⁴²⁸ to preserve the \mathcal{CPT} invariance [15].

⁴²⁹ Parity and Charge conjugation violation

⁴³⁰ Previously theorised by Lee and Yang [16], the confirmation of the non-
⁴³¹ conservation of \mathcal{P} in weak interactions arrived with the Wu experiment in
⁴³² 1957 [17]. Studying the beta decay of the Cobalt-60, Wu and collaborators
⁴³³ found that the neutrino and the antineutrino have the relative orientations
⁴³⁴ of spin and linear momentum fixed. The neutrino spin is always opposite

435 to the linear momentum, this is called left-handed particles. Meanwhile, for
436 the antineutrinos, the momentum is always aligned in the same direction as
437 the spin (right-handed particles). This causes the weak interactions which
438 emit neutrinos or antineutrinos to violate the conservation of parity.

Only left-handed particles and right-handed antiparticles are sensitive to the weak force. Dirac fermion fields, ψ , exhibit chiral symmetry and the right and left handed chiral states can be expressed as:

$$\psi_L(x) = \frac{1}{2}(1 - \gamma_5)\psi(x) \equiv P_L\psi(x) \quad (1.10)$$

$$\psi_R(x) = \frac{1}{2}(1 + \gamma_5)\psi(x) \equiv P_R\psi(x) \quad (1.11)$$

with

$$\gamma^5 \equiv \gamma_5 \equiv \gamma^0\gamma^1\gamma^2\gamma^3 = \begin{pmatrix} 1 & 0 \\ 0 & 1 \end{pmatrix}$$

439 where P_L and P_R are known as projection operators. The last equality is
440 valid in the Dirac representation.

441 In the same year, the \mathcal{C} violation was found too [18]. **Describe how**
442 **the \mathcal{C} violation was discovered**

443 \mathcal{CP} violation

444 While \mathcal{P} and \mathcal{C} are violated in a maximal way by the weak interactions,
445 the product of these two discrete transformations, \mathcal{CP} , is still a good sym-
446 metry (left-handed fermions \leftrightarrow right-handed fermions). Experiences such
447 as the Wu experiment respect the \mathcal{CP} symmetry and, in fact, in the \mathcal{CP} is a
448 symmetry of nearly all the observed phenomena. However, in 1964 Cronin
449 and Fitch discovered a slight (2%) violation of the \mathcal{CP} symmetry in the
450 decays of neutral kaons [19]. The \mathcal{CP} violation plays a fundamental role to
451 explain the dominance of matter over antimatter in the present universe.
452 More information about the matter-antimatter asymmetry can be found in
453 the dedicated text in Section 1.1.7.2.

454 Direct \mathcal{CP} violation is allowed in the SM if a complex phase is present
455 in the CKM matrix (described below). The “direct” \mathcal{CP} violation is a phe-
456 nomenon where the same decay process has a different probability for a
457 particle than for an antiparticle. An example of strong global \mathcal{CP} asy-
458 mmetry observed corresponds to the decay into two kaons and one pion. The
459 probability of $B^+ \rightarrow \pi^+ K^+ K^-$ is 20% higher than for $B^- \rightarrow \pi^- K^+ K^-$.

CKM matrix

The eigenstates that interact through weak interactions, known as “weak

eigenstates” (d' , s' , u'), are different from the the physically observed mass eigenstates (d , s , u). This make possible the charged-flavour-changing-weak decays trough the Cabibbo-Kobayashi-Maskawa (CKM) matrix. The CKM matrix, V_{CKM} , describes the mixing between the three generations of quarks in the SM. The coupling of two quarks i and j to a W boson is proportional to the CKM matrix element V_{ij} .

$$\begin{pmatrix} d' \\ s' \\ u' \end{pmatrix} = \begin{pmatrix} V_{ud} & V_{us} & V_{ub} \\ V_{cd} & V_{cs} & V_{cb} \\ V_{td} & V_{ts} & V_{tb} \end{pmatrix} \begin{pmatrix} d \\ s \\ u \end{pmatrix} \quad (1.12)$$

It is a 3×3 unitary matrix described by four independent parameters: three angles (θ_{ij}) and one phase (δ_{13}). Different equivalent representations of the CKM matrix can be found in literature but the Particle Data Group recommends the standard CKM parameterisation:

$$V_{CKM} = \begin{pmatrix} c_{12}c_{13} & -s_{12}c_{13} & s_{13}e^{-i\delta_{13}} \\ -s_{12}c_{23} - c_{12}s_{23}s_{13}e^{i\delta_{13}} & -c_{12}c_{23} - s_{12}s_{23}s_{13}e^{i\delta_{13}} & s_{23}c_{13} \\ s_{12}s_{23} - c_{12}c_{23}s_{13}e^{i\delta_{13}} & -c_{12}s_{23} - s_{12}c_{23}s_{13}e^{i\delta_{13}} & c_{23}c_{13} \end{pmatrix} \quad (1.13)$$

where $c_{ij} \equiv \cos \theta_{ij}$ and $s_{ij} \equiv \sin \theta_{ij}$, with i and j labelling the generations ($i, j \in \{1, 2, 3\}$). The angles θ_{12} , θ_{23} and θ_{13} are known as Euler angles. The complex phase δ_{13} allows the \mathcal{CP} violation [20]. There are other popular parameterisations such as the Kobayashi-Maskawa one or the Wolfenstein one.

The different elements of the CKM matrix are determined experimentally and are summarised in Table 1.3. As can be seen in this table, the largest values correspond to the diagonal elements of the CKM matrix. This implies that the processes that do not change the flavour are strongly preferred over the family-changing charged currents. For instance, for the top quark, the decay to any of the three down-type quarks is allowed but only $|V_{td}|^2 \times 100\% = 0.0064\%$ of times will decay to a down quark and $|V_{ts}|^2 \times 100\% = 0.14\%$ to a strange quark.

check: [42]

1.1.3.2 Electroweak unification

At energies above the scale of the mass of the weak vector bosons ($E_{EW} \sim m_Z \sim m_W \sim 100 \text{ GeV}$), the electromagnetic and weak interactions are unified into the Electroweak (EW) force. In other words, electromagnetism and weak interactions are simultaneously described by the symmetry

CKM element	Value
V_{ud}	0.97370 ± 0.00014 [21] [22]
V_{us}	0.2245 ± 0.0008 [23] [24]
V_{cd}	0.221 ± 0.004 [25] [26] [27]
V_{cs}	0.984 ± 0.011 [28][29] [30]
V_{cb}	0.0410 ± 0.0014 [31][32]
V_{ub}	0.0038 ± 0.00024 [33] [34][35]
V_{td}	0.0080 ± 0.0003 [36][37]
V_{ts}	0.0380 ± 0.0011 [36][37]
V_{tb}	1.013 ± 0.030 [38][39][40]

Table 1.3: Magnitude of the nine elements of the CKM matrix. The mean for the different measurements has been done by [41]. **Igual me he venido arriba con las referencias. Son las que daba el Particle Data Group**

group $SU(2)_L \times U(1)_Y$. The subindex L refers to left-handed fields and Y to the weak hypercharge. In contrast, at low energies, this interactions are treated as independent phenomena, the electromagnetism is described QED and the weak interaction by Fermi's theory.

In the EW model (Glashow-Salam-Weinberg model), two new quantum numbers are assigned to the particles of the SM: the weak isospin (\vec{T}) and Y . Here, the left-handed chiral states of fermions form isospin doublets (χ_L) with $T_3 = \pm 1/2$ and the right-handed form chiral states are composed of isospin singlets (χ_R) with $T_3 = 0$. For a particle, T_3 is the third component of the \vec{T} , which is related to the electric charge (Q) and the $U(1)$ hypercharge by Gell-Mann-Nishijima relation:

$$Q = T_3 + \frac{1}{2}Y \quad (1.14)$$

With this expression, the electromagnetic coupling and the electroweak couplings are connected. Having χ_L with $T_3 = \pm 1/2$ and χ_R with $T_3 = 0$ implies that a $SU(2)$ weak interaction can rotate left-handed particles (i.e. convert a left-handed e^- into a left-handed ν_e emitting a W^-) but cannot do the same with right-handed.

Using the gauge invariance principle it is possible to find the QED and QCD Lagrangians, as it is described in Sections 1.1.2 and 1.1.4 respectively.

The free Lagrangian, as in the case of QED and QCD is:

$$\begin{aligned}\mathcal{L} &= i \sum_{j=1}^3 \bar{\Psi}(x) \gamma^\mu \partial_\mu \Psi(x) \\ &= i \sum_{j=1}^3 \bar{\chi}_L(x) \gamma^\mu \partial_\mu \chi_L(x) + i \sum_{k=1}^3 \bar{\chi}_R(x) \gamma^\mu \partial_\mu \chi_R(x)\end{aligned}\quad (1.15)$$

where the wave function Ψ has been spited into the left isospin doublets χ_L and and right isospin singlets χ_R . The indices j and k run over the three generations of the SM. This Lagrangian should be invariant when a gauge transformation under the $SU(2)_L \times U(1)_Y$ symmetry group in the flavour space is applied:

$$\chi_L(x) \xrightarrow{SU(2)_L \times U(1)_Y} \chi'_L(x) = \exp\{i\alpha^n \tau_n\} \exp\{i\beta y\} \chi_L(x) \quad (1.16)$$

$$\chi_R(x) \xrightarrow{SU(2)_L \times U(1)_Y} \chi'_R(x) = \exp\{i\beta y\} \chi_R(x) \quad (1.17)$$

with $\alpha, \beta \in \mathbb{R}$ and $n \in \{1, 2, 3\}$. This transformation is given by the generators of $SU(2)_L \times U(1)_Y$, i.e. the Pauli matrices (τ_n) and the weak hypercharge y . Note that $SU(2)_L$ transformation, $\exp\{i\alpha^n \tau_n\}$, only acts on the doublet fields. This term containing the Pauli matrices is non-abelian like in QCD and, like in QCD, this leads to self-interacting terms.

To ensure invariance under $SU(2)_L \times U(1)_Y$, four different gauge fields have to be added (three from $SU(2)$ and one from $U(1)$). Four is also the correct number of gauge bosons needed to describe EW interactions: W^+ , W^- , Z and Pgamma. While the three week isospin currents couple to the triplet of vector bosons W_μ^n with $n \in \{1, 2, 3\}$, the weak hypercharge couples to an isosinglet B_μ . The fields W_μ^1 and W_μ^2 are electrically charged whereas W_μ^3 and B_μ are neutral fields. The EW covariant derivative is defined as:

$$D^\mu \chi_{L_j}(x) = [\partial_\mu - ig \frac{\tau_i}{2} W_\mu^i(x) - ig' \frac{y_j}{2} B_\mu(x)] \chi_{L_j}(x) \quad i \in [1, 2, 3] \quad (1.18)$$

$$D^\mu \chi_{R_j}(x) = [\partial_\mu - ig' \frac{y_j}{2} B_\mu(x)] \chi_{R_j}(x) \quad (1.19)$$

where g and g' are the interaction couplings to W_μ^i isotriplet and the B_μ isosinglet.

Using the derivatives in equations 1.18 and 1.19, the Lagrangian in 1.20 is already invariant under local $SU(2)_L \times U(1)_Y$ transformations:

$$\mathcal{L} = i \sum_{j=1}^3 \bar{\chi}_L^j(x) \gamma^\mu D_\mu \chi_L^j(x) + i \sum_{k=1}^3 \bar{\chi}_R^k(x) \gamma^\mu D_\mu \chi_R^k(x) \quad (1.20)$$

Finally, if kinetic terms for the gauge bosons are included in 1.20, the EW SM Lagrangian is obtained:

$$\begin{aligned}\mathcal{L}_{EW} = & i \sum_{j=1}^3 \bar{\chi}_L^j(x) \gamma^\mu D_\mu \chi_L^j(x) + i \sum_{k=1}^3 \bar{\chi}_R^k(x) \gamma^\mu D_\mu \chi_R^k(x) \\ & - \frac{1}{4} W_{\mu\nu}^n(x) W_n^{\mu\nu}(x) - \frac{1}{4} B_{\mu\nu}(x) B^{\mu\nu}(x)\end{aligned}\quad (1.21)$$

501 Where the addition of kinetic terms gives rise to cubic and quadratic self-
 502 interactions among the gauge fields. Note that the mass terms of the fields
 503 are forbidden in order to ensure local gauge invariance and since the physical
 504 W^+ , W^- and Z bosons have a mass different from zero, for the moment
 505 let's assume that something breaks the symmetry generating the observed
 506 masses.

507 The in \mathcal{L}_{EW} in 1.21 can be divided in two different parts according to
 508 the charge of the bosons: charged currents and neutral currents. Relating
 509 the charged currents (W_μ^1 and W_μ^2) to the W^+ and W^- bosons of the SM
 510 and the neutral (W_μ^3 and B_μ) ones with the Z and γ , it is possible to build
 511 linear combinations fo the original gauge fields that define the SM bosons.

Therefore, from the charged-current interactions, the W^+ and W^- bosons are:

$$W^\pm \equiv \frac{1}{\sqrt{2}}(W_\mu^1 \mp i W_\mu^2) \quad (1.22)$$

While for the neutral-current these combinations can be defined as a rotation of the so called Weinberg (or weak mixing) angle θ_W :

$$\begin{pmatrix} W_\mu^3 \\ B_\mu \end{pmatrix} \equiv \begin{pmatrix} \cos \theta_W & \sin \theta_W \\ -\sin \theta_W & \cos \theta_W \end{pmatrix} \begin{pmatrix} Z_\mu \\ A_\mu \end{pmatrix}$$

Rewriting this equation, the photon and Z -boson fields are

$$A_\mu = B_\mu \cos \theta_W + W_\mu^3 \sin \theta_W Z_\mu \quad = -B_\mu \cos \theta_W + W_\mu^3 \sin \theta_W \quad (1.23)$$

In order to ensure that this A_μ is the one of QED, apart from the Gell-Mann-Nishijima relation (equation 1.14), it is requiered that the couplings of the γ , W and Z satisfy the relation:

$$g \sin \theta_W = g' \cos \theta_W = e \quad (1.24)$$

512 .

513 Within the unified EW model, once θ_W is known, the properties of
 514 Z are specified. Current measurements of θ_W give a value of $\sin^2 \theta_W =$
 515 0.2310 ± 0.0005 [43].

516 There is no mass term for the bosons in the EW Lagrangian that has
 517 been obtained in 1.21 by demanding the $SU(2)_L \times U(1)_Y$ local invariance,
 518 which enters in contradiction with the experimental observations for the
 519 W and Z bosons ($m_{Z,W} \sim 80$ GeV). The introduction of such a mass term
 520 would break the symmetry, however, the it is possible to add the mass for
 521 the W and Z bosons without loosing the properties of the symmetry. The
 522 method to do so is known as Englert–Brout–Higgs–Guralnik–Hagen–Kibble
 523 mechanism or, more commonly, just as Higgs mechanism. This mechanism
 524 is described in Section 1.1.5.

525 1.1.4 Quantum chromodynamics

526 1.1.4.1 Quarks and colour

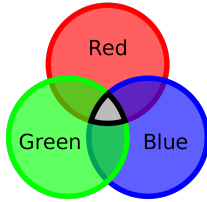
527 Quantum chromodynamics (QCD) is QFT-based theory for describing
 528 the strong interactions between quarks and gluons (partons). This type of
 529 interaction is the responsabile of the nuclear force, the one that acts between
 530 the protons and neutrons of atoms binding them together. Without the
 531 strong force, the protons inside the nucleus would push each other apart
 532 due to the electromagnetic repulsion. It also holds the quarks within a
 533 hadron together.

QCD is based in the $SU(3)$ symmetry group and its name derives from the “colour” charge, an analogous to the electric charge of QED but for strong interactions. The colour charge was introduced in 1964 [44] to explain how quarks could coexist within some hadrons apparently having the same quantum state without violating the Pauli exclusion principle. To satisfy the Fermi-Dirac statistics it is necessary to add an additional quantum number, the colour, to the theory. Each specie of quark (q) may have three different colours (q^α , $\alpha = 1, 2, 3$): red, green, blue. Baryons and mesons are described then by the colour singlet combinations:

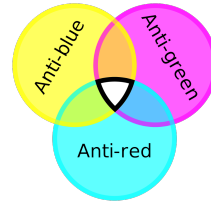
$$B = \frac{1}{\sqrt{6}} \epsilon^{\alpha\beta\gamma} |q_\alpha q_\beta q_\gamma\rangle \quad M = \frac{1}{\sqrt{3}} \epsilon^{\alpha\beta} |q_\alpha \bar{q}_\beta\rangle$$

534 .

535 Additionally, it is postulated that all hadrons must have a global neut-
 536 ral colour charge, i.e. the hadrons must be “colourless”. This assumption
 537 is known as confinement hypothesis and it is made to avoid the existence
 538 of non-observed extra states with non-zero colour. It is called colour con-
 539 finement because it implies that it is not possible to observe free quarks
 540 since they carry colour charge and, hence, they have to be confined within
 541 colour-singlet combinations. Figure 1.3 depicts how different colours and
 542 anticolours combine to create the “colourless” state.



(a) Quark colours combine to be colourless.



(b) Antiquark colours also combine to be colourless.

Figure 1.3: Colour charge combinations for quarks and antiquarks

⁵⁴³ **1.1.4.2 Gauge invariance for $SU(3)$**

The dynamics of the quarks and gluons are controlled by the QCD Lagrangian. Using the power of the gauge invariance principle it is possible to deduce \mathcal{L}_{QCD} similarly to the reasoning developed in Section 1.1.2. Firstly, let's denote a quark field of colour α and flavour f by q_f^α . The vector $q_f^T \equiv (q_f^1, q_f^2, q_f^3)$ is defined under the $SU(3)$ colour space, meaning that each dimension corresponds to a colour. The Lagrangian

$$\mathcal{L}_0 = \sum_f \bar{q}_f (i\gamma^\mu \partial_\mu - m_f) q_f \quad (1.25)$$

is invariant under global $SU(3)$ transformation in the colour space,

$$q_f^\alpha \rightarrow (q_f^\alpha)' = U_\beta^\alpha q_\beta^\alpha, \quad UU^\dagger = U^\dagger U = 1, \quad \det U = 1 \quad (1.26)$$

⁵⁴⁴ .

In the $SU(N)$ algebra, $SU(N)$ is the group of $N \times N$ unitary matrices (U) which can be written in the form $U = \exp\{i(\lambda^a/2)\theta_a\}$ with $a = 1, 2, \dots, N^2 - 1$. Therefore, the $SU(3)$ matrices can be written as

$$U = \exp\left\{i\frac{\lambda^a}{2}\theta_a\right\} \quad (1.27)$$

where the index a goes from 1 to 8 for the arbitrary parameter θ_a and $\frac{\lambda^a}{2}$, which denotes the fundamental representation of the $SU(3)$ algebra. The Einstein notation for summation over repeated indices is implied. The matrices λ^a are traceless and satisfy the commutation relations [11]:

$$\left[\frac{\lambda^a}{2}, \frac{\lambda^b}{2}\right] = if^{abc} \frac{\lambda^c}{2} \quad (1.28)$$

⁵⁴⁵ , being f^{abc} the $SU(3)_C$ structure constants, which are real and totally ⁵⁴⁶ antisymmetric.

To satisfy the gauge invariance requirement, the Lagrangian has to be invariant under $SU(3)$ local transformations, i.e, transformations in which

the phase is dependent of the space-time location, $\theta_a = \theta_a(x)$. To fulfil the condition, the quark derivatives in the Lagrangian in 1.25 have to be substituted by covariant objects. Since there are eight independent gauge parameters, eight different gauge bosons $G_a^\mu(x)$ are needed⁷. These bosons are the eight gluons and the new covariant objects are:

$$D^\mu q_f \equiv \left[\partial_\mu + ig_s \frac{\lambda^a}{2} G_a^\mu(x) \right] q_f \equiv [\partial_\mu + ig_s G^\mu(x)] q_f$$

- ⁵⁴⁷ The compact matrix notation is used $[G^\mu(x)]_{\alpha\beta} \equiv \left(\frac{\lambda^a}{2} \right)_{\alpha\beta} G_a^\mu(x)$.

To ensure that the covariant derivative ($D^\mu q_f$) transforms like the q_f , the transformation of the gauge fields are:

$$D^\mu \rightarrow (D^\mu)' = UD^\mu U^\dagger \quad G^\mu \rightarrow (G^\mu)' = UG^\mu U^\dagger + \frac{i}{g_s} (\partial_\mu U) U^\dagger \quad (1.29)$$

. The quark and gluon fields transform under an infinitesimal local transformation, i.e. $\theta_a(x) = \delta\theta_a(x) \approx 0$, the $SU(3)_C$ unitary matrices (eq. 1.27) can be expressed as their first order expansion:

$$U = \exp\left\{ i \frac{\lambda^a}{2} \theta_a(x) \right\} \approx 1 + i \left(\frac{\lambda^a}{2} \right) \delta\theta_a(x)$$

and, consequently, the transformations for the colour-vector field (eq. 1.26) and gluon field (eq. 1.29) become:

$$\begin{aligned} q_f^\alpha &\rightarrow (q_f^\alpha)' = q_f^\alpha + \left(\frac{\lambda^a}{2} \right)_{\alpha\beta} \delta\theta_a q_f^\beta \\ G_a^\mu &\rightarrow (G_a^\mu)' = G_a^\mu - i \frac{i}{g_s} \partial_\mu (\delta\theta_a) - f^{abc} \delta\theta_b G_c^\mu \end{aligned}$$

- ⁵⁴⁸ .

⁵⁴⁹ In contrast to the transformation for the photon field in QED (equation 1.5), the non-commutativity⁸ of the $SU(3)_C$ matrices give rise to an additional term involving the gluon fields themselves ($-f^{abc} \delta\theta_b G_c^\mu$), as the relation 1.28 expresses. For constant $\delta\theta_a$, the transformation rule for the gauge fields is expressed in terms of the structure constants f^{abc} ; thus, the gluon fields belong to the adjoint representation for the colour group. There is a unique coupling at $SU(3)_C$, g_s . All the colour-triplet flavours couple to the gluon fields with exactly the same interaction strength.

⁷The eightfold multiplicity of gluons is labeled by a combination of color and anticolor charge (e.g. red–antigreen)

⁸Because the generators of $SU(3)$ do not commute, QCD is known as non-Abelian gauge theory.

It is necessary to introduce the corresponding fields strengths to build a gauge-invariant kinetic terms for the gluon fields.

$$G^{\mu\nu} \equiv -i\frac{-i}{g_s}[D^\mu, D^\nu] = \partial_\mu G^\nu - \partial_\nu G^\mu + ig_s[G^\mu, G^\nu] \equiv \frac{\lambda^a}{2}G_a^{\mu\nu}(x)$$

$$G_a^{\mu\nu} \equiv \partial_\mu G_a^\nu - \partial_\nu G_a^\mu - g_s f^{abc} G_b^\mu G_c^\nu$$

Under a $SU(3)_C$ transformation,

$$G^{\mu\nu} \rightarrow (G^{\mu\nu})' = U G^{\mu\nu} U^\dagger \quad (1.30)$$

and the colour trace $\text{Tr}(G^{\mu\nu}G_{\mu\nu}) = \frac{1}{2}G^{\mu\nu}G_{\mu\nu}$ remains invariant. Normalising the gluon kinetic term, the $SU(3)_C$ invariant QCD Lagrangian is obtained:

$$\mathcal{L}_{QCD} \equiv -\frac{1}{4}G_a^{\mu\nu}G_a^{\mu\nu} + \sum_f \bar{q}_f(i\gamma^\mu D_\mu - m_f)q_f \quad (1.31)$$

557 Note how the gluon-gluon vertex is find by demanding the gauge invari-
 558 ance under local $SU(3)_C$ transformation. A mass term is forbidden for the
 559 gluon fields by the $SU(3)_C$ gauge symmetry because something of the form
 560 $\frac{1}{2}m_G^2 G_a^\mu G_\mu^a$ would not be invariant under the transformation in 1.29. The
 561 gluons are, then, predicted by the theory to be spin-1 massless particles.

562 Thanks to the colour symmetry properties, this Lagrangian looks very
 563 simple and all its interactions depend on the strong coupling constant, g_s .
 564 In contrast to the Lagrangian derived for QED (eq 1.7), in \mathcal{L}_{QCD} the boson
 565 field have a self-interacting term. This gluon self-interactions give rise to the
 566 triple and quadratic gluon vertex (center and right diagrams in Figure 1.4).
 567 This self-interactions among the gluon fields can explain features the asymp-
 568 totic freedom and confinement, properties that were not present in QED.
 569 The asymptotic freedom causes interactions between particles to become
 570 asymptotically weaker as the energy scale increases and the corresponding
 571 length scale decreases. The confinement implies that the strong forces in-
 572 crease with the distance, therefore, as two colour charges are separated,
 573 at some point it becomes energetically favorable for a new quark-antiquark
 574 pair to appear rather than keep getting further. This new quarks bond with
 575 the previous two, preventing single quarks to be isolated. This mechanism,
 576 depicted in Figure 1.5, explains why the strong interaction is responsable
 577 for keeping the quarks together forming hadrons.

578 **Maybe, expand the QCD Lagrangian in 1.31 and explain its
 579 different elements.**

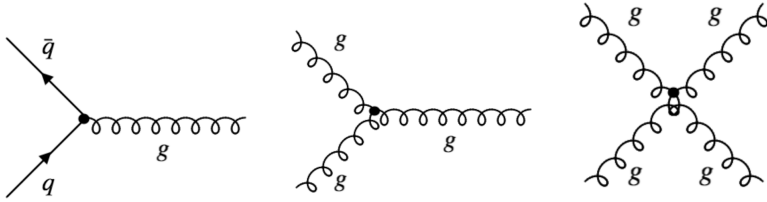


Figure 1.4: The predicted QCD interaction vertices arising from the requirement of $SU(3)_C$ local gauge invariance. The presence of the triples and quadruple gluon vertices is possible to the Non-Abelian nature of $SU(3)_C$.



Figure 1.5: The QCD colour confinement explains the inseparability of quarks inside a hadron in spite of investing ever more energy. In this example, the mechanism is shown for a meson.

580 1.1.5 Particle masses

For the QED Lagrangian, \mathcal{L}_{QED} (eq. 1.9), it is clear how the mass of the photon must be zero in order to satisfy the $U(1)$ local gauge symmetry because, if a mass term for the vector gauge field A_μ is included, the \mathcal{L}_{QED} would be:

$$\mathcal{L}_{QED} = \bar{\Psi}(x)(i\gamma^\mu\partial_\mu - m)\Psi(x) - eQ\bar{\Psi}(x)\gamma^\mu A_\mu\Psi(x) - \frac{1}{4}F_{\mu\nu}(x)F^{\mu\nu}(x) + \frac{1}{2}m_\gamma^2 A_\mu A^\mu$$

and, with the $U(1)$ transformation in equation 1.5, the new mass term becomes:

$$\frac{1}{2}m_\gamma^2 A_\mu A^\mu \rightarrow \frac{1}{2}m_\gamma^2 (A_\mu + \frac{1}{e}\partial_\mu\theta)(A^\mu + \frac{1}{e}\partial^\mu\theta) \neq \frac{1}{2}m_\gamma^2 A_\mu A^\mu$$

581 Confirming that the photon mass term is not invariant under local $U(1)$
 582 and, consequently, that the photon must be massless to satisfy the gauge
 583 invariance. Experimental efforts to measure the mass of the photon have
 584 set an upper limit of $m_\gamma \leq 1 \times 10^{-18}$ eV [45].

585 With the Lagrangian of QCD in equation 1.31 happens the same, the
 586 mass term for the gluon fields are forbidden by the $SU(3)_C$ gauge symmetry.
 587 Therefore, the mediating bosons for the strong interactions are massless as
 588 well (experimentally, a mass as large as upper limits of a few MeV have
 589 been seted, see [46]).

590 While the prohibition of mass terms for the bosons of QED and QCD is
 591 not a problem, this requirement also applies to the $SU(2)_L$. This condition

592 enters into open contradiction with the measurements of large masses for
 593 the W ($m_W = 80.370 \pm 0.007$ (stat.) ± 0.017 (syst.) MeV[47]) and Z ($m_Z =$
 594 91.1852 ± 0.0030 GeV [48]) bosons of weak interactions. <- to do: Aquí
 595 no estoy utilizando las mismas medidas de la masa de m_W y m_Z
 596 que antes. He de escoger una and stick to it.

597 For weak interactions, the problem of massless particles do not only
 598 affect the bosons. Since under the $SU(2)_L$ transformations left-handed
 599 particles transform as weak isospin doubles and right-handed particles as
 600 isospin singlets, the mass term of a spinor field Ψ written as chiral states
 601 also breaks the required gauge invariance: $-m\bar{\Psi}(x)\Psi(x) = -m\bar{\Psi}(x)(P_R +$
 602 $P_L)\Psi(x) = -m(\bar{\Psi}_R(x)\Psi_L(x) + \bar{\Psi}_L(x)\Psi_R(x))$

603 The Higgs mechanism describes how both the W and Z bosons and the
 604 fermions acquire mass without breaking the local gauge symmetry of the
 605 SM.

606 1.1.5.1 The Higgs mechanism

Goldstone theorem and spontaneous symmetry breaking

For a scalar field ϕ with a Lagrangian of the form:

$$\mathcal{L} = \frac{1}{2}\partial_\mu\phi_i\partial^\mu\phi_i - V(\phi) \text{ where } V(\phi) = \frac{1}{2}\mu^2\phi_i\phi_i + \frac{1}{4}\lambda(\phi_i\phi_i)^2 \quad (1.32)$$

This Lagrangian is invariant under $\phi_i \rightarrow \phi'_i = R_{ij}\phi_j$, where R_{ij} are rotational matrices in 4-dimensions. The mass term is the one with $\phi_i\phi_i$ and the parameter λ has to be positive for \mathcal{L} to describe a physical system, if $\lambda < 0$ the potential is unbounded from below. Contrary, the parameter μ^2 can be either positive or negative. As depicted in Figure 1.6a, if $\mu^2 > 0$, the vacuum expectation value (i.e. minimum of potential) is located at the origin ϕ_0 and this \mathcal{L} would describe a spin-0 particle of mass μ . However, if $\mu^2 < 0$, the potential $V(\phi)$ has the form of Figure 1.6a and \mathcal{L} would not represent anymore the Lagrangian of a particle of mass μ . The vacuum expectation value is now multivalued:

$$\phi_0 = \pm\sqrt{-\frac{\mu^2}{\lambda}} \equiv \pm v$$

Expanding the field around the minima at $\phi_i = (0, 0, 0, v)$, the \mathcal{L} becomes:

$$\begin{aligned} \mathcal{L} = & \frac{1}{2}\partial_\mu\sigma\partial^\mu\sigma + \mu^2\sigma^2 - \sqrt{\mu^2\lambda}\sigma^3 - \frac{1}{4}\lambda^4 \\ & + \frac{1}{2}\partial_\mu\pi_i\partial^\mu\pi_i - \frac{1}{4}\lambda(\pi_i\pi_i)^4 - \lambda v\pi_i\pi_i\sigma - \frac{1}{2}\pi_i\pi_i\sigma^2 \end{aligned} \quad (1.33)$$

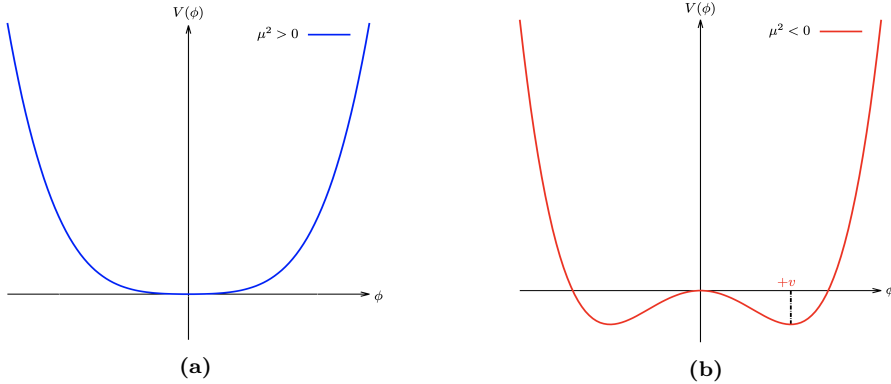


Figure 1.6: The potential $V(\phi)$ of Lagrangian 1.32 for (a) μ^2 positive and (b) negative.

where i runs from 1 to 3. Here $\sigma = \phi_4 - v$ and $\pi_i = \phi_i$ are new boson fields, being the latter massless and the with a mass of $m_\sigma^2 = -2\mu^2$. The new terms break the original symmetry because the symmetry of the Lagrangian is not longer a symmetry of the vacuum, it has been spontaneously broken. One massive σ boson and three massless π_i bosons with a residual $O(3)$ symmetry have appeared. This is a consequence of the Goldstone theorem which states that “for a continuous symmetry group \mathcal{G} spontaneously broken down to a subgroup \mathcal{H} , the number of broken generators is equal to the number of massless scalars that appear in the theory” [49]. Therefore, since the $O(N)$ group has $N(N-1)/2$ generators, the $O(N-1)$ has $(N-1)(N-2)/2$ and, hence, $N-1$ Goldstone bosons appear. The example shown is for $N=4$.

The Higgs mechanism in the SM - Bosons

To apply this mechanism to the SM, it is necessary to generate mass for the W^+ , W^- and Z bosons while keeping the photon massless. In order to do so, the EW symmetry group $SU(2)_L \times U(1)_Y$ has to be broken into a $U(1)$ subgroup describing electromagnetism. A gauge-invariant interaction that gives masses to fermions without mixing chiral components is introduced by defining a $SU(2)$ isospin doublet of complex scalar field with hypercharge $Y=1$:

$$\Phi = \begin{pmatrix} \phi^+ \\ \phi^0 \end{pmatrix}$$

Being ϕ^+ positively charged and ϕ^0 neutral. The Lagrangian \mathcal{L}_{Higgs} has to be added to the \mathcal{L}_{EW} in 1.21.

$$\mathcal{L}_{Higgs} = (D_\mu \Phi)^\dagger (D^\mu \Phi) - V(\Phi) \text{ where } V(\Phi) = \mu^2 \Phi^\dagger \Phi + \lambda (\Phi^\dagger \Phi)^2$$

with $\lambda > 0$ required for vacuum stability. When $\mu^2 > 0$, the minimum of the potential occurs when both fields (ϕ^+ and ϕ^0) are at zero. If $\mu^2 < 0$, the minimum of the potential has an infinite number of degenerate states that

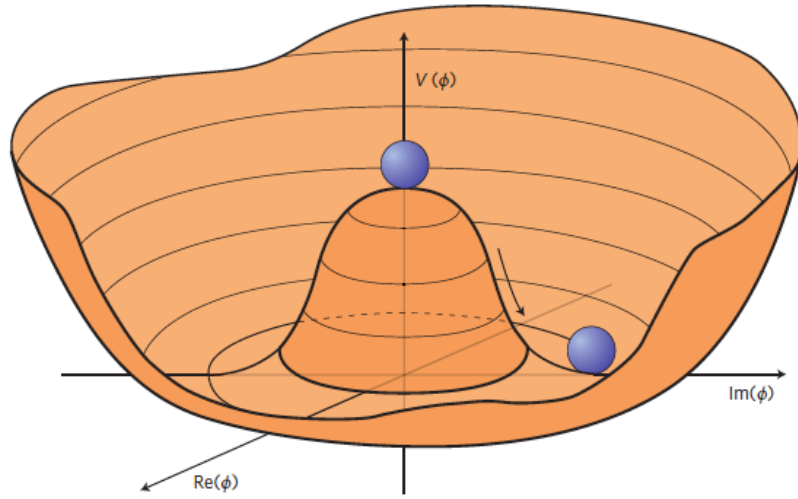


Figure 1.7: An illustration of the Higgs potential $V(\Phi)$ in the case of $\mu^2 < 0$. Choosing any particular point in the circle defined by v spontaneously breaks the $U(1)$ rotational symmetry. This type of potential is frequently called “Mexican hat”.

satisfy $\Phi^\dagger \Phi = \mu^2/2\lambda$ and the physical vacuum state will correspond to any particular point on the circle of Figure 1.7. Having to chose a particular point breaks the global $U(1)$ symmetry of the Lagrangian. Without loss of generality, in this scenario, the ground state Φ_0 can be chosen to be:

$$\Phi_0 = \frac{1}{\sqrt{2}} \begin{pmatrix} 0 \\ v \end{pmatrix} \text{ where } v = 2\sqrt{\frac{\mu^2}{\lambda}}$$

618 being v the vacuum expectation value. This defines the already mentioned
619 circle in the minimum of $V(\Phi)$ in the $\mu^2 < 0$ scenario.

The Lagrangian density must be formulated in terms of deviations from one of these ground states. This can be done by introducing an excitation, $h(x)$, that can be understood as a small deviation of the field from the ground state. Accordingly, the fields can be expanded around the minimum as:

$$\Phi = \frac{1}{\sqrt{2}} \begin{pmatrix} 0 \\ v + h(x) \end{pmatrix} \exp\{i\chi(x)\}$$

The new field $\chi(x)$ can be set to zero in the so called “unitary gauge”.

$$\Phi = \frac{1}{\sqrt{2}} \begin{pmatrix} 0 \\ v + h(x) \end{pmatrix} \quad (1.34)$$

Expanding the covariant derivative of the \mathcal{L}_{Higgs} :

$$\begin{aligned}
 (D_\mu \Phi)^\dagger (D^\mu \Phi) &= \left| \left(\partial_\mu + ig \frac{\tau^k}{2} W_\mu^k(x) + ig' \frac{y}{2} B_\mu \right) \right|^2 \\
 &= \frac{1}{2} \left| \begin{pmatrix} \partial_\mu + i\frac{1}{2}(gW_\mu^3 + g'\frac{y}{2}B_\mu) & i\frac{g}{2}(W_\mu^1 - iW_\mu^2) \\ i\frac{g}{2}(W_\mu^1 - iW_\mu^2) & \partial_\mu - i\frac{1}{2}(gW_\mu^3 - g'\frac{y}{2}B_\mu) \end{pmatrix} \begin{pmatrix} 0 \\ v+h \end{pmatrix} \right|^2 \\
 &= \frac{1}{2}(\partial_\mu h)^2 + \frac{1}{8}(v+h)^2 |W_\mu^1 - iW_\mu^2|^2 \\
 &\quad + \frac{1}{8}(v+h)^2 |gW_\mu^3 - g'B_\mu| + (\text{interaction terms})
 \end{aligned}$$

Where the τ_k with $k = 1, 2, 3$ are the Pauli Matrices. In this equation there are terms mixing the W^3 and the B_μ fields that, by using the physical fields defined in equation 1.1.3.2, should disappear since the physical bosons do not mix. Applying the relation 1.1.3.2 into the covariant derivative,

$$(D_\mu \Phi)^\dagger (D^\mu \Phi) = \frac{1}{2} + \frac{g^2 v^2}{4} W_\mu^+ W^{-\mu} + \frac{g^2 v^2}{8 \cos^2 \theta_W} Z_\mu Z^\mu + 0 A_\mu A^\mu$$

, the W^+ , W^- and Z bosons have finally acquired mass. Through the Higgs mechanism, their masses within the SM are:

$$M_W = \frac{1}{2} g v \quad M_Z = \frac{1}{2} \frac{g v}{\cos \theta_W}$$

620 Additionally, a new scalar field $h(x)$ has appeared with its correspondent
 621 mass term, the Higgs field. Note that the $h(x)$ was introduced as a perturba-
 622 tion from the ground state of the Higgs potential $V(\Phi)$, so the Higgs boson
 623 can be understood as an excitation of the Higgs potential. Apart from cou-
 624 plings to the electroweak gauge fields, the Higgs field has also self-interaction
 625 vertices. The mass of this boson is $m_H = \sqrt{2}\mu$.

With this covariant term, the Higgs Lagrangian density of the system is obtained:

$$\begin{aligned}
 \mathcal{L}_{Higgs} &= \frac{1}{2}(\partial_\mu h)(\partial^\mu h) + \frac{g}{4}(v+h)^4 W_\mu W^\mu + \frac{g^2}{8 \cos^2 \theta_W} (v+h)^2 Z_\mu Z^\mu \\
 &\quad + \frac{\mu^2}{2}(v+h)^2 - \frac{\lambda}{16}(v+h)^4
 \end{aligned}$$

and expressing it in terms of the boson masses and coupling parameters, it can be written as:

$$\begin{aligned}\mathcal{L}_{Higgs} = & \frac{1}{2}(\partial_\mu h)(\partial^\mu h) - \frac{1}{2}m_H^2 h^2 + \frac{1}{2}m_W W_\mu W^\mu + \frac{1}{2}m_Z Z_\mu Z^\mu + gm_W h W_\mu W^\mu \\ & + \frac{g^2}{4}W_\mu W^\mu + g \frac{m_Z}{2\cos\theta_W} h Z_\mu Z^\mu - g^2 \frac{1}{4\cos^2\theta_W} h^2 Z_\mu Z^\mu - g \frac{m_H^2}{4m_W} h^3 \\ & - g^2 \frac{m_H^2}{32m_W^2} h^4 + \text{const.}\end{aligned}\tag{1.35}$$

As can be seen in the Lagrangian 1.35, the coupling strengths of the W and Z fields to the Higgs are proportional to m_W and m_Z respectively. This why it is said that the more a fundamental particle interacts with the Higgs boson, the more massive it is.

The Higgs mechanism in the SM - Fermions

The Higgs mechanism for spontaneous symmetry breaking of the $SU(2)_L \times U(1)_Y$ gauge group of the SM generates the masses of the W^\pm and Z bosons. For originating the mass of the fermions without violating the EW gauge symmetry a similar procedure is carried but taking into account that the left-handed particles transform different than the right-handed. To do so, additional terms including the Yukawa couplings are added into the Lagrangian. These terms are of the form:

$$-y_f (\bar{\chi}_L^f \Phi \chi_R^f + \bar{\chi}_R^f \Phi^\dagger \chi_L^f)$$

where the f superindex runs over all quarks and charged leptons. It is usual to express the second part of the sum just as “plus hermitic conjugate” (“+ h.c.”). Note that the hermitic conjugate part is necessary to ensure that expression fulfills the requirement for a hermitian operator to be self-adjoint in a complex Hilbert space. The different y_f constants are known as Yukawa couplings of the particle f to the Higgs field. The Higgs doublet is denoted by Φ . For the electron $SU(2)$ doublet, the element with this coupling can be written as:

$$\mathcal{L}_e = -y_e \left[(\bar{\nu}_e \bar{e})_L \begin{pmatrix} \phi^+ \\ \phi^0 \end{pmatrix} e_R + \bar{e}_R (\phi^{+*} \phi^{0*}) \begin{pmatrix} \nu_e \\ e \end{pmatrix}_L \right] \tag{1.36}$$

Here, y_e is the Yukawa coupling of the electron to the Higgs boson. After spontaneously breaking the symmetry as it is done in eq. 1.34, the Lagrangian in 1.36 becomes:

$$\mathcal{L}_e = \frac{-y_e}{\sqrt{2}} v (\bar{e}_L e_R + \bar{e}_R e_L) + \frac{-y_e}{\sqrt{2}} h (\bar{e}_L e_R + \bar{e}_R e_L) \tag{1.37}$$

The y_e is not predicted by the Higgs mechanism, but can be chosen to be consistent with the observed electron mass (m_e) so that $y_e = \sqrt{2}m_e/v$. Using this relation, the Lagrangian in 1.37 becomes:

$$\mathcal{L}_e = -m_e \bar{e}e - \frac{m_e}{v} \bar{e}eh \quad (1.38)$$

630 The first element of the Lagrangian in 1.38 gives mass to the electron and
 631 gives rise to the coupling of the electron to the Higgs fields in its non-
 632 zero vacuum expectation. The second term represents the coupling of the
 633 electron and the Higgs boson itself.

634 The non-zero vacuum expectation value occurs only in the neutral part
 635 of the Higgs doublet (the lower in $\Phi = \begin{pmatrix} \phi^+ \\ \phi_0 \end{pmatrix}$) due to the form in the
 636 ground state in 1.34. This implies that the combination $\bar{\chi}_L^f \Phi \chi_R^f + \bar{\chi}_R^f \Phi^\dagger \chi_L^f$
 637 can only generate masses for the fermions in the lower component of an
 638 $SU(2)$ doublet, i.e. the charged leptons and the down type quarks. Putting
 639 aside the procedure to give mass to the up-type quarks, this explains why
 640 the neutrinos do not get mass through the Higgs mechanism.

For the up-type quarks, a gauge invariant term can be constructed from $\bar{\chi}_L^f \Phi_c \chi_R^f + \bar{\chi}_R^f \Phi_c^\dagger \chi_L^f$:

$$\mathcal{L}_u = y_u (\bar{u} \bar{d})_L \begin{pmatrix} -\phi^{0*} \\ \phi^- \end{pmatrix} u_R + \text{h.c.}$$

Applying the symmetry breaking:

$$\mathcal{L}_u = \frac{-y_u}{\sqrt{2}} v (\bar{u}_L u_R + \bar{u}_R u_L) + \frac{-y_u}{\sqrt{2}} h (\bar{u}_L u_R + \bar{u}_R u_L)$$

with a Yukawa coupling between the up quark and the boson $y_u = \sqrt{2}m_u/v$, resulting in:

$$\mathcal{L}_u = -m_u \bar{u}u - \frac{m_u}{v} \bar{u}uh$$

641 .

Therefore, for Dirac fermions, mass terms that let the Lagrangian invariant under local gauge transformations can be constructed from

$$\mathcal{L} = -y_f [\bar{\chi}_L^f \Phi \chi_R^f + (\bar{\chi}_R^f \Phi \chi_L^f)^\dagger] \quad \text{or} \quad \mathcal{L} = y_f [\bar{\chi}_L^f \Phi_c \chi_R^f + (\bar{\chi}_R^f \Phi_c \chi_L^f)^\dagger]$$

. The left Lagrangian is used for the leptons and down-type quarks, while the right one is used for the up-type quarks. These elements give rise not only to the mass of the fermions but also to the interaction strengths

between these fermions and the Higgs boson. The Yukawa coupling of the fermions to the Higgs field is given by:

$$y_f = \sqrt{2} \frac{m_f}{v} \quad (1.39)$$

where the Higgs vacuum expectation value is fixed by the Fermi coupling G_F and is measured to be $v = \sqrt{2} G_F \approx 246.22 \text{ GeV}$. The G_F is measured from the μ^+ lifetime [50]. The G_F is also used to determine the magnitude of the elements in the CKM matrix.

The value of fermionic masses is not predicted by the SM but obtained through experimental observations. Given the $m_{top} = 172.76 \pm 0.30 \text{ GeV}$, it is of particular interest the Yukawa coupling of the top quark to the Higgs field, y_t , which is almost exactly equal to one. It is important to verify this because deviation of the measured y_t from the SM prediction would be a proof of new phenomena beyond the SM that could provide an answer to several open questions concerning the fundamental interactions of elementary particles.

1.1.6 Charge-Parity

Probably, this section is gonna be absorbed by 1.1.3

1.1.7 Wrap up

Perhaps the ultimate and definitive (if talking about definitive makes any sense) theory of particle physics is a simple equation with a small number of free parameters. Meanwhile, the SM is here, and while it is not the ultimate theory, it is unquestionably one of modern physics' greatest successes. Despite its achievements, many questions remain unsolved.

1.1.7.1 The parameters of the Standard Model

The SM contains 25 free parameters that must be determined through observation and experimentation. These are the masses of the twelve fermions (assuming color variations and antiparticles are not viewed as separate fermions), or, more precisely, the twelve Yukawa couplings to the Higgs field.

$$m_{\nu_1}, m_{\nu_2}, m_{\nu_3}, m_e, m_\mu, m_\tau, m_u, m_d, m_c, m_s, m_t \text{ and } m_b$$

The three coupling constants of describing the strength of the gauge interactions

$$g, g' \text{ and } g_s$$

the two parameters describing the Higgs potential (μ and λ) or, equivalently, its vacuum expectation value and the Higgs mass

$$v \text{ and } m_h$$

The three mixing angles and the complex phase of the CKM matrix and the four of the PMNS matrix (the Pontecorvo–Maki–Nakagawa–Sakata matrix is similar to the CKM matrix but for the mixing of neutrino-mass eigenstates with neutrino-falvour eigenstates):

$$\theta_{12}, \theta_{13}, \theta_{23}, \rho_{13}, \theta'_a, \theta'_b, \theta'_c \text{ and } \theta'_d$$

663 From the 25 free parameters of the SM, 14 are associated to the Higgs
 664 field, eight with the flavour sector and only three with the gauge interac-
 665 tions.

666 1.1.7.2 Problems with the Standard Model

667 While the SM is very good theory that has passed rigorous testing, this
 668 is not the ending of the story, there are several limitations of the SM and
 669 a variety phenomena that it does not explain. The SM does not cover all
 670 questions in the universe and, hence, physicist continue looking for better
 671 theories to explain more. There is a long list of small and minor issues with
 672 the SM but lets focus on the most relevant ones.

673 Gravity

674 Gravity is the first force that any person learns about and the one known
 675 by the humankind for the most time. The SM describes all the other funda-
 676 mental interactions but this one. In the Table 1.1, the four forces are
 677 presented along with the theories to describe them. While QCD, QED and
 678 EW interactions are part of the SM, the GR is not. GR is a geometric the-
 679 ory that currently describes the gravitation in modern physics. Some of the
 680 suggested solutions to integrate gravitational interactions in the SM consist
 681 in postulating a new force carrier particle, the “graviton”, that mediates
 682 this interaction in a similar way to how the gauge bosons were proposed.
 683 Other explanations state that the gravity can only be described by a deeper
 684 theory in which the time-space structure is not flat like it is in the SM but
 685 dynamic.

686 Neutrino masses

687 According to the SM the neutrinos are massless, nevertheless, many ex-
 688 periments confirm that this is not true [51]. This is due to a property of

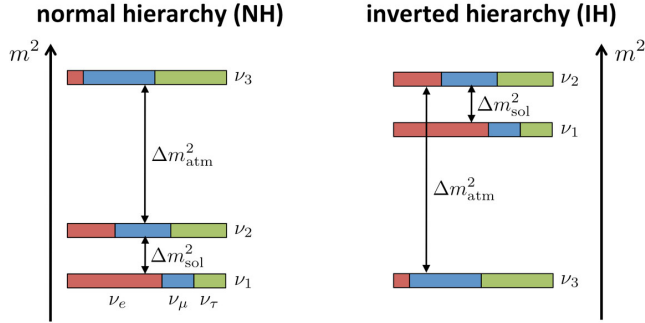


Figure 1.8: Two potential mass orderings of neutrinos are the normal ordering (normal hierarchy) and the inverted ordering (inverted hierarchy)

neutrinos that allows them to change their flavour while traveling through the space, this feature is known as “neutrino oscillations”. Each of the three neutrino flavours (ν_e , ν_μ , ν_τ) is a linear combination of three discrete neutrino-mass eigenstates (ν_i with $i \in \{1, 2, 3\}$) with mass eigenvalues (m_i). While the neutrino oscillation experiments could probe the squared neutrino-mass eigenvalues (Δm_{ij}^2), both the total scale of the masses and the sign of Δm_{ij} remains as some the most relevant open questions in particle physics. Regarding to the sign of Δm_{ij} , it is known that the mass of ν_2 is slightly higher than ν_1 ($\Delta m_{21}^2 \equiv m_2^2 - m_1^2 \sim 10^{-4}$ eV) but for the third mass eigenstate it has not been measured yet whether it is greater (normal ordering) or lower (inverted ordering) than the other two. This is referred as “hierarchy problem” and is depicted in Figure 1.8. Nevertheless, the absolute square difference is known ($\Delta m_{31}^2 \equiv |m_3^2 - m_1^2| \sim 10^{-3}$ eV).

Non-zero neutrino masses opened an interesting portal on beyond SM physics and, even though neutrinos are very elusive when it comes to detect them, some next-generation experiments such as Dune are very promising when it comes to set competitive and model independent limits on neutrino masses.

Regarding to the nature of this mass, one could add mass terms to the SM as it is done in Section 1.1.5.1 for the up-type quarks but the origin of the neutrino masses is still not known. It is possible that this mass comes from the Higgs mechanism, however, this is not clear. Also, if neutrinos gained mass through Yukawa interaction, it would imply the presence of right-handed neutrinos, which has not been observed.

713 Matter-antimatter asymmetry

714 In principle, the Big Bang should have produced an equal amount of matter
715 and antimatter which would all have then annihilated, leaving behind an

716 empty Universe filled with EM radiation. However, everything we see now
717 is essentially totally constituted of matter, from the tiniest life forms on
718 Earth to the greatest celestial objects. In comparison, there isn't a lot of
719 antimatter around.

720 By looking at the CMB radiation, which contain the residual photons
721 of the Big Bang, researchers have determined that there was a symmetry
722 between the matter and antimatter content in the early universe. For every
723 3×10^9 antimatter particles, there were 3×10^9 and 1 matter particles. The
724 matter and antimatter annihilate and produced the CMB and the remaining
725 1 part turned into all the stars and galaxies that are seen. The field of
726 cosmology that studies the processes that produced an asymmetry between
727 leptons and antileptons in the very early universe is called leptogenesis.

728 Researches carried during the last few decades have revealed that the
729 laws of nature do not equally apply to matter and antimatter. So far, the
730 only non-trivial difference between matter and antimatter found is the \mathcal{CP}
731 asymmetry (or \mathcal{CP} violation, which has been introduced in Section 1.1.3).
732 Alas, the quantity of \mathcal{CP} asymmetry included in the SM is insufficient to
733 explain the composition of the observable universe and, hence, extensive
734 searches of new sources of \mathcal{CP} violation are being carried.

735 In this context, the studies described in this thesis are part of the seek
736 of new \mathcal{CP} -violation sources. As Section 1.4.2 details, the observation of a
737 cross-section greater than the one predicted by the SM would imply that
738 Higgs-single-top-quark associated production does not conserve \mathcal{CP} .

739 Strong \mathcal{CP} problem

740

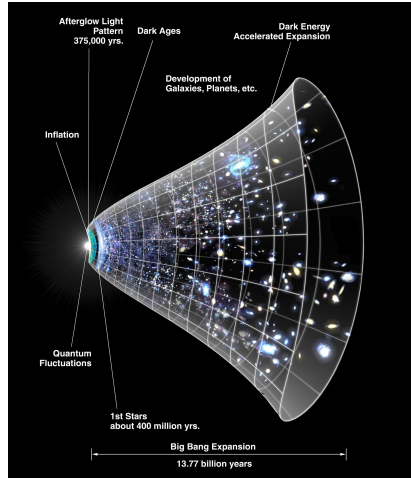
741 Dark energy

742 According to cosmological observations, the matter described by the SM
743 only makes up around 5% of the universe. It turns out that roughly 68% of
744 the universe is dark energy, which is not considered by the SM.

745 Dark energy is an unknown type of energy postulated to explain the ob-
746 served accelerated expansion of the universe. This expansion is dominated
747 by a spatially smooth component with negative pressure called dark energy.
748 Modern cosmological measurements are based in supernovae, cosmic mi-
749 crowave background fluctuations, galaxy clustering and weak gravitational
750 lensing, and methods agree with a spatially flat universe with about 30%
751 matter (visible and dark) and 70% dark energy [52].

752 **Dark matter**

753 The rest of the energy content in the
 754 universe is the matter. Dark matter (DM) adds up for approximately
 755 85% of all matter and 27% of all en-
 756 ergy. This matter is called dark be-
 757 cause it does not interact with the
 758 electromagnetic field, so maybe a
 759 name such us invisible matter would
 760 have been more appropriate since
 761 rather than being dark it just does
 762 not emit or reflect light. The only
 763 way to interact with DM is via grav-
 764 itational interaction, which is bout
 765 25 orders of magnitud weaker than the weak force (as Table 1.1 shows).
 766 This is why DM is so difficult to detect. The SM does not provide a proper
 767 explanation but searches are being carrie and candidates such as weakly
 768 interacting massive particles (WIMPs) or axions have been proposed.



770 The existence of DM has been inferred through gravitational effects
 771 in astrophysical and cosmological observations. The rotational speed of
 772 the galaxies[53], the gravitational lensing[54] and the CMB angular spec-
 773 trum[55] are some examples of phenomena that cannot be explained with
 774 general relativity unless there is more present matter what it is seen.

775 Although the vast majority of scientific community accepts dark matter
 776 existence, alternative explanations for the observed phenomena have sug-
 777 gested. Most of these model consists in modifications of GR. The search
 778 of DM at particle colliders, which is focussed on large missing transverse
 779 energy signatures, have not result in any observation. Nevertheless, the ex-
 780 istence of a particle is never discarded, only its presence within the detector
 781 sensitivity limits.

782 **Unification of the strong interaction**

783 There are unification attempts to treat all interactions as one, with the same
 784 coupling constant and the same symmetry group⁹. In the same way the EW
 785 unifies QED and Weak forces, the grand unified theories (GUT) unifies all
 786 three interactions (QED, Weak and QCD) of the SM at high energies, where
 787 the coupling constants approach each other. Note that gravity is still left
 788 out, because it is much weaker than the other interactions.

⁹The most popular symmetry group for unification is $SU(5)$.

789 **Supersymmetry**

790 Originally motivated by the hierarchy problem, supersymmetry (SUSY) is
 791 an extension to the SM. In SUSY the equations for force and the equations
 792 for matter are identical and each SM particle has its supersymmetric partner
 793 “sparticle” from which differs by half spin unit. Therefore, for each SM
 794 fermion, the corresponding sfermion is a spin-0 scalar and hence a boson.
 795 Identically, there is a super-partner for each of the SM bosons. The gluons
 796 have the spin-half gauginos. The Higgs have a weak isospin doublet or spin-
 797 half Higgsinos ($\tilde{H}_{1,2}^0$ and \tilde{H}^\pm). The new particles interact through the forces
 798 of the SM but would have different masses

799 SUSY is not a theory but a principle and any theory with that property
 800 is said to be supersymmetric. So, there is not one but dozens of supersym-
 801 metric theories. A lot of focus has been put searching for supersymmetric
 802 particles but so far the supersymmetric partners have not been found, which
 803 is a good reason to be skeptical about SUSY. **maybe cite here some AT-**
 804 **LAS SUSY searches**

805 **Others**

806 The different problems mentioned hitherto are just some of the most relevant
 807 open questions that fundamental physics has not being able to answer yet.
 808 Nonetheless, there are many other issues whose discussion would need many
 809 pages and are outside the scope of this work. Even so, it won’t harm to list
 810 a few of them:

- 811 • Hierarchy problem: It is caused by the enormous distance between
 812 two fundamental physics scales: the EW scale ($\sim 10^2$ GeV) and the
 813 Planck scale ($\sim 10^{19}$ GeV).
- 814 • Strong \mathcal{CP} problem: It refers to the fact that, while QCD does not
 815 explicitly prohibit \mathcal{CP} violation in strong interactions, it has yet to be
 816 observed in experiments.
- 817 • Naturalness: It is the property that the dimensionless ratios between
 818 free parameters or physical constants appearing in a physical theory
 819 should take values of order unity. By looking at the parameters of the
 820 SM described in Section 1.1.7.1, it can be seen that the naturalness
 821 principle is not satisfied. For instance, the masses of the first gen-
 822 eration of fermions are in the range of 1 MeV while the top quark has
 823 a mass of 173 GeV. Though this is not a flaw in the theory itself, it is
 824 frequently seen as a sign of undiscovered principles hidden behind a
 825 more comprehensive theory.
- 826 • Composite Higgs models:

- Majorana neutrinos: It is not clear yet if neutrinos are Majorana particles, i.e. they are their own antiparticles ($\nu = \bar{\nu} = \nu_M$). Current experiments trying to solve this question are focused on neutrino-less double- β decay, which can occur only if neutrinos are Majorana particles.
- String theory: It is a theoretical framework in which fundamental point-like particles are understood as vibrational states of a more basic object, the so-called “string”. A string is a one-dimensional entity that can be either open (forming a segment with two endpoints) or closed (forming a loop) and may have other special properties. Despite being in development since the late 1970s, it has not been accepted nor discarded yet.

Most of theoretical concepts of the SM were in place by the end of the 1960s. With the discovery of the W and Z bosons at CERN in the mid 1980s and the Higgs boson in 2012, the SM has established itself as one of the major pillars of modern physics. The understanding of the universe at the most fundamental level is based in this theory, which has been tried to be summarised through the entire Section 1.1.

Despite its brilliance and success, the SM is not the ending of the story. As exposed above, there are far too many unanswered questions and loose ends. The HL-LHC (see Section ??) and the next generation of experiments will look for evidence of physics outside the SM in the next years.

Among the open questions, unresolved concerns and measurements to be completed, this research is focused on the top quark¹⁰. On one hand, contributions to the measurement of the polarisation of this quark are presented and, on the other hand, the study of the associated production of a single-top quark with a Higgs boson is present as well. Now that the basics of the SM have been settled, in the sections to come, the context of these two topics is being discussed.

1.2 Top quark

The top quark (t) or, for simplicity, just top is the up-type quark of the third generation of fermions. Sometimes called truth quark, its most distinctive feature is its huge mass, which is the largest among all fundamental particle particles. The left-handed top is the $Q = 2/3$ and $T_3 = +1/2$ member of the weak isospin doublet that also contains the bottom quark. The

¹⁰Here and in the following, the usage of the term top quark includes the top antiquark.

right-handed top quark is the $SU(2)_L$ weak isospin singlet ($Q = 2/3$ and $T_3 = 0$). Its phenomenology is driven by its large mass. The top quark is often regarded as a window for new physics since it provides a unique laboratory where to test the understanding of the SM.

Due to being so massive, its life time is very short ($\tau_t = 5 \times 10^{-25}$ s [54]). Actually, it is shorter than the hadronisation time ([cite](#)), this represents a unique opportunity to study quarks in free state, something that is very rare due to colour confinement, as explained in Section 1.1.4. In fact, the top quark is the only quark that can be investigated in isolation. Some of its properties, such as the spin information, can be accessed through its decay products and, consequently, be measured. This is the base to study its polarisation, a work that is contextualised in Section 1.2.4 and described in Chapter 4).

Another consequence of its large mass is that the top quark is the only quark with a Yukawa coupling (y_t) to the Higgs boson on the order of one; hence, a thorough understanding of its properties (mass, couplings, decay branching ratios, production cross section, etc.) can reveal crucial information on basic interactions at the electroweak symmetry-breaking scale and beyond. The main objective of this thesis is, precisely, the study of the top quark and Higgs boson interplay to, ultimately, help to determine if the y_t is that predicted by the SM or there is some \mathcal{CP} -violating phase that would affect the sign of the Higgs-top Yukawa coupling. The theoretical base for the understanding the associated production of a top quark and a Higgs boson given in Section 1.4 and the analysis investigating this matter is presented in Chapter 5.

887 Top quark mass

888

889 -> Top quark mass defines the stability of the EW vacuum. It is a key
890 factor to test the internal consistency of the SM.

891 -> m_{top} is a free parameter of the SM. It has to be determined experi-
892 mentally.

893 As discussed in Section 1.1.7.1, m_{top} is a free parameter of the SM. The
894 theory does not predict its value, hence it must be determined experimen-
895 tally. To derive the m_{top} from hadron collision data, two approaches are
896 explored:

- 897 • Direct measurements (also known as template methods) [56]: The
898 m_{top} is determined by reconstructing (fully or partially) the decay

899 products of one or more top quarks in a $t\bar{t}$ or single-top event¹¹. A
 900 comparison of the detector-level distribution with templates created
 901 with a MC generator is used to determine the mass. Analysing $t\bar{t}$
 902 events with lepton-plus-jets and dilepton topologies provides the most
 903 precise results. $\rightarrow m_t^{MC}$ with $O(480 \text{ MeV})$ precision.

- 904 • Indirect measurements[56]: Performed from measurements of cross-
 905 section. These methods rely on the dependence on the value of the
 906 m_{top} for the total or differential production cross sections for processes
 907 involving top quarks. $\rightarrow m_t^{pole}$ with $O(1 \text{ GeV})$ precision

908 The most precisely studied property of the top quark is its mass. The
 909 most recent results for the top quark mass measurements result in $m_{top} =$
 910 $172.76 \pm 0.30 \text{ GeV}$ [1]. This number is an average of the measurements at
 911 LHC with ATLAS ($172.69 \pm 66 \text{ GeV}$ [57]) and CMS ($172.6 \pm 3.5 \text{ GeV}$ at CMS
 912 [58]) and at Tevatron with CDF and D \emptyset (combined result: $174.30 \pm 0.89 \text{ GeV}$
 913 [59]). These values are measured from the kinematics of $t\bar{t}$ events¹².

914 Figure 1.9 summarises the measurements of ATLAS and CMS for m_{top}
 915 from direct top quark decay.

916 1.2.1 Top quark discovery

917 In 1973, Kobayashi and Maskawa postulated the possibility of a third
 918 generation of quarks to explain \mathcal{CP} violations in kaon decays[60]. To match
 919 the names of the up and down quarks, the new generation's quarks were
 920 given the names top and bottom. The GIM mechanism, which predicted
 921 the existence of the yet-to-be-discovered charm quark, was used to make
 922 this prediction. When the charm was observed [61], the GIM was integ-
 923 rated into the SM and the postulation of the third family, and thus the top
 924 quark, gained acceptance. Shortly after the charm, the bottom quark was
 925 discovered in the E288 experiment at Fermilab [62], reinforcing the idea of
 926 the existence of the top quark. However, due to its large mass, it took 18
 927 years to confirm the existence of the top.

928 The top quark was observed for the first time at Tevatron with the
 929 CDF [63] and D \emptyset [64] detectors via flavour-conserving strong interaction
 930 in 1995. Back then and until the start of LHC Run-1, Tevatron was the
 931 only accelerator powerful enough to produce top quarks.

¹¹In particle physics, an event is the result of a collision, as recorded by the experiment.

¹²This m_{top} results are sensitive to the top quark mass used in the MC generator that is usually interpreted as the pole mass.

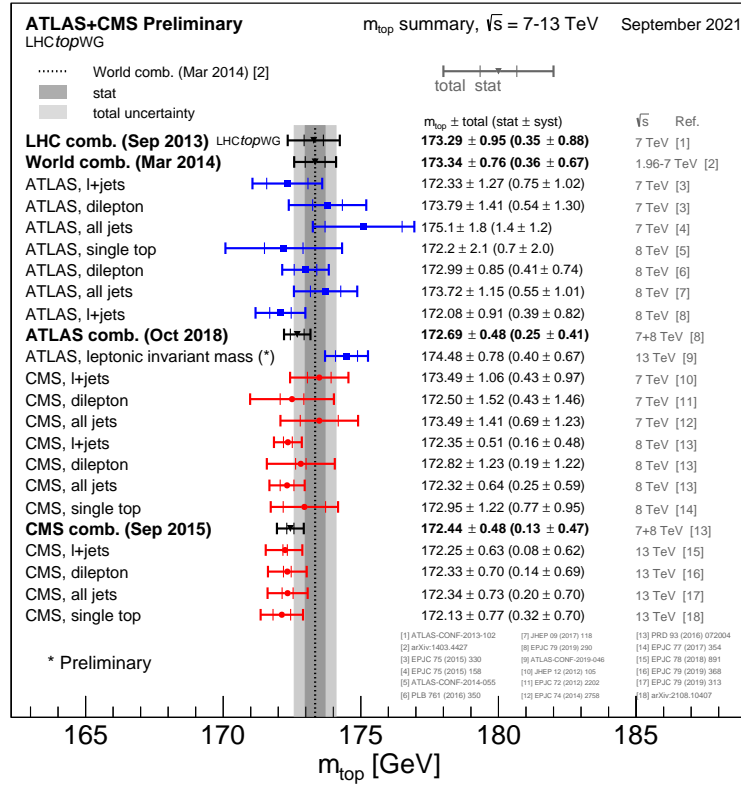


Figure 1.9: Summary of the ATLAS and CMS measurements from top quark decay. Results compared to LHC m_{top} combination.

932 1.2.2 Top quark production at LHC

933 The LHC is sometimes referred as a top quark factory due to its ability
 934 to produce such particles. In this collider, at pp collisions, the top quark
 935 is mainly produced via two mechanisms: through QCD in top and anti-top
 936 pairs ($t\bar{t}$), and by means of the Wtb vertex of EW in single-top quarks
 937 associated with other particles. Apart from the $t\bar{t}$ (Section 1.2.2.1) and
 938 single-top (Section 1.2.2.2) productions, the associated $t\bar{t} + X$ and four-top-
 939 quark productions (Sections 1.2.2.3 and 1.2.2.4 respectively) are presented
 940 as well.

941 Since the top quark production is si relevant at LHC, the top quarks
 942 often constitute a main background in other physics analysis and, as a result,
 943 a better understanding of this particle's properties will directly translate
 944 into improvements in those searches.

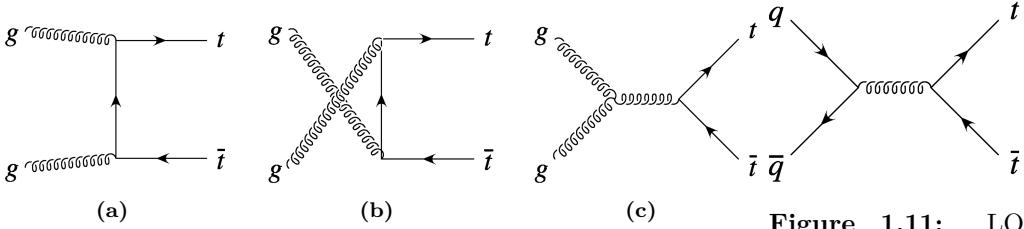


Figure 1.10: Representative Feynman diagrams of the LO processes contributing to the $t\bar{t}$ production through gluon fusion at LHC.

Figure 1.11: LO Feynman diagram for $t\bar{t}$ production via quark and anti-quark annihilation.

945 1.2.2.1 Top pairs

946 The production top and anti-top pair of quarks is the largest source of
 947 production of top quarks in hadron collisions. This process is one of the
 948 most important at LHC because it allows to precisely study the properties
 949 of the top quark. Additionally, due to the dominance of this production
 950 mode, the top-quark-pair production is also a major background in many
 951 searches for rare processes.

952 For the $p\bar{p}$ collisions at Tevatron or pp at LHC, the $t\bar{t}$ production is
 953 described by perturbative QCD. In this approach, a hard scattering process
 954 between the two hadrons is the result of an interaction between the quarks
 955 and gluons that constitute these hadrons. This model is described with
 956 detail in Section 2.2.7.

957 At LHC, the gluon fusion (Figure 1.10) dominates with a 90% of the $t\bar{t}$
 958 production. It is followed by the quark and anti-quark annihilation (Figure
 959 1.11), which accounts for a 10% of the the total top-quark-pair production.
 960 Due to its primordial importance for the physics programme of LHC, the
 961 theoretical calculations for the $t\bar{t}$ production are done to an accuracy of
 962 next-to-next-to-leading order (NNLO) in QCD [65] and measured by AT-
 963 LAS and CMS. Figure 1.12 shows the measurements for the $t\bar{t}$ production
 964 cross section ($\sigma_{t\bar{t}}$) at $\sqrt{s} = 13$ TeV. The measurements and the theory cal-
 965 culations are quoted at $m_{top} = 172.5$ GeV.

966 1.2.2.2 Single top

967 In addition to the top-quark-antiquark-pair production, the single-top-
 968 quark processes are of great importance to the study of the top quark prop-
 969 erties at the LHC. This mechanism has a cross section three times smaller
 970 than that of $t\bar{t}$ and are almost exclusively produced through the electroweak
 971 Wtb vertex. This is precisely the reason why single-top-quark production is

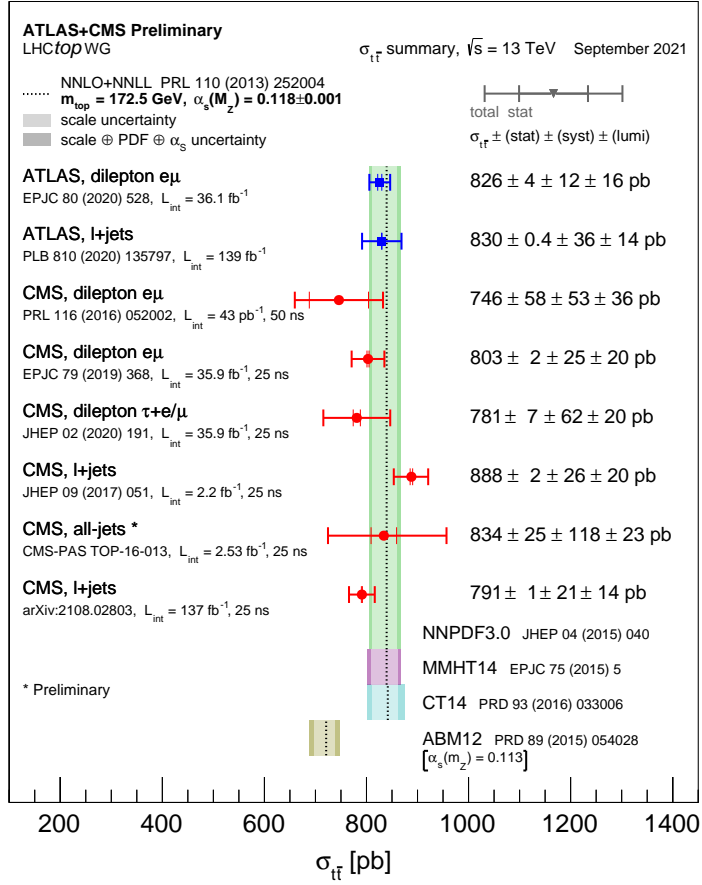


Figure 1.12: Summary of measurements $\sigma_{t\bar{t}}$ at 13 TeV compared to the exact NNLO QCD calculation complemented with NNLL resummation.

972 essential to gather information the Wtb interaction and to directly measure
 973 $|V_{tb}|$ at hadron colliders. The reason to decay and be produced from the
 974 bottom quark and not from strange or down quarks is because the CKM
 975 elements V_{ts} and V_{td} are much more smaller than V_{tb} being $|V_{tb}| = 0.99915$,
 976 $|V_{ts}| = 0.0403$ and $|V_{td}| = 0.00875$.

977 At LO, there are three production modes for single top, being the t -
 978 channel the dominant mechanism at the LHC with, approximately 70% of
 979 the single top quark cross section ($\sigma_{Single-t}$) at a $\sqrt{s} = 13 \text{ TeV}$. The other
 980 processes are the s -channel and the associated production tW production.
 981 Only t -channel and tW productions are relevant to the electroweak single
 982 top production at LHC.

983 **t -channel**

984 This production mode, involves the scattering of a light quark and a gluon

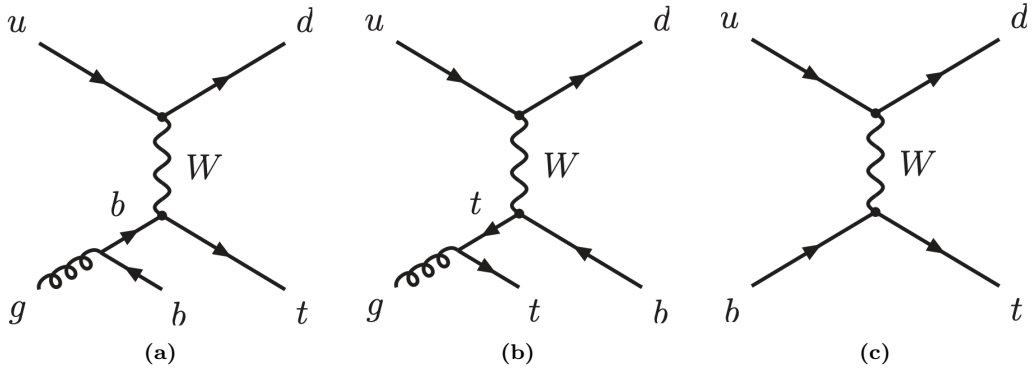


Figure 1.13: Representative Feynman diagrams for the single-top-quark production in the t -channel process.

from the proton sea as shown in Figure 1.13. Note that additional diagrams to those in Figure 1.13 are obtained by either replacing the u and d by a c and s quarks or by switching the light quarks in the fermion line. The diagrams for antitop production are the charge conjugate of the ones presented.

The measurements cross sections at 13 TeV for single-top ($\sigma_{t\text{-channel},t}$) and single-anti-top ($\sigma_{t\text{-channel},\bar{t}}$) quarks in the t -channel production are shown in Figure 1.14. The theoretical calculations at NLO for $\sigma_{t\text{-channel},t+\bar{t}}$ at 13 TeV are:

$$\begin{aligned}\sigma_{t\text{-channel},t} &= 136^{+4.1}_{-2.9}(\text{scale}) \pm 3.5(\text{PDF} + \alpha_s) \text{ pb}, \\ \sigma_{t\text{-channel},\bar{t}} &= 81.0^{+2.5}_{-1.7}(\text{scale}) \pm 3.2(\text{PDF} + \alpha_s) \text{ pb}, \\ \sigma_{t\text{-channel},t+\bar{t}} &= 217^{+6.6}_{-4.6}(\text{scale}) \pm 6.5(\text{PDF} + \alpha_s) \text{ pb}.\end{aligned}$$

These numbers have been obtained using HATHOR 2.1 [66][67].

The dominant process in the SM is the one in diagram 1.13a, while the one in 1.13b is included in order to form a gauge invariant set but its contribution is not very significative since for the gluon is easier to decay to $b\bar{b}$ pair than to a $t\bar{t}$ pair. These two $3 \rightarrow 2$ production modes are known as 4 Flavour Scheme (FS) because the proton is considered to be composed by five quark flavours (u, d, c and s) and is characterised by having a b quark in the final state. This final state b quark is sometimes referred as second b and it has a transverse momentum (p_T) distribution peaking around 2 or 3 GeV as can be seen in Figure 1.15. This is the reason why the final b quark from the gluon splitting frequently goes undetected, because it does not pass the p_T threshold of the detector.

The $2 \rightarrow 2$ process in 1.13c is known as 5FS because the proton is considered to be composed by five flavours of quarks (u, d, c and s) and it is characterised by having a b quark in the initial state. The simulations for

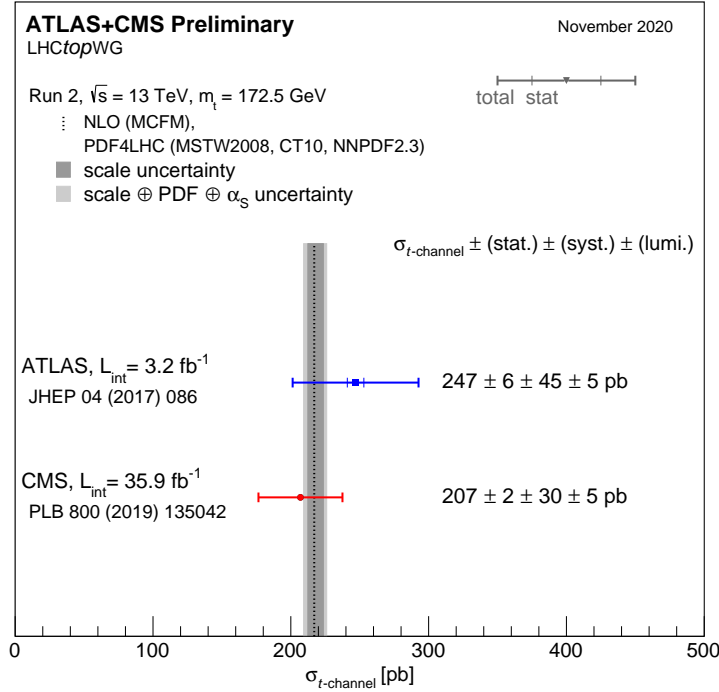


Figure 1.14: Summary of the ATLAS and CMS Collaboration measurements of the single top production cross-sections in the t -channel at 13 TeV.

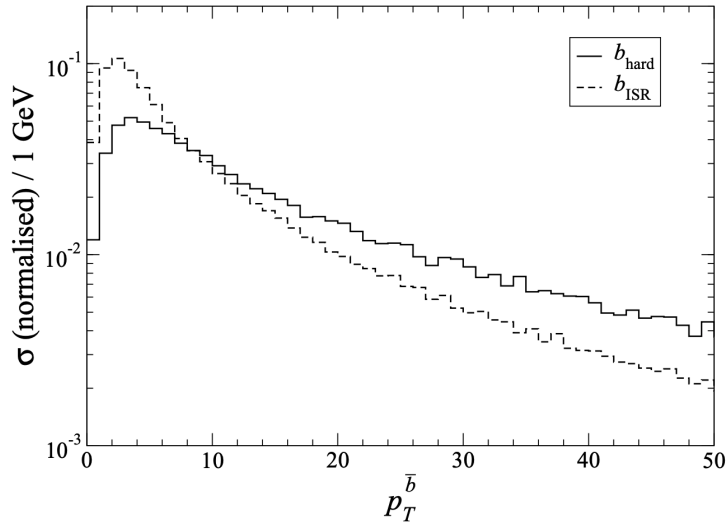


Figure 1.15: Normalised p_T distribution of the second b quark in the t -channel process, generated by Monte Carlo (MC) simulation [68].

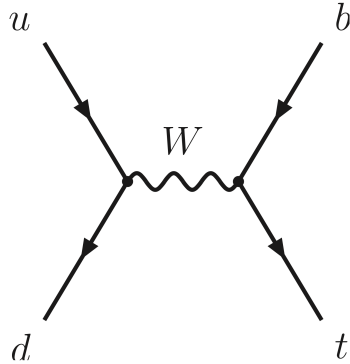


Figure 1.16: Representative Feynman diagram for the single-top-quark production in the *s*-channel.

1005 the 4FS and 5FS diagrams are produced separately and merged afterwards.
 1006 When adding the two contributions, some double-counting may appear due
 1007 to the overlap in the phase space so one has to be careful.

1008 **s-channel**

1009 The *s*-channel process for single-top is the one with less impact among
 1010 single-top production channels. It is depicted in Figure 1.16. This produc-
 1011 tion mode is also referred as the quark-antiquark annihilation or W^* process
 1012 and it is very similar to the Drell-Yann.

According to the LHC cross section group, at 13 TeV of center-of-mass energy, the cross sections for the single top and single anti-top production in the *s*-channel ($\sigma_{s\text{-channel}}$) are:

$$\begin{aligned}\sigma_{s\text{-channel}, t} &= 6.35^{+0.18}_{-0.15}(\text{scale}) \pm 0.9(\text{PDF} + \alpha_s) \text{ pb}, \\ \sigma_{s\text{-channel}, \bar{t}} &= 3.97^{+0.11}_{-0.09}(\text{scale}) \pm 0.15(\text{PDF} + \alpha_s) \text{ pb}, \\ \sigma_{s\text{-channel}, t+\bar{t}} &= 10.32^{+0.29}_{-0.34}(\text{scale}) \pm 0.27(\text{PDF} + \alpha_s) \text{ pb}.\end{aligned}$$

1013 Note that while at LHC the *s*-channel production has not been observed
 1014 at LHC, for Tevatron it was a significant part of the total single-top cross-
 1015 section.

Associated tW

Finally, the associated production of a single top quark with a W boson (sometimes referred as tW -channel) is represented by two the Feynman diagrams in Figure 1.18. To these two diagrams, the charge conjugate processes could be added to complete the tW mechanisms. The cross section for the associated tW is:

$$\sigma_{tW, t+\bar{t}} = 71.7 \pm 1.80(\text{scale}) \pm 3.40(\text{PDF} + \alpha_s) \text{ pb}.$$

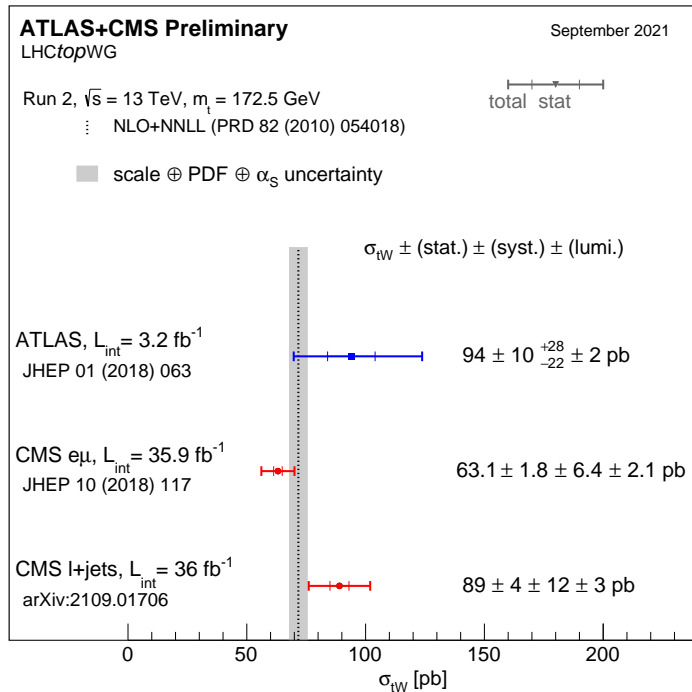


Figure 1.17: Cross-section measurements for the associated tW production boson performed by ATLAS and CMS at 13 TeV, and combined result compared with the NLO+NNLL prediction.

1016 This and all σ in the section are calculated for a top mass of $m_{top} =$
 1017 172.5 GeV and NLO in QCD with HATHOR v.2.1. The PDF and α_s un-
 1018 certainties are calculated using the PDF4LHC prescription [69] with the
 1019 MSTW2008 68% CL NLO [70][71], CT10 NLO [72] and NNPDF2.3 [73]
 1020 PDF sets, added in quadrature to the scale uncertainty.

1021 1.2.2.3 Associated $t\bar{t} + X$ production

1022 1.2.2.4 Four tops

1023 Figure 1.22

1024 1.2.3 Top quark decay

As advanced in the Section 1.2.2.2, due to the large V_{tb} element of the CKM matrix, the top quark decays almost entirely ($\sim 99.8\%$) thorough the medium of the Wtb vertex to a b quark and a W boson. The final state

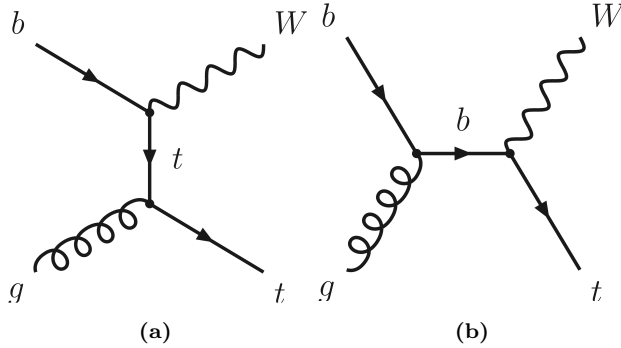


Figure 1.18: Representative Feynman diagrams for the single-top-quark production in association with a W boson.

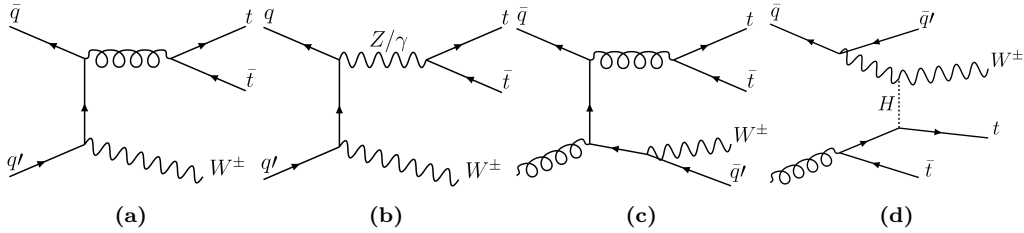


Figure 1.19: Representative Feynman diagrams for $t\bar{t}W$ production. Left diagrams show the $\bar{q}q' \rightarrow t\bar{t}W$ processes and right ones the $\bar{q}q \rightarrow t\bar{t}Wq'$ production.

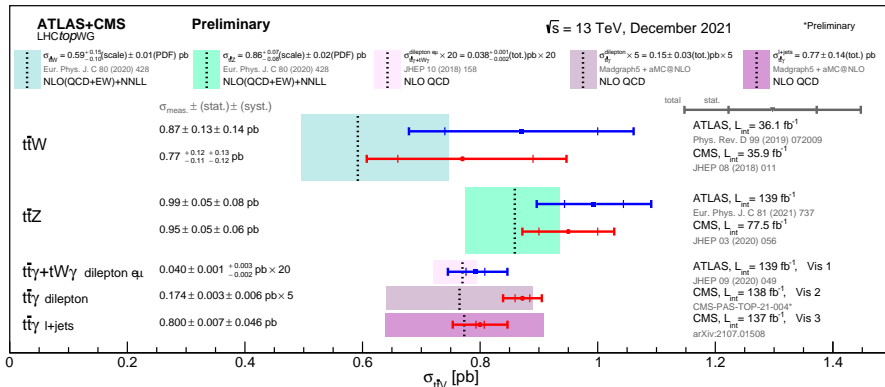


Figure 1.20: Summary of the ATLAS and CMS measurements of the $t\bar{t} + X$ production cross-sections at 13 TeV. Here $X = W, Z$ and γ .

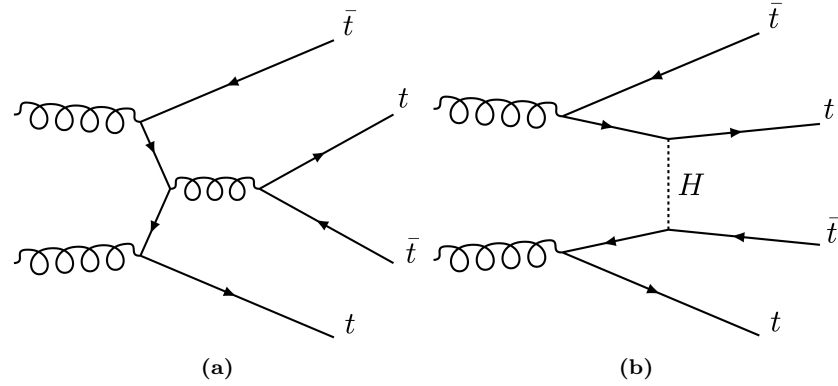


Figure 1.21: Representative Feynman diagrams for the $gg \rightarrow t\bar{t}t\bar{t}$ production.

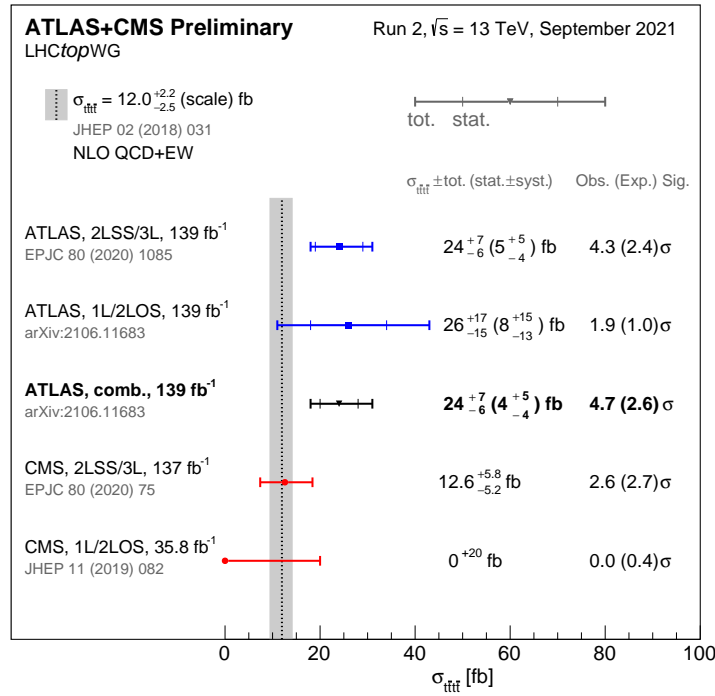


Figure 1.22: Summary of the ATLAS and CMS measurements of the $t\bar{t}$ production cross-sections at 13 TeV in various channels

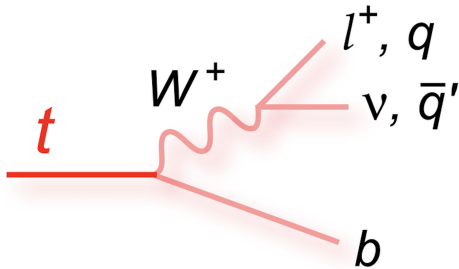


Figure 1.23: Decay of a top quark to a b quark and a W boson. The W boson can decay either leptонically to a neutrino and a lepton or hadronically to a pair of quarks. In the hadronic W decay, a jet triplet is formed along with the b quark.

decay is classified according to the subsequent decay of the W boson. As W are massive vector bosons, its lifetime is very short ($\tau_W \approx 3 \times 10^{-25}$ s). For the W^+ , the decay modes are:

$$\begin{aligned}
 W^+ &\rightarrow e^+ \nu_e & (10.71 \pm 0.16)\% \\
 W^+ &\rightarrow \mu^+ \nu_\mu & (10.63 \pm 0.15)\% \\
 W^+ &\rightarrow \tau^+ \nu_\tau & (11.38 \pm 0.21)\% \\
 W^+ &\rightarrow q\bar{q} \text{ (hadrons)} & (67.41 \pm 0.27)\% \\
 W^+ &\rightarrow \text{invisible} & (1.4 \pm 2.9)\%
 \end{aligned}$$

For the conjugate processes involving the W^- , the branching ratios (BR) are the same. Therefore, the W decay and consequently the t decay can be classified either as leptonic or hadronic. The decay chain of the top quark is represented in Figure 1.23. Due to its large mass, the W can decay to any quark except the top quark. For a certain decay mode, the BR is defined as the fraction times that the particle decays in that particular mode with respect to total possible decays.

1.2.4 Top quark polarisation

Angular measurements in ATLAS:

- Top polarisation: how the top is produced
- Helicity fractions: how the top decays
- Spin correlation: information between produced top-quarks. Provides information about quantum entanglement.

For polarisation: Top polarised in direction of spectator quark Define 3
Polarisation directions: $\{P_{xt}, P_{xy}, P_{zt}\}$ Lepton direction used as spin analyser (α_l)

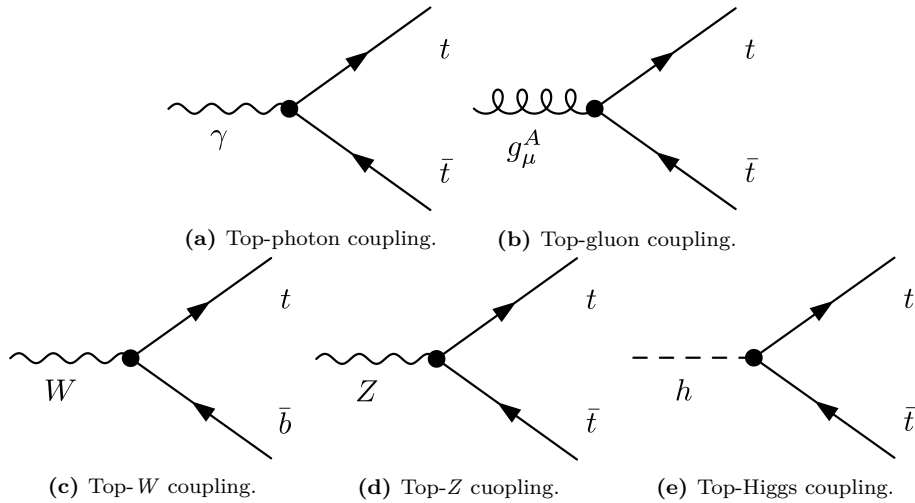


Figure 1.24: Top quark coupling to SM bosons.

1041 In the single top t -channel production, the top quark is polarised due
 1042 to left-handed W -coupling. Top-quark spin points in the direction of the
 1043 spectator-quark(q')

1044 1.2.5 Top quark physics

1045 **Probably this section is not necessary since the physics are**
 1046 **mostly explained above.** The top quark couples directly to all SM vector
 1047 (γ , W^+ , W^- , Z , g) and scalar (H) bosons. For both photons and gluons,
 1048 the interaction is described by a vectorial fermion-gauge coupling $\bar{\Psi}\Psi A_\mu$.
 1049 From boson-fermion interacting term of the \mathcal{L}_{QED} in 1.9, the coupling of
 1050 the top quark to photons (Figure 1.24a) has a strength of $eQ\gamma^\mu = \frac{2}{3}e\gamma^\mu$.
 1051 Meanwhile, for the top-gluon coupling (Figure 1.24b), the expanded form
 1052 of the gluon-fermion term in the \mathcal{L}_{QCD} of 1.31 gives the $g_s \frac{\lambda_a}{2} \gamma^\mu$.

1053 For the charged weak current only the only the left-handed top couples
 1054 to the W^\pm with coupling. This is done via the Wtb vertex with a strength
 1055 of $g\gamma^\mu(1 - \gamma^5)V_{tb}$ (Figures 1.23 and 1.24c). The value of V_{tb} is given in Table
 1056 1.3. The top couples to the Z bosons (Figure 1.24d) with unequal left and
 1057 right-handed components, $\frac{ig}{2\cos\theta_W}\gamma^\mu(v_t - a_t\gamma^5)$. Being $v_t = 1/2 - 2Q_t\sin^2\theta_W$
 1058 and $a_t = 1/2$. Finally, for the Higgs boson (Figure 1.24e), the top quark
 1059 couples with a Yukawa type interaction $\bar{\Psi}\Psi\phi$ with a strength $y_t = \frac{\sqrt{2}m_{top}}{v}$,
 1060 as equation 1.39 states. All of these couplings are flavour-conserving, with
 1061 the exception of the charged-current interaction with the W bosons.

1062 1.3 Higgs boson

1063 Following the top quark, the Englert-Brout-Higgs-Guralnik-Hagen-
 1064 Kibble-Higgs boson or, for simplicity, Higgs boson (H) or just Higgs is
 1065 the most massive particle in the SM with a mass of $m_H = 125.25 \pm 0.17$
 1066 GeV [2]. The value provided by [2] is an average of the ATLAS com-
 1067 bined measurement ($m_H = 124.86 \pm 0.27$ GeV [74]) and the CMS results
 1068 ($m_H = 125.46 \pm 0.16$ [75]).

1069 The Higgs boson was the final piece in the SM puzzle. Its existence
 1070 was theorised in 1964 by three independent groups: Englert-Brout [76],
 1071 Higgs [77] and Guralnik-Hagen-Kibble [78], and its discovery meant one of
 1072 the greatest successes of the SM. This theory was not only able to calculate
 1073 with great precision the physics but also predicted the existence of a particle
 1074 that was found later (see 1.3.1).

1075 In the SM, fundamental particles acquire mass through their interactions
 1076 with the Higgs fields. It is important to note that not all mass is related to
 1077 the Higgs mechanism. For instance, the mass of the proton does not come
 1078 from the interaction of its components with the Higgs but from the kinetic
 1079 energy of the particles that compose the proton.

1080 1.3.1 Higgs boson discovery

1081 Any particle physicist enthusiast remembers July 4th of 2012 pretty
 1082 well, it was LHC experiments ATLAS [79] and CMS [80] who announced
 1083 the discovery of a massive state H with the properties expected for the
 1084 Higgs boson.

1085 Both the ATLAS and CMS Collaborations reported excesses of events
 1086 for 2011 ($\sqrt{s} = 7$ TeV and $\mathcal{L} = 4.8 \text{ fb}^{-1}$) and 2012 ($\sqrt{s} = 8$ TeV and $\mathcal{L} = 458 \text{ fb}^{-1}$)
 1087 datasets of proton-proton collisions. This surplus of events was compatible
 1088 in its production and decay with the SM Higgs boson in the mass region
 1089 $m_H \in [124, 135]$ GeV with significances of 2.9σ for ATLAS and 3.1σ for
 1090 CMS. At Tevatron (circular proton-antiproton collider at Fermilab), the
 1091 experiments CDF [81] and D \emptyset [82] also reported an excess in the mass
 1092 region $m_H \in [120, 135]$ GeV.

1093 1.3.2 Higgs boson production at LHC

1094 One of the reasons why the Higgs boson was found the latest among
 1095 SM fundamental particles is because it is a fairly heavy particle and, hence,

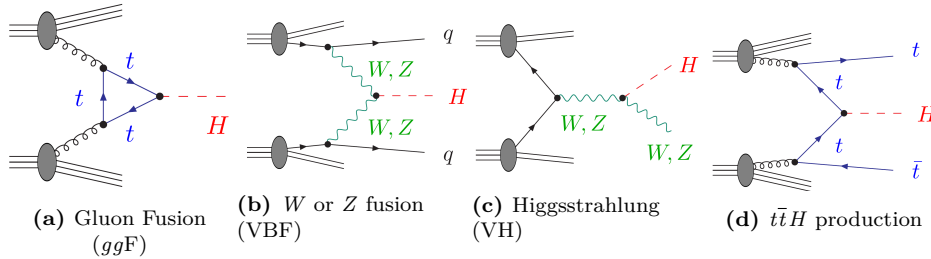


Figure 1.25: Lowest-order Feynman diagrams for the dominant production mechanisms of a Higgs boson at hadron colliders.

it was necessary a lot of energy to produce it. Even though that colliders such us SLAC or LEP had enough energy, they were colliding electrons and positrons and, since the coupling of the Higgs to fermions is proportional to the fermions mass, the process $e^- e^+ \rightarrow H$ processes is highly suppressed¹³ and, for this reason, there were not enough statistics of events with a Higgs boson. The most favoured way of producing a Higgs boson is trough the mediation of the heaviest fundamental particles in the SM because these have the strongest couplings with the Higgs and, consequently, the greater cross section.

The four most dominant processes for Higgs boson production at LHC are summarised in Figure 1.25:

- **Gluon Fusion (ggF):** This channel is depicted in Figure 1.25a and, as the diagram shows, the process $gg \rightarrow H$ has to be mediated by a massive fermion loop. This due to the fact that there is no direct gluon-Higgs coupling within the SM. Although in principle all quarks should be included in the loop, in practise it is the top quark the one doing so because its coupling to the Higgs boson is 35 times stronger than the next-heaviest fermion, the bottom quark.

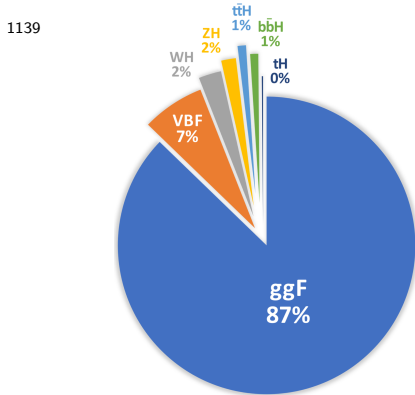
Due to the abundance of gluons in pp collisions, the ggF is very favoured at LHC.

- **Vector Boson Fusion (VBF):** The second most important is the radiation by the incoming quarks of a W or Z vector bosons that fuse to from a Higgs as Figure 1.25b illustrates. The vector bosons of the process $V\bar{V} \rightarrow H$ are originated from initial state quarks which scatter thorough the final state (changing its flavours in the case of W fusion) producing two forward jets.

¹³The dominant Higgs production in $e^- e^+$ annihilation is the so called Higgsstrahlung, an s -channel process in which the H is produced in association to a Z boson similarly to Figure 1.25c.

- **Higgsstrahlung (VH):** There is another significant contribution involving the W or Z bosons, the Higgsstrahlung or associated WH or ZH production. Here, a, off-shell W or Z (formed from the annihilation of two quarks) radiate a Higgs boson via $V^* \rightarrow VH$. Figure 1.25c depicts the VH associated production.
- **Quark-pair associated production ($q\bar{q}H$):** In this mode, the Higgs is produced from a $q\bar{q}$ pair via $q\bar{q} \rightarrow H$ with a $q\bar{q}H$ final state. Typically, the involved quark pair is either a $b\bar{b}$ or $t\bar{t}$. In the case of $t\bar{t}$ (Figure 1.25d), the top quarks decay before hadronising, leading to a high multiplicity final state.
- **Associated Higgs boson and single-top quark (tHX):** This sub-dominant contribution can be either a tHq or a tWH .

The cross section of the different procedures for Higgs boson production at $\sqrt{s} = 13$ TeV are shown in Figure 1.26 as a function of m_H . For Figure 1.26a, the σ_{tH} accounts for the t -channel and s -channel but not the tW -channel. Assuming a $m_H = 125.2$ GeV, the cross-sections for Higgs production are [83]:



$$\begin{aligned}\sigma_{ggF} &= 48.5^{+2.2}_{-3.3} \text{ pb} \\ \sigma_{VBF} &= 3.78 \pm 0.05 \text{ pb} \\ \sigma_{WH} &= 1.37 \pm 0.03 \text{ pb} \\ \sigma_{ZH} &= 0.89^{+0.04}_{-0.03} \text{ pb} \\ \sigma_{t\bar{t}H} &= 0.5^{+0.03}_{-0.05} \text{ pb} \\ \sigma_{b\bar{b}H} &= 0.49^{+0.10}_{-0.11} \text{ pb} \\ \sigma_{tHX} &= 0.09 \pm 0.01 \text{ pb}\end{aligned}$$

1.3.3 Higgs boson decay

The Higgs boson has a very short lifetime ($\tau_H = 1.6 \times 10^{-22}$ s [83]) and, hence, is always detected through its decay products. Despite the expected large Yukawa coupling between the Higgs boson and the top quark, the $H \rightarrow t\bar{t}$ is forbidden because the $m_H < 2m_{top}$. Consequently, the most prominent decay mode is the $H \rightarrow b\bar{b}$ followed by the $H \rightarrow W^+ W^-$. For the rest fermionic decays, the decay rates are ordered by the fermion mass. Regardless of the expected large coupling between the weak force bosons and the Higgs, the $H \rightarrow VV^*$ is suppressed due to the requirement that one vector boson has to be produced off-shell.

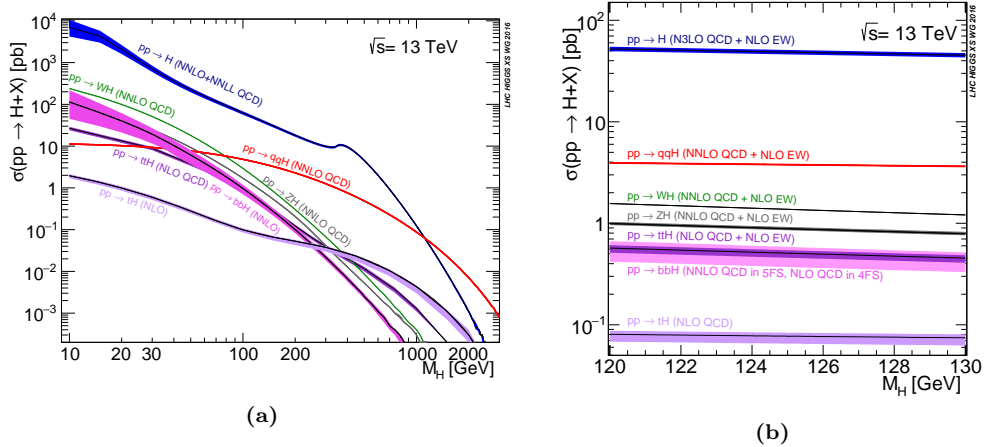
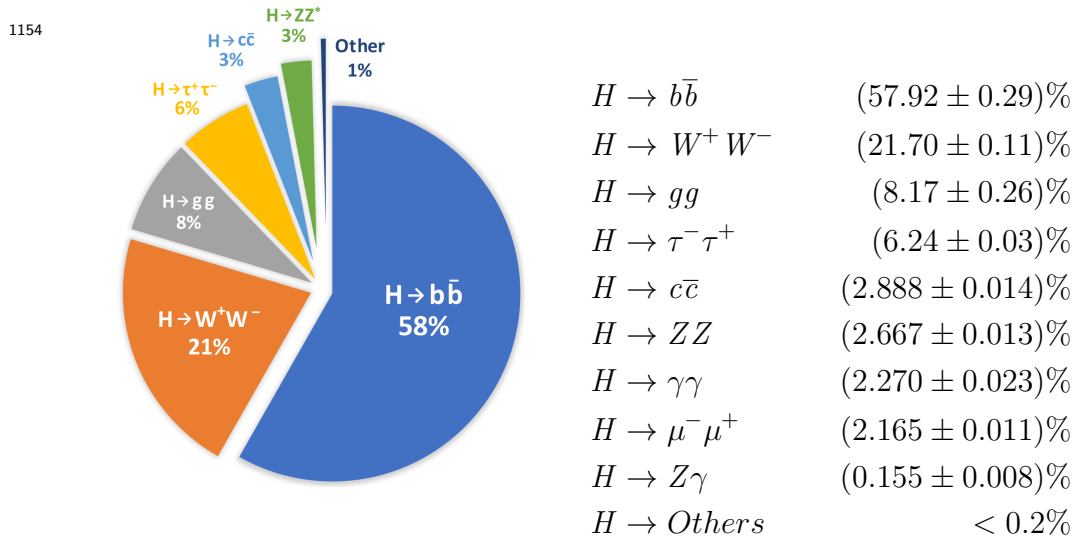


Figure 1.26: Higgs boson production cross sections as function of m_H at $\sqrt{s} = 13$ TeV [83].

Add some diagrams of the Higgs decay modes

For the analysis carried in this thesis, are of particular the decays $H \rightarrow W^+ W^-$, $H \rightarrow ZZ$ and $H \rightarrow \tau^-\tau^+$. Sorted by its importance and assuming a $m_H = 125.2$ GeV, the BR for the Higgs are [84]:



1.3.4 Higgs boson physics

Work in progress

The gauge symmetry is broken is broken by the vacuum, triggering the EW Spontaneous Symmetry Breaking (SSB). This means that the symmetry group of the EW sector, $U(2)_L \otimes U(1)_Y$.

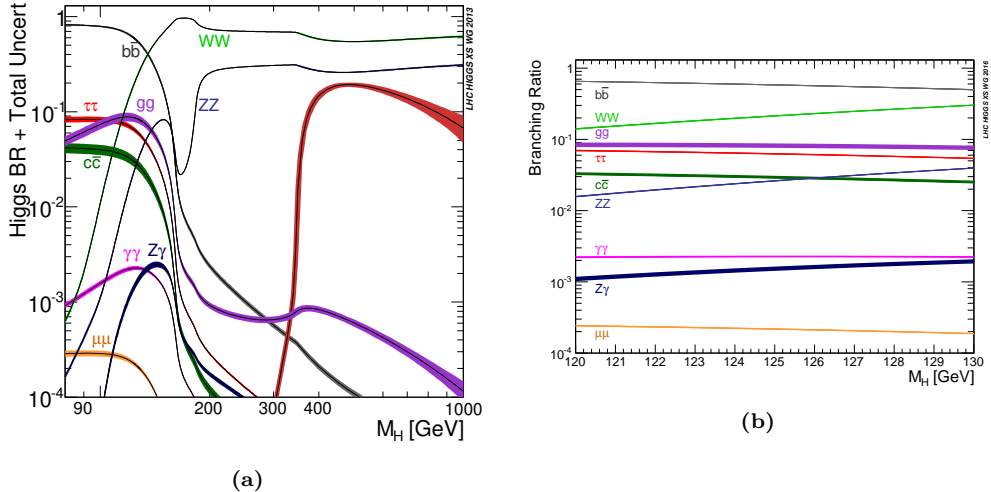


Figure 1.27: Standard Model Higgs boson decay branching ratios as function of m_H at $\sqrt{s} = 13$ TeV citeLHCIGGSSWG2013.

$$SU(3)_C \otimes SU(2)_L \otimes U(1)_Y \xrightarrow{\text{SSB}} SU(3)_C \otimes U(1)_{QED}$$

Production and decay rates, constrains on its couplings: <https://arxiv.org/abs/1606.02266>

The Higgs mass is given by $m_H = \sqrt{\lambda/2v}$, being v the vacuum expectation value of the Higgs field and λ the Higgs self-coupling.

Electro weak symmetry breaking [85]: <https://arxiv.org/pdf/1512.08749.pdf> In this paper the Yukawa coupling of the top is introduced, link it with the tHq paper.

1168 Work in progress

1169 1.4 Top quark and Higgs boson interplay

1170 So far, the couplings of the Higgs boson to the SM particles have been
 1171 found to be proportional to the mass of these particles. Since the top quark
 1172 is the most massive particle and the coupling of Higgs to SM particles is
 1173 uniquely determined by the mass of these particles, the Yukawa coupling
 1174 between the top quark and the Higgs boson (y_t) is expected to be the
 1175 greatest among all fermions and, hence, its study is of crucial importance,
 1176 as it is discussed in references [86][87] and developed in the succeeding
 1177 sections.

1178 The production of a pair or top quarks along with a Higgs boson ($t\bar{t}H$)
 1179 it is possible to measure the absolute value of y_t . This process has the

advantage of being the leading mechanism to produce the Higgs together with the quark top. At $\sqrt{s} = 13$ TeV it has a cross section of **poner cálculos del SM para $\sigma_{t\bar{t}H}$** (the definition of cross section can be found in Section 2.2.5).

Despite having a very much lower cross section than $t\bar{t}H$ (**poner números**), the Higgs boson production alongside a single top quark (tHq or tH) brings valuable information, specially regarding the sign of the Yukawa coupling. Note that the sign of y_t is not physical by itself but the relative sign compared to the coupling of the Higgs to weak¹⁴ boson is, in deed, physical [86]. This is explored with more detail in 1.4.2.

A change in the Yukawa sign and/or absolute value with respect to its SM value would signal an origin of the fermion masses different from the described by the EWSB because the relative sign of the Higgs coupling to fermions and gauge vector bosons is crucial for recovering the unitarity and renormalizability of the theory s[88].

1195 All section 1.4 is work in progress

1196 $\rightarrow \mathcal{CP}$ Properties of Higgs Boson Interactions with Top Quarks in the
 1197 tH and $t\bar{t}H$ processes at ATLAS: <https://inspirehep.net/literature/1790698>
 1199

1200 Only 1% of all Higgs bosons are produced in association with top quarks,
 1201 the observation of such processes is very challenging. Notably, it is a immensely ambitious task to measure the associated production of a Higgs
 1203 with a single top which has an extremely low cross section as can be seen
 1204 in Figure 1.26b.

1205 1.4.1 $t\bar{t}H$

1206 The first associated production of a Higgs boson with a pair of top
 1207 quarks was observed in 2008 by ATLAS [89] and CMS [90]. This process
 1208 marked a significant milestone for the field of high-energy physics because
 1209 it helped establishing the first direct measurement of the tree-level coupling
 1210 of the Higgs boson to the top quark, which interacted with the predicted
 1211 strength.

1212 The associated production of H with top quark pair has been studied by
 1213 ATLAS and CMS previously during Run-1 at $\sqrt{s} = 7$ TeV and 8 TeV [91]
 1214 [92] and Run-2 [**buscar $t\bar{t}H$ en Run-2**]

¹⁴The coupling of the Higgs to the gauge bosons is taken as positive.

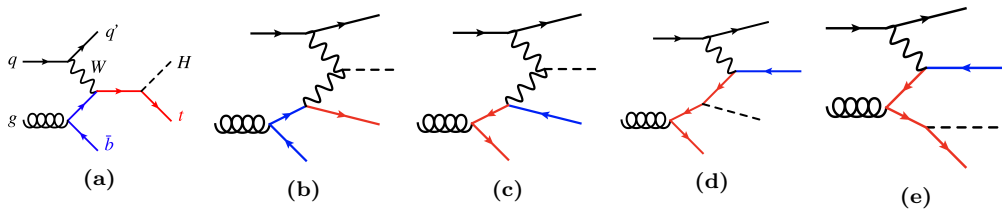


Figure 1.28: LO Feynman diagrams for t -channel tH production in the 4FS.

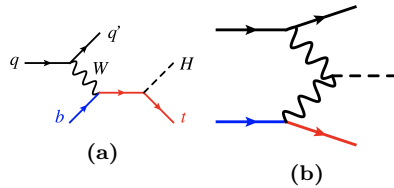


Figure 1.29: LO Feynman diagrams for t -channel tH production in the 5FS.

1.4.1.1 $t\bar{t}H$ Standard Model

1.4.1.2 $t\bar{t}H$ Charge-Parity

1.4.2 tHq

The tH production is divided in tHq and tWH .

1.4.2.1 tHq production modes

At LO, the production of a Higgs boson in association with a single top quark (tHq) in pp collisions is classified in three groups according to the virtuality of the W boson. These groups are: t -channel production, s -channel production and associated production with an on-shell W boson. This categorisation is the same as for the single-top-quark (Section 1.2.2.2), which makes sense since the tH associated production is, basically, a single-top-quark process in which a Higgs boson is radiated either from the W or the top.

In the t -channel production modes are classified in 4FS and 5FS as it is done for the single-top case. The 4FS and the 5FS modes are shown in Figures 1.28 and 1.29 respectively. For the 4FS modes, the diagrams in which the gluon decays to a top pair (1.28c, 1.28d and 1.28e) contribute less than the ones in which it does to a $b\bar{b}$ (1.28a and 1.28b).

Poner las tablas para las cross section de Demartin [93] para t -channel y s -channel

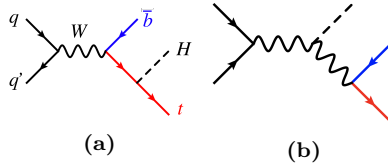


Figure 1.30: LO Feynman diagrams for s -channel tH production in the 5FS.

Since the s -channel contribution is so small to the total cross section of the tHq process,

For tH and single-top-quark production at colliders, the 5FS calculations are easier than the 4FS due to the lesser final state-multiplicity and simpler phase space. This is why in the 5FS the single-top production is known at NNLO while the 4FS this is done only for NLO. Another advantage of the 5FS is that the t -channel, s -channel and associated tWH production do not interfere until NNLO. Contrary, the in 4FS, the t -channel at NLO and s -channel at NNLO can interfere. Nevertheless, this interferences are very small and can be neglected [93].

Poner algo in información del tWH production mode para tH
y The tWH production is a background in the tHq analysis.

In reference 1.31 is shown that the shapes of the distributions of most observables in the s -channel differ significantly from those of the t -channel. So, even though the total cross section of the tHq production with the s -channel is much more smaller than the one for t -channel, one could think that including the s -channel in the analysis would increase the precision. This is not the case because the LHC is not sensible for to the tHq production via s -channel. In fact, not event the s -channel-single-top production (without any associated Higgs boson) has been found at LHC.

Summarise production modes described in [93]

tHq sensibility to y_t

As already commented in the introduction of the Section 1.4, the main interest of the tHq process is that it is among the few processes in the LHC that are sensible to the relative size and phase between the couplings of the Higgs top and the Higgs to the gauge bosons. The other mechanisms to determine this relative sign are $H \rightarrow \gamma\gamma$ and $gg \rightarrow ZZ$. This is due to the fact that in the SM the tHq production of the where the H couples to the W (Figure 1.31 right) interfere destructively with those in which the H is radiated from the top (Figure 1.31 left). As it is later explained in Section 2.2.5, the cross section is proportional to the square of the matrix element, \mathcal{M} and if there are several diagrams for a same process, the matrix elements

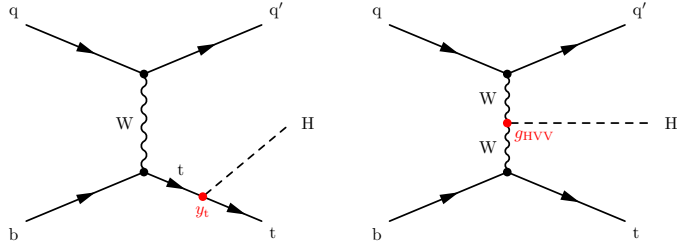


Figure 1.31: Representative LO Feynman diagrams for the t -channel tHq associated production, where the Higgs boson couples either to the top quark (left) or the W boson (right)

have to be summed before squaring leading to interference terms. For the tHq production

$$\sigma_{tHq} \propto |\mathcal{M}_{qq \rightarrow tHq}|^2 = |\mathcal{M}_{qq \rightarrow tHq_{WH}} + \mathcal{M}_{qq \rightarrow tHq_{tH}}|^2 \quad (1.40)$$

When squaring the scattering amplitude, the destructive interference¹⁵ term decreases the σ_{tHq} . This behaviour makes the tHq cross section exceptionally sensible to the departures of y_t from the SM predictions. Typically, the destructive interference yields a reduction in the rate as compared to the contribution from each individual diagram by about an order of magnitude [94]. Therefore, in the presence of non-SM new physics, a positive relative sign between the tH and the WH couplings would imply that the amount of tHq events recorded should increase a factor of ~ 13 over the SM expectations, surpassing the $t\bar{t}H$ production [95].

The tHq production has been studied at LHC Run-1 by CMS [39]

[Usar los papers the \$tHq\$ de CMS la sección 5 de Demartin \[93\]](#)

1.4.2.1 tH Standard Model

1.4.2.2 tH Charge-Parity

1.4.2.3 ATLAS and CMS results

In order to gather the necessary information, the widest possible campaign of measurements has to be undertaken, including all the different Higgs decay modes. In this context, the scope of this thesis is the study of the production tH with a final state characterised by two light leptons (ℓ), i.e. electrons (e^\pm) or muons (μ^\pm), and one hadronically decaying tau lepton

¹⁵By destructive interference is meant that the relative sign between $\mathcal{M}_{qq \rightarrow tHq_{WH}}$ and $\mathcal{M}_{qq \rightarrow tHq_{tH}}$ is negative.

₁₂₇₅ (τ_{had}). This signature is usually referred as dileptau or lep-had channel and
₁₂₇₆ is denoted by $2\ell + 1\tau_{\text{had}}$.

¹²⁷⁷ Chapter 2

¹²⁷⁸ **The ATLAS experiment at the 1279 Large Hadron Collider of 1280 CERN laboratory**

¹²⁸¹ The work developed in this thesis is framed in the context of the ATLAS
¹²⁸² detector, a general-purpose particle physics detector registering the events
¹²⁸³ originated from the collisions produced by the largest and most powerful
¹²⁸⁴ particle accelerator built up to this date, the LHC. This experimental setup
¹²⁸⁵ is located in one of the largest and most renowned centres for scientific
¹²⁸⁶ research in the world, the CERN.

¹²⁸⁷ This chapter is devoted to the introduction of the CERN laboratory and
¹²⁸⁸ a description of the technical design of LHC and ATLAS. The CERN or-
¹²⁸⁹ ganisation is presented through an overview of its history, its achievements
¹²⁹⁰ and some of the most relevant research projects carried out currently. The
¹²⁹¹ essential technical aspects of the LHC machine design are covered. The
¹²⁹² distribution and functioning of the accelerator complex and the main exper-
¹²⁹³ iments conducted at LHC are summarised as well. Finally, a full overview
¹²⁹⁴ of the different components of the ATLAS detector is exposed, presenting
¹²⁹⁵ the specific features of each of its parts.

¹²⁹⁶ 2.1 CERN

¹²⁹⁷ The European Organization for Nuclear Research, known as CERN, is
¹²⁹⁸ the largest particle physics laboratory in the world. The convention estab-
¹²⁹⁹ lishing CERN was ratified in 1954. Its name is derived from the French
¹³⁰⁰ acronym *Conseil Européen pour la Recherche Nucléaire*, which was the pro-
¹³⁰¹ visional body designated in 1952 to foster the fundamental physics research

1302 in Europe, and the acronym has been maintained until CERN’s foundation.
1303 Initially formed by 12 member states, now it has 23 member states and
1304 many non-European countries involved in different ways such as associate
1305 members, partners and observers [96].

1306 The main site of the laboratory is located at Meyrin, a municipality of
1307 the Canton of Geneva (Switzerland), at the Franco–Swiss border. There
1308 are other sites in the vicinity of the Meyrin site, being the most relevant the
1309 Prévessin Site, the CERN’s second-largest site, straddling the communes of
1310 Prévessin-Moën (France).

1311 Since its beginning, CERN’s objective has been helping to uncover what
1312 the universe is made of and how it works. CERN started its first accelerator,
1313 the Synchrocyclotron, on 1957 and rapidly observed the electron decay of
1314 the pion for the very first time [97]. Thereafter, the laboratory has con-
1315 tinued contributing to not only particle and nuclear physics but also more
1316 technical fields. For instance, one of the most important achievements made
1317 through CERN experiments is the discovery in 1973 of neutral currents in
1318 the Gargamelle bubble chamber installed in the Proton Synchrotron (PS)
1319 [98]. This observation was an indirect evidence for the existence of the Z
1320 boson and ten years later, in 1983, CERN announced the discovery of the
1321 Z and W bosons [99]. This finding was done at the UA1 and UA2 ex-
1322 periments, located within the Super Proton Synchrotron (SPS), and it was
1323 awarded with the laboratory first Nobel Prize in 1984. Other major suc-
1324 cesses of CERN were the determination of the number of light neutrino
1325 families at the Large Electron-Positron Collider (LEP) on 1995 [100] and
1326 the creation for the very first time of antihydrogen atoms in 1995 at the
1327 PS210 experiment [101]. More crucial accomplishment followed such as the
1328 discovery during the 1990’s of \mathcal{CP} violation by NA31 [102] and NA48 ex-
1329 periments [103]. And, in 2012, the Higgs boson discovery by ATLAS and
1330 CMS[79] [80], a fundamental test for the robustness of the SM as described
1331 in Section 1.3.1. More recently, in 2015, a state consistent with a pentaquark
1332 was observed at LHCb [104].

1333 Currently, a wide diversity of projects are carried at CERN being the
1334 most renowned of them the LHC and its experiments which are described in
1335 more detail in Section 2.2. In addition, fixed-target experiments, antimatter
1336 experiments and experimental facilities make use of the LHC injector chain.
1337 The main fixed-target experiments at CERN are the Antiproton Decelerator
1338 (AD) [105] for slowing antiprotons for the antimatter factory [106] and the
1339 On-Line Isotope Mass Separator (ISOLDE) facility for short-lived ions [107].
1340 The world’s first proton-driven plasma wakefield acceleration experiment is
1341 also at CERN, the Advanced Proton Driven Plasma Wakefield Acceleration
1342 Experiment (AWAKE) [108]. In the International Space Station (ISS), the

1343 Alpha Magnetic Spectrometer (AMS) tries to observe dark matter [109].
1344 The research programme at CERN covers topics from the basic structure
1345 of matter to cosmic rays, and from the Standard Model to supersymmetry.

1346 Important breakthroughs and advances have been done by CERN on
1347 three main technical fields: accelerators, detectors and computing. Behind
1348 these three areas of technology, lies a great number of topics of expertise:
1349 cryogenics, ultra-high vacuums, particle tracking, radiation monitoring, su-
1350 perconductivity, plasma-physics and many more. Probably, the most pop-
1351 ular of the contributions is the invention of the World Wide Web (WWW)
1352 in 1989 at CERN facilities [110]. All of this proves the versatility and cap-
1353 ability of CERN as a contributor to science, technology and society.

1354 2.2 Large Hadron Collider

1355 In the mid of the decade of 1980, the plans for building the Large Hadron
1356 Collider (LHC) were started. At several high-energy physics workshops
1357 and conferences, the idea of assembling a machine able to reach multi-TeV
1358 energies was discussed. This instrument would allow physicists to search for
1359 the Higgs boson at all possible masses. In 1991 the Long-Range Planning
1360 Committee of CERN proposed the construction of the LHC as the best step
1361 forward in CERN's future [111]. The approval of the LHC project arrived
1362 in 1994 and in 1995 the Conceptual Design Report was published [112].
1363 Finally, on 10 September 2008, a beam of protons was successfully directed
1364 into the LHC pipes for the first time.

1365 A summary of the main parameters of LHC for pp collisions is pre-
1366 sented in Table 2.1. These parameters are shown for how the machine was
1367 designed, for Run-1 (2011-2012) and Run-2 (2015-2018) as well as the ex-
1368 pected parameters for Run-3 (2025-2027). The forecasted values for the
1369 High Luminosity (HL) LHC upgrade (after 2027) are exposed too.

1370 2.2.1 Machine design

1371 The LHC is a circular hadron accelerator with a circumference of 27 km.
1372 Located where once was the LEP collider, the accelerator used by CERN
1373 from 1999 to 2000 [113], the LHC tunnels are almost entirely outside the
1374 main site, being mainly on french territory. An overall schematic view of
1375 the LHC is shown in Figure 2.1.

1376 The LHC has two rings with ultra-high vacuum (to prevent collisions
1377 with gas molecules while moving through the accelerator) inside of which

Parameter	Design	Run-1	Run-2	Run-3	HL-LHC
Beam energy	7	3.5 - 4	6.5	7	7
Center-of-mass energy (\sqrt{s}) [TeV]	14	7 - 8	13	14	14
Bunch spacing [ns]	25	50	25	25	25
Bunch Intensity [10^{11} ppb]	1.15	1.6	1.2	up to 1.8	2.2
Number of bunches (n_b)	2800	1400	2500	2800	2800
Transverse emittance (ϵ) [μm]	3.5	2.2	2.2	2.5	2.5
Amplitude function at the interaction point (β^*) [cm]	55	80	30→25	30→25	down to 15
Crossing angle [μrad]	285	-	300→260	300→260	TBD
Peak Luminosity [$10^{34} \text{ cm}^2 \text{ s}^{-1}$]	1.0	0.8	2.0	2.0	5.0
Peak pileup	25	45	60	55	150
Nominal magnetic field (B) [T]	8.73	4.16 - 7.76	7.73	8.73	8.73
Injection energy [GeV]				450	
Circumference length [km]				26.7	
Radius [km]				4.24	
Number of dipole magnets				1232	
Length of dipole magnets [m]				14.3	
Number of quadrupole magnets				395	
Total mass [tons]				27.5	

Table 2.1: Summary of main accelerator parameters for the LHC, showing the design values, and those used during Run-1 and Run-2, as well as the expected parameters for Run-3 and the HL-LHC.

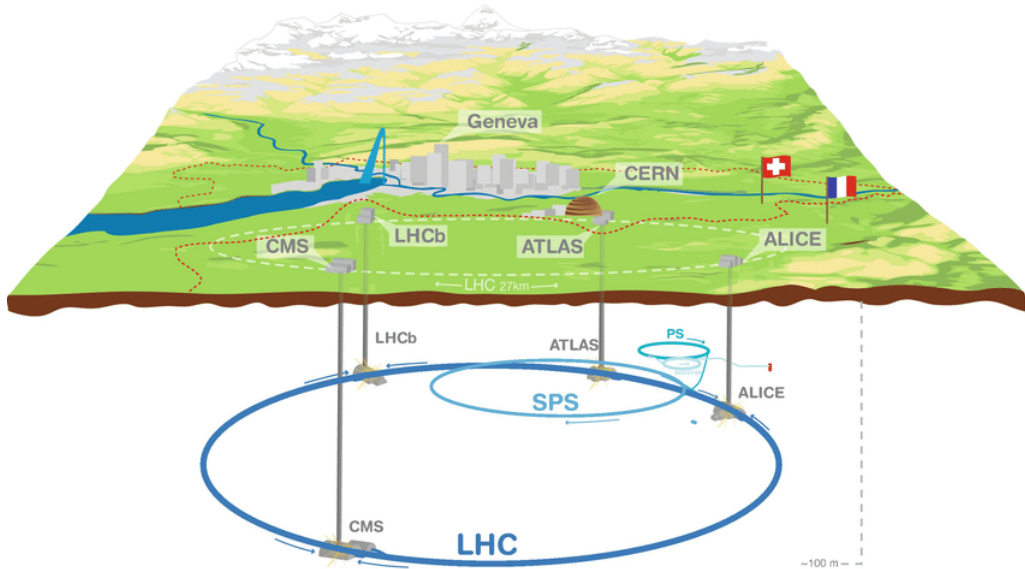


Figure 2.1: Overall view of the LHC including the ATLAS, CMS, ALICE and LHCb experiments.

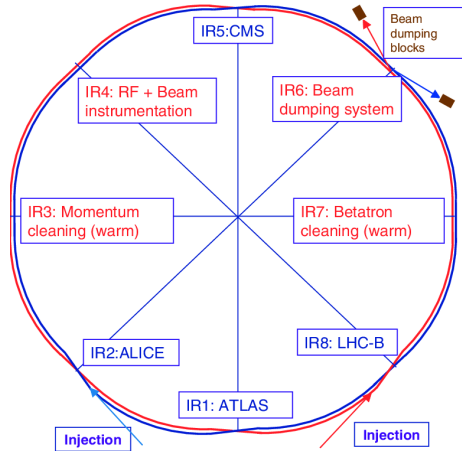


Figure 2.2: Schematic layout of the LHC (Beam 1 clockwise, Beam 2 anti-clockwise).

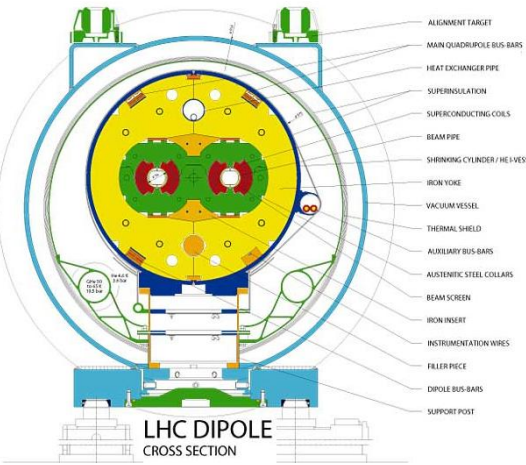


Figure 2.3: LHC dipole cross section.

1378 particle beams travelling in opposite directions. It was designed to accelerate and collide proton beams with a center-of-mass energy (\sqrt{s}) up to
 1379 14 TeV at a luminosity (\mathcal{L}) of $10^{34} \text{ cm}^2 \text{ s}^{-1}$ (see Section 2.2.5 for details
 1380 about luminosity). As well as protons, it can collide heavy ions, in partic-
 1381 ular lead nuclei, at $\sqrt{s} = 2.3 \text{ TeV}$ per nucleon and a peak luminosity of $\mathcal{L} = 10^{27} \text{ cm}^2 \text{ s}^{-1}$ [114]. These specifications make the LHC the accelerator
 1382 with higher collision energy [115].
 1383

1384 The beams in the LHC are made up of bunches of protons that are
 1385 spaced 7 m apart and collide every 25 ns. Each bunch contains 1.1×10^{11}
 1386 hadrons, being 2556 the maximum possible number of bunches that can be
 1387 reached with the beam preparation method currently used [116]. The size
 1388 of each bunch is 25 cm [117].
 1389

1390 The LEP tunnel lies between 45 m and 170 m below the surface on a
 1391 plane inclined at 1.4% sloping towards the Léman lake. The underground
 1392 construction adds some shielding from outside interferences that could in-
 1393 teract with the detectors and cause anomalous readings. Even 100 m under-
 1394 ground, the cosmic rays can reach the detectors, so these are used to help to
 1395 calibrate them. The tunnel has an internal diameter of 3.7 m, which makes
 1396 it extremely difficult to install two completely separate proton rings [118]
 1397 as in the Superconducting Super Collider (SSC). Therefore, the counter-
 1398 rotating rings are built under the *two-in-one* twin-bore superconducting
 1399 magnet design. These twin bore configurations have the disadvantage of
 1400 having the rings magnetically coupled, which adversely affects flexibility
 1401 [119]. Figure 2.3 shows an example of the LHC twin-bore dipole magnet.

1402 The LHC is not a perfect circle. Approximately 22 km of the LHC ring
1403 consists of 8 curved sections. The remaining 5 km of the tunnel are made of 8
1404 straight sections, denominated insertion regions (IR), that provide space for
1405 the experiments. Figure 2.2 shows the distribution of IR and crossing points
1406 for the LHC. This layout follows that of the LEP tunnel. The number of
1407 crossing points where the beams pass from one ring to the other for colliding
1408 was decreased from the original 8 at LEP to 4 in the LHC in order to reduce
1409 costs and optimise the utility insertions containing Radio Frequency (RF),
1410 the collimation and the beam dump systems [112].

1411 The arcs contain the dipole bending magnets, which are shown in Section
1412 2.3. The 1232 twin-bore magnets curve the trajectory of the particle beam
1413 that would, otherwise, follow a straight line. Dipoles are also equipped with
1414 additional multipole lattice magnets (sextupole, octupole and decapole),
1415 which correct for small imperfections in the magnetic field at the extremities
1416 of the dipoles.

1417 Each of the 8 straight sections is approximately 528 m long. The RF
1418 cavities delivering 2 MV (an accelerating field of 5 MV/m) at 400 MHz are
1419 located in the IR4. The 16 RF cavities compensate the synchrotron radi-
1420 ation losses (the electromagnetic radiation emitted when charged particles
1421 travel in curved paths) that take place at the arcs of LHC. The energy ra-
1422 diated per particle by synchrotron radiation is proportional to the inverse
1423 of the mass of the particle: $\Delta E \propto 1/m^4$. This radiation is, thus, smaller
1424 for protons than for electrons. That is why the LHC machine has much less
1425 synchrotron radiation losses than LEP and its design would ideally have
1426 longer arcs and shorter straight sections for the same circumference. But
1427 using the tunnel as built for LEP was the cost-effective solution. During
1428 the 20 minutes that are needed to reach the beams maximum energy, the
1429 bunches have passed the RF cavities more than 10 million times [112].

1430 The RF cavities (also known as resonators) are metallic chambers spaced
1431 at intervals along the accelerator shaped to resonate at specific frequencies,
1432 allowing radio waves to interact with passing particle bunches. The main
1433 role of the RF cavities is to keep the proton bunches tightly packed to
1434 ensure the required luminosity at the interaction point. They also transfer
1435 RF power to the beam to accelerate it to the top energy [120].

1436 At the insertion of the arc and straight sections, quadrupole magnets
1437 are installed to suppress the dispersion of particles. Acting as focal lenses,
1438 quadrupole magnets gather the particles together. This system not only
1439 cancels the horizontal dispersion arising in the arc but also adapts the LHC
1440 reference orbit to the geometry of the LEP tunnel. Before entering the
1441 detectors, the inner triplets (which are made mostly from quadrupoles)

1442 tighten the beam, from 0.2×10^{-3} m down to 16×10^{-6} m. These are known
1443 as insertion magnets.

1444 In total there are more than 9000 magnets all over the LHC and more
1445 than 50 types of magnets are needed to make the particles circulate in
1446 their path without losing speed. The coils are made of niobium-titanium
1447 (NbTi) which is cooled to less than 2 K with superfluid helium to reach
1448 superconductivity.

Of course, only stable charge particles¹ such as electrons, positrons, protons, antiprotons and some ions, can be accelerated by the magnetic fields described. The force that experiments a charged particle with charge q moving under a magnetic field B at a speed v is given by Lorentz law

$$\vec{F} = q \vec{v} \times \vec{B} \quad (2.1)$$

1449 and, since \vec{B} is perpendicular to \vec{v} , this force is always directed to the
1450 center of the circle of radius r : $F = Bqv = m\frac{v^2}{r}$.

1451 2.2.2 Accelerator complex

1452 To accelerate the proton beams, the existing CERN accelerator complex
1453 is used. These accelerators were, back in the day, the state of the art
1454 colliders and now they serve as injection system for the LHC. The path
1455 followed by the particle beams is presented in Figure 2.4. The accelerator
1456 complex consists in several machines interconnected with higher and higher
1457 capabilities, i.e. the beams are injected from one accelerator to the next in
1458 sequence, boosting the particles to higher energies in each step until they
1459 enter into the LHC.

1460 The proton bunches are produced ionising a gas of hydrogen atoms and
1461 then they are accelerated to a momentum of 50 MeV by the linear accelerator
1462 (LINAC2). Starting from Run-3, the LINAC2 is being replaced by the
1463 LINAC4. After being produced, the beams enter into the first circular
1464 accelerator, the Proton Synchrotron Booster (PSB) which has 630 m radius
1465 and increases the energy of the protons until 1.4 GeV.

1466 The main advantage of circular accelerators compared to linear ones is
1467 that they can speed up particles with much less physical space. Circular
1468 accelerators ramp up two different beams with opposite charges at the same
1469 time with a single magnetic field. The maximum energy transferred to the
1470 beams in a circular accelerator is given by p_T [GeV] = $0.3qB[T]r[m]$, being

¹Long-lived particles such as the muon ($\tau \approx 2 \times 10^{-6}$ s) are discussed to be used on a muon collider [121].

1471 p_T the transverse momentum of the particles, q the charge of the particles
1472 ($q = 1$ for protons), B the magnetic field applied and r the radius of the
1473 circular accelerator.

1474 Right after the PSB, the Proton Synchrotron brings the particles 25 GeV.
1475 The next step in the chain raises the energy to 450 GeV. This is done by the
1476 SPS, which is 6.9 km long. Once the protons have 450 GeV, the minimum
1477 energy at which the LHC can maintain a stable beam, they are injected
1478 into the LHC by two different 2 km-long Transfer Injection (TI) lines [122].
1479 Protons will circulate in the LHC for 20 minutes until reaching the maximum
1480 speed and energy (650 GeV per beam) [119].

1481 Heavy-ion collisions were included in the conceptual design of the LHC
1482 from an early stage. Lead ions for the LHC are extracted from a source
1483 of vaporised lead and enter LINAC3 before being collected and accelerated
1484 in the Low Energy Ion Ring (LEIR). They, then, follow the same route to
1485 maximum acceleration as the protons [119].

1486 2.2.3 LHC Experiments

1487 In the LHC four major experiments are carried, each of them with its own
1488 detector (Figure 2.5). These particle detectors measure particles produced
1489 as debris from the pp collisions through the interaction with the material
1490 of the sub-detectors. Distributed along the collider as is shown in Figures
1491 2.1, 2.2 and 2.4, these highly sophisticated experiments are:

- 1492 • **A Toroidal LHC ApparatuS (ATLAS)** [123]: Located in the IR1,
1493 it is a generic multi-purpose experiment for high luminosity (up to \mathcal{L}
1494 = $10^{34} \text{ cm}^2 \text{ s}^{-1}$). It studies proton-proton collisions and investigates
1495 a wide range of physics, from the search for extra dimensions to dark
1496 matter. It has the dimensions of a cylinder, 46 m long, 25 m in dia-
1497 meter. The ATLAS detector weighs 7×10^3 tonnes. The design of the
1498 ALTAS detector features excellent jet and E_T^{miss} resolution, particle
1499 identification and flavour tagging and standalone muon measurements.
1500 ATLAS will be covered in detail in Section 2.3.
- 1501 • **Compact Muon Solenoid (CMS)** [124]: Built inside the IR5, it's
1502 the other general-purpose experiment for high luminosity (same \mathcal{L} as
1503 ATLAS). CMS has the same objectives and goals as ATLAS but both
1504 its hardware and software designs are different. Even though CMS is
1505 smaller than ATLAS (21 m long, 15 m in diameter) it is much heavier,
1506 weighting 14×10^3 tonnes. The bulk of its weight is the steel yoke that
1507 confines the 4 T magnetic field of its superconducting solenoid. The

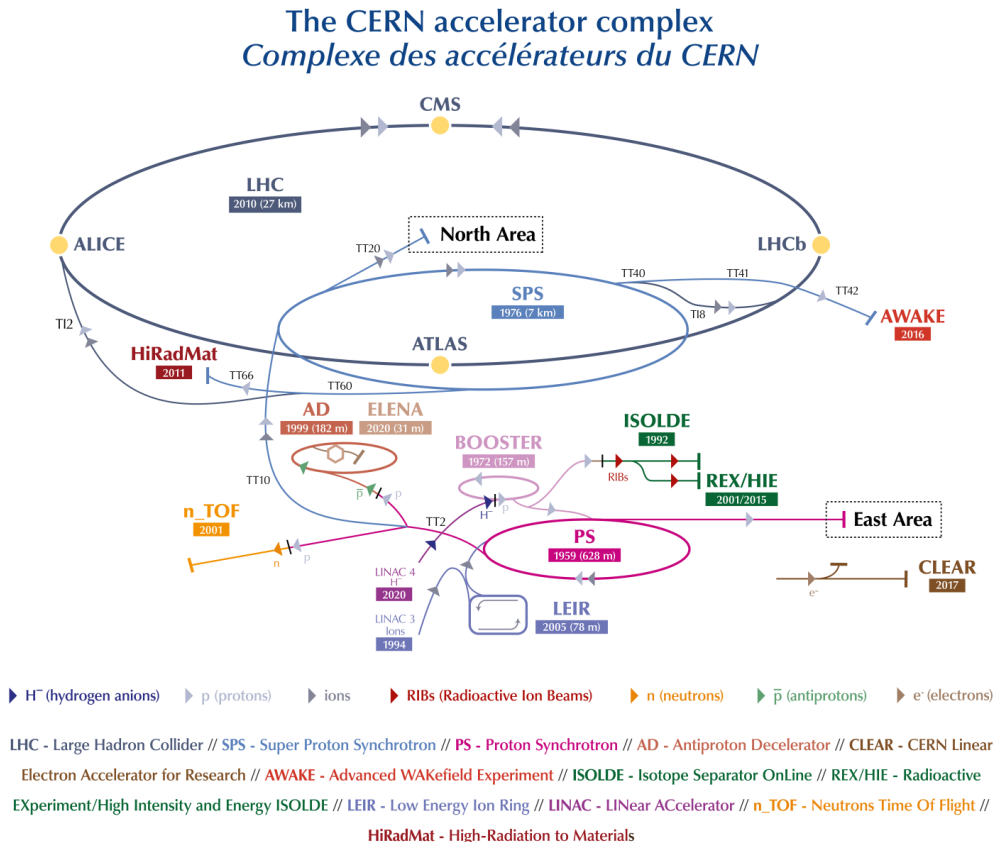


Figure 2.4: Scheme of CERN accelerator complex. Protons are injected from the LINAC2 into the PS Booster, then the PS, followed by the SPS, before finally reaching the LHC.

design of CMS emphasises magnificent electron/photon energy and momentum resolution. The role of coexistence of CMS and ATLAS is fundamental so that one can verify and confirm the experiments of the other independently.

- **Large Hadron Collider beauty (LHCb)** [125]: Hosted at IR2, it is a lower luminosity experiment designed to study the small asymmetries between matter and antimatter through \mathcal{CP} violation using rare decays of b -quark based hadrons. The detector is arranged as a succession of planar sub-detectors since most of the b -flavoured mesons follow the beam pipe direction when created in the proton-proton collision. LHCb delivers remarkable low-momentum track reconstruction and particle identification.
- **A Large Ion Collider Experiment (ALICE)** [126]: It is a low luminosity experiment in IR8 that focuses on QCD, the strong-

1522 interaction sector of the SM. The main feature of ALICE is a general-
 1523 purpose detector that it uses heavy-ion collisions to study matter in-
 1524 teracting at extreme densities and temperatures, thus reproducing the
 1525 quark-gluon plasma. This detector provides highly efficient track re-
 1526 construction in an environment full of heavy ions. Besides running
 1527 with Pb ions, the physics programme includes collisions with lighter
 1528 ions, lower energy collisions and a dedicated proton-nucleus run.

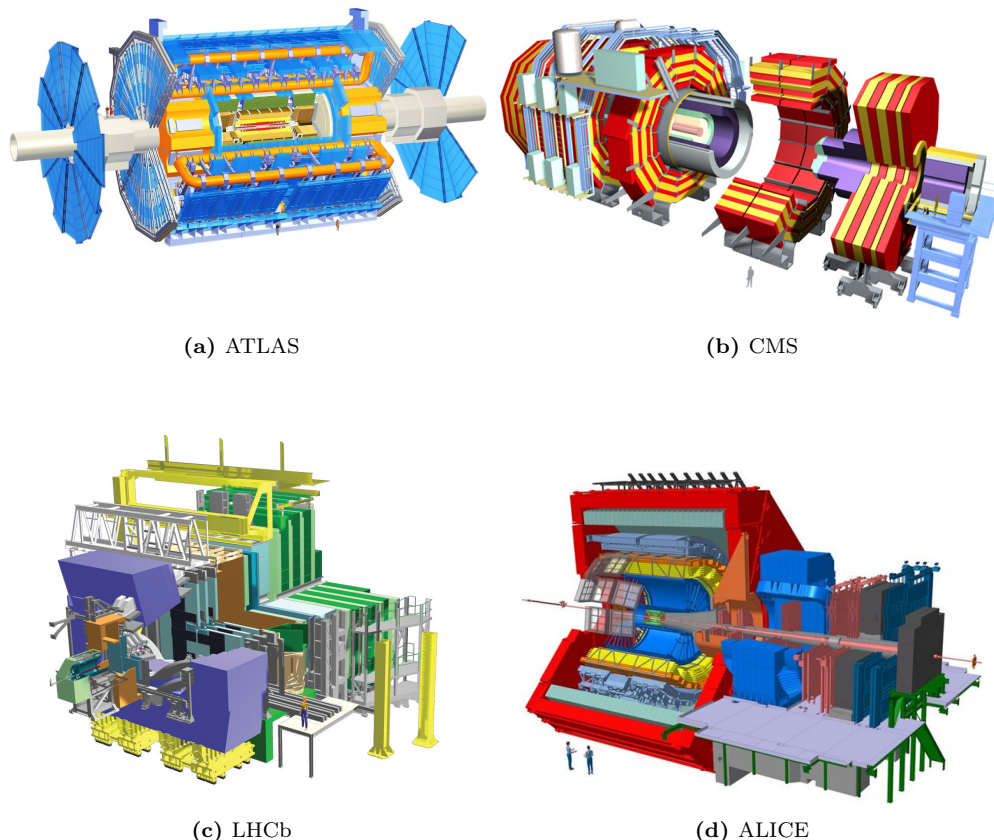


Figure 2.5: Scheme of LHC main experiments. Note that the images are not equally scaled.

1529 Along the LHC machine, there are other experiments much more smaller
 1530 than ATLAS, CMS, LHCb and ALICE, typically sharing the cavern with
 1531 the major projects. The most relevant among the minor experiments are:

- 1532 • **The Large Hadron Collider forward (LHCf)** [127]: Uses
 1533 particles thrown forward by collisions in the Large Hadron Collider
 1534 as a source to simulate cosmic rays in laboratory conditions. It shares
 1535 its cavern with the ATLAS detector [128].

- 1536 • **The Massive Timing Hodoscope for Ultra Stable neutrAL**
1537 **pArticles (MATHUSLA)** [129]: Is dedicated large-volume dis-
1538 placed vertex detector for the HL-LHC on the surface above ATLAS
1539 or CMS for the search for neutral long-lived particles.

- 1540 • **MilliQan** [130][131]: Consists on a small-scale detector experiment
1541 aiming to detect millicharged particles, i.e., particles with charges
1542 much smaller than that of the electron.

- 1543 • **Monopole and exotic particle detector at the LHC**
1544 (**MoEDAL**) [132]: Deployed at LHCb cavern, it is optimised to de-
1545 tect highly ionising particles such as magnetic monopoles, dyons and
1546 multiple-electrically charged stable massive particles predicted in a
1547 number of theoretical scenarios.

- 1548 • **TOTEM** [133]: Aims to measure the total cross-section of pp inter-
1549 action using a luminosity-independent method and study elastic and
1550 diffractive scattering at the LHC. As CERN longest experiment, TO-
1551 TEM detectors are spread across almost half a kilometre around the
1552 CMS interaction point.

- 1553 • **ForwArd Search ExpeRiment (FASER)** [134][135]: Designed to
1554 search for new, yet undiscovered, light and weakly-interacting particles
1555 and study the interactions of high-energy neutrinos.

1556 2.2.4 LHC Computing grid

1557 The data collected by the different LHC experiments is stored, processed
1558 and, then, made available for all the researchers of each collaboration². This
1559 is possible thanks to the last piece of the LHC, its computing model and
1560 infrastructure: the LHC Computing Grid (LCG). It consists of several com-
1561 puting farms distributed around the world and interconnected. Figure 2.6
1562 shows the geographical distribution of the different facilities that comprise
1563 the LCG. Just as the WWW enables access to information, the Grid en-
1564 ables access to computer resources. Employing a grid certificate, is possible
1565 for any user to run jobs on the grid and to access the data stored. The
1566 implementation of the grid model implies an effective coordination among
1567 all LHC collaboration centres [136].

1568 Different types of computing centres have been defined and classified in
1569 Tiers [138]:

²Within the grid context, each collaboration is known as Virtual Organisation (VO).



Figure 2.6: Worldwide LHC Computing Grid geolocalisation of sites [137].

- 1570 • **Tier-0:** This facility is located at CERN and it is responsible for
 1571 archiving (first copy) and distributing the raw data received from the
 1572 Event Filter, i.e., the data emerging from the Data Acquisition systems (DAQ)
 1573 after the trigger. It provides prompt reconstruction and
 1574 distributes a copy of the raw data to the Tier-1 centres.
- 1575 • **Tier-1:** These facilities archive the raw data permanently and provide
 1576 the computational capacity for reprocessing and for physical analysis.
 1577 It also stores the simulated and reprocessed data. Currently, there
 1578 are thirteen large computer centres serving as Tier-1 (see Figure 2.7).
 1579 These make data available to their Tier-2 centres [139].
- 1580 • **Tier-2:** Typically located at universities and other scientific insti-
 1581 tutes, there are more than 150 Tier-2 sites. The derived datasets
 1582 produced by the physics groups are copied to the Tier-2 facilities for
 1583 further analysis. The MC simulations for event production are ex-
 1584 ecuted at this level.
- 1585 • **Tier-3:** The local computing resources, from local clusters to even
 1586 just an individual PC are referred to as Tier-3. There is no formal
 1587 engagement between worldwide LCG and the Tier-3.

1588 This system provides near real-time access to LHC data. The LCG
 1589 collaboration spreads out over 42 countries with 170 computing centres and
 1590 1 million computer cores, being the world's largest computer grid. It deals
 1591 with over two million tasks daily. These specifications make the LCG the
 1592 most sophisticated system for data taking and analysis ever built for science.

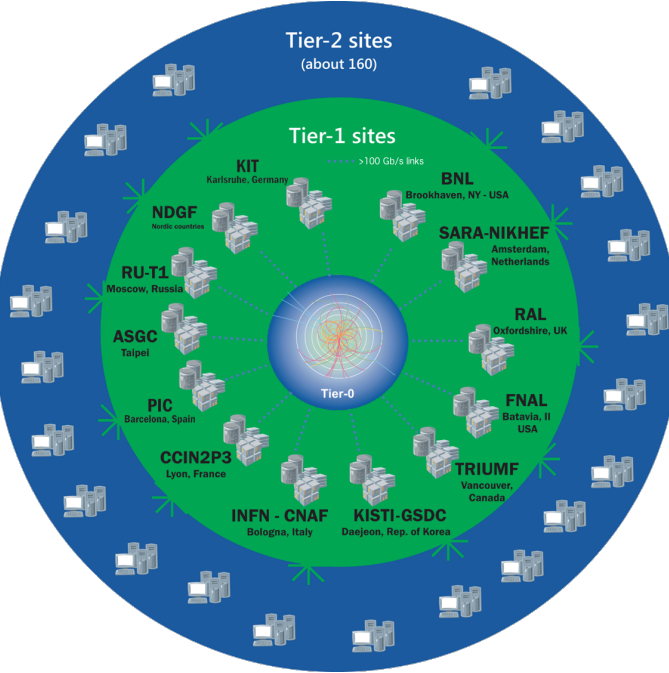


Figure 2.7: LCG Tiers [139].

1593 2.2.5 Energy, Luminosity and Cross-section

1594 Energy

1595 Another name to refer to the field of Particle Physics is “high energy phys-
 1596 ics”. Particles such as the Higgs boson or the top quark are more than 100
 1597 times heavier than the proton so, in order to produce them, huge energies
 1598 are required. The energy of the interaction, \sqrt{s} , allows the production of
 1599 physical effects. The greater the energy is, the bigger is the range of the
 1600 different processes that can be produced by the accelerator.

The four-vector, $\mathbf{p} = (E, \vec{p})$, of a particle of mass m describes its kinematics with its energy E and \vec{p} . The square of the four-vector, \mathbf{p}^2 , corresponds to the particle mass:

$$\mathbf{p}^2 = E^2 - \vec{p}^2 = m^2 \quad (2.2)$$

When two particles of mass m_1 and m_2 and momenta \vec{p}_1 and \vec{p}_2 respectively collide, the center of mass energy, \sqrt{s} , can be expressed as:

$$s = E_{CM}^2 = (\mathbf{p}_1 + \mathbf{p}_2)^2 = (E_1 + E_2)^2 - (\vec{p}_1 + \vec{p}_2)^2 \quad (2.3)$$

For symmetric colliding beams, such those of LHC, the collision point is at rest in the laboratory frame ($\vec{p}_1 = -\vec{p}_2$) and, hence, the energy is

$$s = E_{CM}^2 = (E_1 + E_2)^2 \quad (2.4)$$

1601 Since the energy of each beam is 650 GeV during Run-2, the center of mass
 1602 energy of LHC collisions is

$$\sqrt{s} = E_{CM} = (E_{beam1} + E_{beam2}) = 650 \text{ GeV} + 650 \text{ GeV} = 13 \text{ TeV} \quad (2.5)$$

When LHC is used for fix target experiments, one of the particles in the collision is at rest ($\vec{p}_2 = 0$) and the equation 2.3 writes as:

$$E_{CM}^2 = (m_1^2 + m_2^2 + 2m_2 E_{1,lab}) \quad (2.6)$$

Then, the energy for a proton-proton fix target collision with one beam at 650 GeV is

$$\begin{aligned} E_{CM}^2 &= (m_p^2 + m_p^2 + 2m_p E_{beam}) \\ &= 2(0.938 \text{ GeV})^2 + 2 \cdot 0.938 \text{ GeV} \cdot 650 \text{ GeV} = 1221.2 \text{ GeV}^2 \\ E_{CM} &= 34.9 \text{ GeV} \end{aligned} \quad (2.7)$$

1603 This shows why colliding beams are essential to achieve high center of mass
 1604 energies.

1605 **Luminosity**

1606 Besides \sqrt{s} , the luminosity is the most relevant parameter in an experiment,
 1607 especially in searches for events with small cross-section. It measures the
 1608 ability of the particle accelerator to produce enough events of the desired
 1609 type.

The luminosity, \mathcal{L} , is the ratio of events detected in a certain period of time for a given cross-section (σ):

$$\mathcal{L} = \frac{1}{\sigma} \frac{dN}{dt} = \frac{1}{\sigma} R \quad (2.8)$$

1610 where N is the number of the events and t the time. $R = \frac{dN}{dt}$ is known as
 1611 reaction rate. It can be understood as number of particle collision per unit
 1612 area (typically expressed in cm^2) and per second, therefore it is measured in
 1613 $\text{cm}^2 \text{s}^{-1}$ [140]. For instance, for LEP was $\mathcal{L}_{LEP} = 1.0 \times 10^{32} \text{ cm}^2 \text{s}^{-1}$ and
 1614 the LHC is designed to achieve $\mathcal{L}_{LHC_{pp}} = 2.1 \times 10^{34} \text{ cm}^2 \text{s}^{-1}$ in pp collisions
 1615 and $\mathcal{L}_{LHC_{PbPb}} = 6.1 \times 10^{27} \text{ cm}^2 \text{s}^{-1}$ for heavy ion collisions.

For two beams colliding, the instantaneous luminosity is proportional to the number of bunches per beam (n_1 and n_2), the revolution frequency (f) with which the bunches are crossing and the number of proton bunches in

the machine (n_b), and it is and inversely proportional to the beams effective transverse area in which the collision takes places (Area = $4\pi\sigma_x\sigma_y$)

$$\mathcal{L} = f \cdot \frac{n_1 n_2 n_b}{4\pi\sigma_x\sigma_y} \cdot F(\theta_c, \sigma_x, \sigma_z) \quad (2.9)$$

where $F(\theta_c, \sigma_x, \sigma_z)$ is a factor accounting for the luminosity reduction due to the beam crossing angle (θ_c). At the LHC, assuming that the particles travel at the speed of light, for its 27 km, the bunch crossing frequency is $f = 11245.5$ Hz. The maximum number of proton bunches in the machine with 25 ns slots is³ $n_b = 2808$. In each bunch there are $n_1 \approx n_2 \approx 1.15 \times 10^{11}$ particles. Finally, characterising the optics of the collision at the interaction point (IP), the RMS transverse beam width in the horizontal and vertical directions are $\sigma_x \approx \sigma_y \approx 12, \dots, 50 \mu m$. The expression 2.9 assumes that the particles in the beam are Gaussian distributed. According to equation 2.9 the instantaneous luminosity only depends on the machine and its beam parameters [141][142].

The integrated luminosity over time is given by

$$L = \int \mathcal{L} dt \quad (2.10)$$

and it is used to determine the number of events, N , that have taken place during that time: $N = \sigma \times L$. The ability to observe low cross-section events is

$$N_{events}^{obs} = \sigma_{process} \times \text{efficiency} \times L \quad (2.11)$$

, where the efficiency of the detection is to be optimised by the experimental physicist, the integrated luminosity (L) is delivered by LHC and the cross-section of the process ($\sigma_{process}$) is given by nature.

On one hand, several factors can limit the maximum luminosity that can be achieved at LHC [140]:

- **Beam-beam effect:** The bunches of two beams or the particles in the same bunch can interact electromagnetically, this leads to distortions from the orbit and results in an increase of the emittance, ϵ .
- **Crossing angle:** Often used to avoid unwanted collisions in machines with many bunches, due to the crossing angle θ_c , the luminosity is reduced by a factor $F(\theta_c, \sigma_x, \sigma_z) = \sqrt{1 + (\theta_c \sigma_z / 2\sigma x)^2}$.
- **Beam offset:** Originated from the beam-beam effects or misalignments in the quadrupole magnets, the beams can collide with small

³The theoretical maximum of 3564 bunches cannot be reached due to space needed between bunch trains and for the beam dump kicker magnets.

Year	2015	2016	2017	2018
Peak instantaneous luminosity ($\times 10^{33} \text{ cm}^2 \text{ s}^{-1}$)	5	13	16	19
Total delivered integrated luminosity (fb^{-1})	4.0	38.5	50.2	63.4

Table 2.2: Peak luminosity and total integrated luminosity delivered by the LHC at $\sqrt{s} = 13 \text{ TeV}$ in Run-2 per year [144].

1640 transverse offset. Such beams' offsets induce a loss of \mathcal{L} at the inter-
 1641 action point.

- 1642 • **Hourglass effect:** Appears when beams collide in a point away from
 1643 the IP.

1644 On the other hand, there are diverse strategies to maximise the lumin-
 1645 osity delivered by a machine [141]:

- 1646 • **Maximise the total beam current:** Improvements in beam col-
 1647 limitation, cryogenics vacuum and background protection could extend
 1648 the limit on the maximum beam current.
- 1649 • **Compensate reduction factor:** The hourglass effect may be re-
 1650 duced by shorter bunches at the expense of a higher longitudinal pileup
 1651 density (see Section 2.2.6).

1652 The cumulative luminosity delivered by LHC to ATLAS during the Run-
 1653 2 per year is shown in Figure 2.8. In Figure 2.9, the total Run-2 cumulative
 1654 luminosity is presented differentiating between the delivered and recorded
 1655 luminosity and showing that almost all delivered events are considered to
 1656 be good data quality. The delivered luminosity accounts for the luminosity
 1657 given from the start of stable beams until the LHC requests ATLAS to
 1658 put the detector in a safe standby mode to allow a beam dump or beam
 1659 studies. The recorded luminosity reflects the DAQ inefficiency, as well as
 1660 the inefficiency of the so-called “warm start”: when the stable beam flag is
 1661 raised, the tracking detectors undergo a ramp of the high-voltage and, for
 1662 the pixel system, turning on the preamplifiers. The All Good Data Quality
 1663 criteria require all reconstructed physics objects to be of good data quality
 1664 [143].

1665 Cross-section

1666 The cross-section is a metric of the likely is a particular reaction to occur.
 1667 The higher the cross section is for a process, the more probable is for it to
 1668 take place. Denoted by σ , it is measured in units of area named barns: 1
 1669 barn = $b = 10^{-24} \text{ cm}^2$. For instance, for the LHC energy:

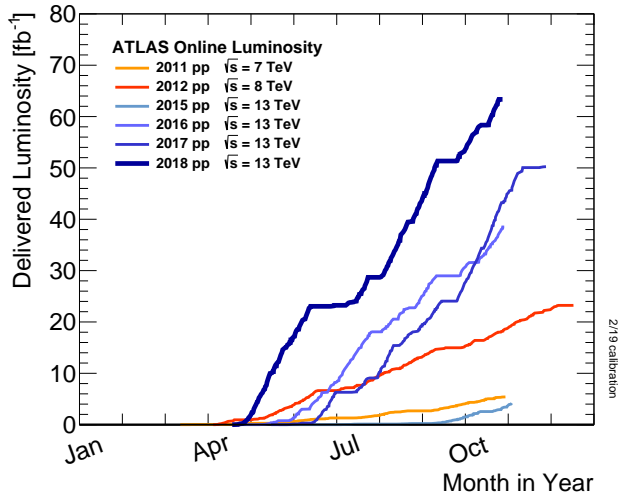


Figure 2.8: Cumulative luminosity versus day delivered to ATLAS during stable beams and for high energy pp collisions.

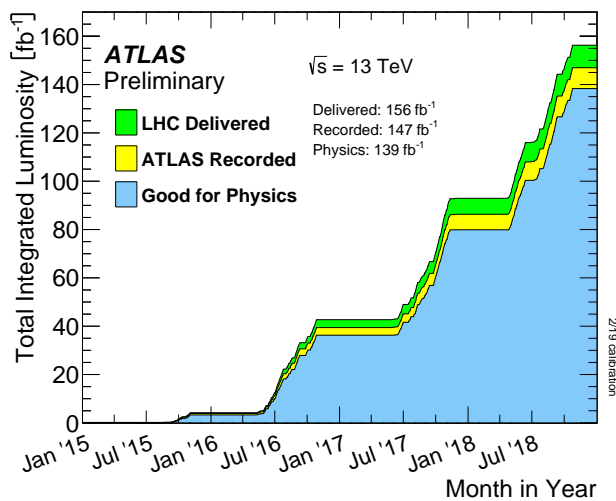


Figure 2.9: Total cumulative luminosity versus time delivered to ATLAS (green), recorded by ATLAS (yellow) and certified to be good quality data (blue) during stable beams for pp collisions at $\sqrt{s} = 13 \text{ TeV}$.

- 1670 • $\sigma(pp \rightarrow X) \approx 0.1 \text{ b}$
- 1671 • $\sigma(pp \rightarrow X + H) \approx 1 \times 10^{-11} \text{ b}$
- 1672 • $\sigma(pp \rightarrow X + H; H \rightarrow \gamma\gamma) \approx 50 \times 10^{-15} \text{ b}$

1673 In experiments with rotational symmetry, such as ATLAS, it is usual to
1674 define the differential cross-section ($\frac{d\sigma}{d\Omega}$) as the cross-section per solid angle.
1675 If the differential cross-section is integrated over corresponding the angular
1676 range, the cross-section for a specific region (σ_ϑ) is obtained:

$$1677 \quad \sigma_\vartheta = \int_0^\vartheta \int_0^{2\pi} \frac{d\sigma}{d\Omega} \sin(\vartheta) d\phi d\vartheta$$

with $\vartheta \in [0, \pi]$ is the coverage of the scattering angle.

The total cross-section is determined by the matrix element \mathcal{M} , which is independent of the experimental setup. The \mathcal{M} , also known as scattering amplitude, relates the initial state and the final state of a physical system undergoing a scattering process. Using \mathcal{M} , the total cross-section for a process is determined by:

$$\sigma_{tot} = \int \frac{d\sigma}{d\Omega} d\Omega = \int \frac{1}{\Phi} |\mathcal{M}|^2 dQ$$

1678 being Φ the incident particle flux in the process and the parameter dQ
1679 describes the kinematic phase space.

1680 2.2.6 The Pile-up effect

1681 Pile-up is a challenging matter among detectors and for the acquisition
1682 and analysis of the data. In particle physics, pile-up is called to the situation
1683 where the detector is being affected by several events at the same time.

1684 Even though the bunches are composed by $\sim 10^{11}$ protons, there are
1685 only around 30 collisions per crossing with nominal beam currents. The
1686 mean number of interactions per bunch crossing is presented in Figure 2.10
1687 for each year of Run-2. The data shown in Figure 2.10 is recorded by AT-
1688 LAS during stable beams at $\sqrt{s} = 13 \text{ TeV}$. The mean number of interactions

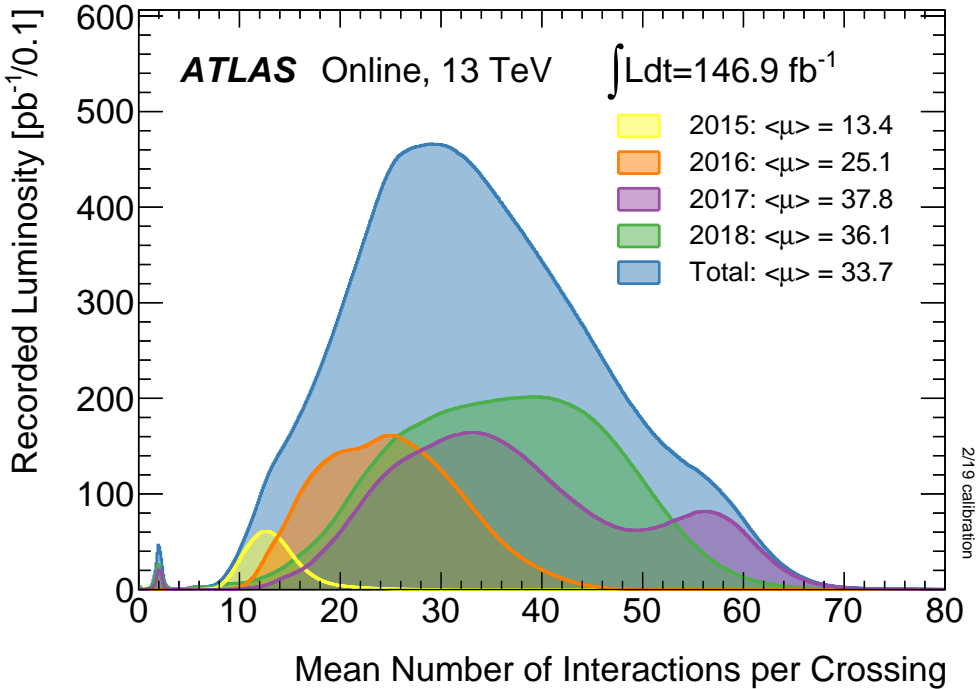


Figure 2.10: Luminosity-weighted distribution of the mean number of interactions per crossing $\langle \mu \rangle$ for Run-2 with pp collisions data.

per crossing corresponds to the mean of the poisson distribution of the number of interactions per crossing calculated for each bunch. It is calculated from the instantaneous per bunch luminosity as $\langle \mu \rangle = \mathcal{L}_{\text{bunch}} \times \sigma_{\text{inel}} / f_r$ where $\mathcal{L}_{\text{bunch}}$ is the instantaneous luminosity per bunch, $\sigma_{\text{inel}} = 80 \text{ mb}$ is the inelastic cross section of pp collisions at 13 TeV and $f_r = 11.245 \text{ kHz}$ is the LHC revolution frequency.

1695 Work in progress

1696 2.2.7 Phenomenology of proton-proton collisions

1697 During LHC Run-2 data taking period, the protons were colliding at a
 1698 center-of-mass energy of $\sqrt{s} = 13 \text{ TeV}$. The pp total cross-section at this
 1699 energy is measured to be $\sigma_{\text{tot}} = (110.6 \pm 3.4) \text{ mb}$ [145]. The luminosity-
 1700 independent method used to measure σ_{tot} allows to split the cross-section
 1701 into elastic and inelastic cross-sections, $\sigma_{\text{el}} = (31.9 \pm 1.7) \text{ mb}$ and $\sigma_{\text{inel}} =$
 1702 $(79.5 \pm 1.8) \text{ mb}$ respectively. However, only inelastic scattering generates
 1703 particles with an sufficient angle with respect to the beam axis so that
 1704 these particles enter into the geometrical acceptance of the detector. Figure
 1705 2.11 shows the cross-section (elastic, inelastic and total) for pp collisions

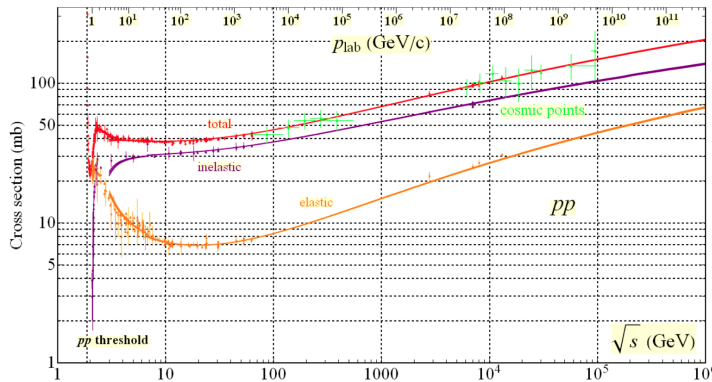


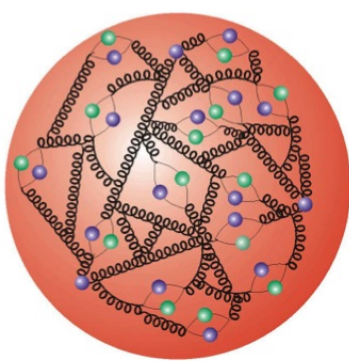
Figure 2.11: Total and elastic cross-section for pp collisions as a function of the laboratory momentum and the \sqrt{s} [146].

1706 depending on \sqrt{s} ([Why the values of the Figure 2.11 do not match the: \$\sigma_{tot} = \(110.6 \pm 3.4\)\$, \$\sigma_{el} = \(31.9 \pm 1.7\)\$ and \$\sigma_{inel} = \(79.5 \pm 1.8\$ \)](#)).
 1707 The shown cross-section can be computed as the convolution of parton
 1708 density functions (PDF) with the parton scattering matrix element \mathcal{M} .
 1709

1710 Unlike leptons, protons are composite objects since they are made of
 1711 quarks and gluons. Therefore and specially at LHC energy regime, the pp
 1712 collisions cannot be described as a point-like interactions, here is where the
 1713 PDFs come into play. The PDFs are functions containing the long distance
 1714 structure of the hadron in terms of valence and sea quarks and gluons.
 1715 This description is known as “parton model”.

1716 2.2.7.1 Proton structure and parton model for collisions

1717



The parton model for hadrons describes these non-fundamental particles as a composite of a number of point-like constituents named partons. The proton is not only simply made of three quarks (uud , the so called “valence” quarks) but also, there is a “sea” of gluons and short-lived quark and anti-quark pairs. The partons in the sea are continuously interacting with each other and can have any flavour.

1718 The PDFs describe the distribution of the hadron’s momentum among
 1719 its constituents. The PDFs are essential to describe the pp interactions be-
 1720 cause these collisions cannot be understood as point-like particles crashing.
 1721 Instead, all the constituents of the protons are taken into account [69].

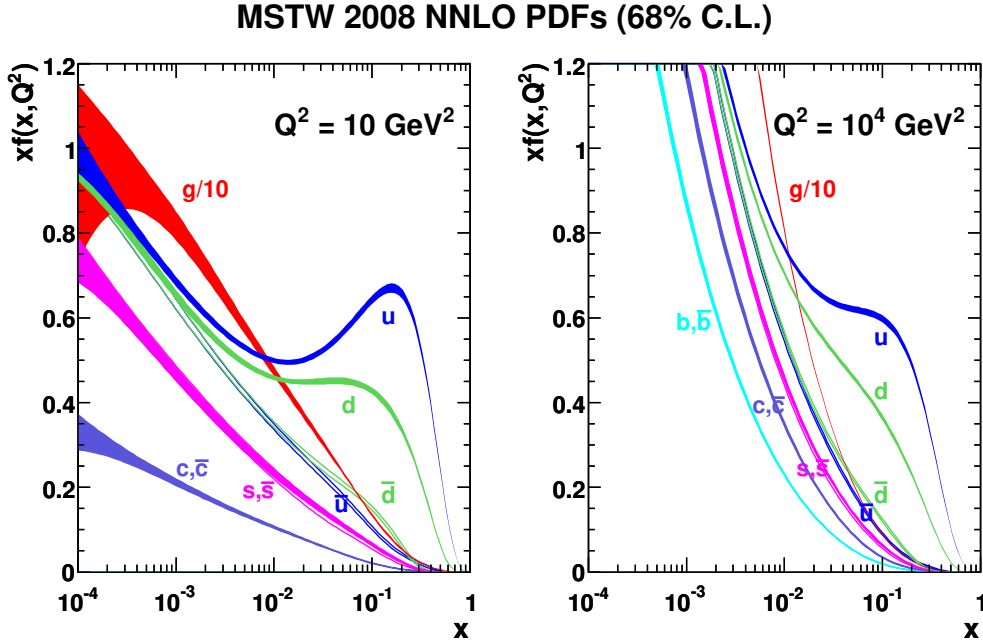


Figure 2.12: Parton distribution functions $xf(x, q^2)$ plotted against x for gluons different quark flavours at $Q^2 = 10 \text{ GeV}^2$ and $Q^2 = 10^4 \text{ GeV}^2$ using MSTW 2008 NNLO [70].

1722 Due to the fact that inside of hadrons the quarks are continuously interacting
 1723 with each other via the exchange of gluons, it is not possible to calculate PDFs using non-perturbative QCD. Instead, the momentum distribution function of the partons within the proton is obtained by a fit on
 1724 a large number of cross-section data points over a grid of x and Q^2 values obtained from many experiments (deep inelastic scattering, Drell-Yan and jet measurements). There are various global fitting collaborations (ABM,
 1725 CT, MMHT, NNPDF, MSTW, CTEQ), each taking different approaches
 1726 to this fitting procedure. These fits are later extrapolated to new energy
 1727 scales.

1732 Formally, the PDF $f_{a/A}(x, Q^2)$ is defined as the probability of finding
 1733 a parton a within the hadron A carrying a fraction $x = p_a/p_A$ of its momentum at Q^2 energy scale. The energy scale Q characterises the hard
 1734 scattering and typically corresponds to the momentum transfer in the given process. As an example, several PDFs at two different scale energies are
 1735 presented in Figure 2.12 as a function of x .

1738 The momentum of the proton is distributed among its constituents and,
 1739 while at lower energies ($Q \sim 1 \text{ GeV}$) it is shared mainly between the valence
 1740 quarks, at higher energies ($1 < Q \lesssim 1 \text{ GeV}$) the emission of gluons carrying
 1741 a some of the initial momentum of the quark is more probable. Within the

1742 QCD theory, these interactions can be classified in two main groups: “hard”
 1743 and “soft”. The hard processes are those involving large momentum trans-
 1744 fer. This type of processes are well understood and their cross-section can
 1745 be predicted with good precision using perturbation theory. In contrast,
 1746 the low momentum transfer of soft interactions leads to a much more dom-
 1747 inant impact of non-perturbative QCD, which makes much more difficult to
 1748 calculate the cross-section.

1749 When two protons (A and B) collide, what actually happens is that the
 1750 partons of one proton can interact with partons of the other via a hard
 1751 scattering process. Each of the interactions between the partons pairs (let a
 1752 be a parton from A interacting with b , a parton from B) is independent from
 1753 the interactions of other partons. The remaining partons also contribute to
 1754 the final state as “underlaying events”.

In a pp or, more generally, in a hadron-hadron (A and B) hard scattering process, the total cross section is given by:

$$\sigma_{AB \rightarrow X} = \sum_{a,b} \iint dx_a dx_b f_a(x_a, Q^2) f_b(x_b, Q^2) \times \hat{\sigma}_{ab \rightarrow X} \quad (2.12)$$

1755 where a and b denote the parton constituents of the hadrons A and B
 1756 respectively and $f_i(x_i, Q^2)$ their PDF. Here, the Q is chosen to be the fac-
 1757 torisation scale (μ_F). The contributions of the individual partons a and b is
 1758 denoted by $\hat{\sigma}_{ab \rightarrow X}$. With this equation, all process in pp collisions can can
 1759 be computed.

Depending on the order achieved in perturbation theory (LO, NLO, NNLO, ...), the cross-section of the individual partons to give the final state of instest ($ab \rightarrow X$) is calculated as

$$\begin{aligned} \hat{\sigma}_{ab \rightarrow X} &= \sum_{i=0}^{\infty} \alpha_s^i(\mu_R) \sigma_n(x_a, x_b, \mu_F^2) \\ &= [\sigma_{LO}(x_a, x_b, \mu_F^2) + \alpha_s(\mu_R) \sigma_{NLO}(x_a, x_b, \mu_F^2) \\ &\quad + \alpha_s(\mu_R)^2 \sigma_{NNLO}(x_a, x_b, \mu_F^2) + \dots]_{ab \rightarrow X} \end{aligned}$$

1760 where $\alpha_s^i(\mu_R)$ is the coupling constant derived for a specific renormalization
 1761 scale (μ_R).

1762 **Work in progress**

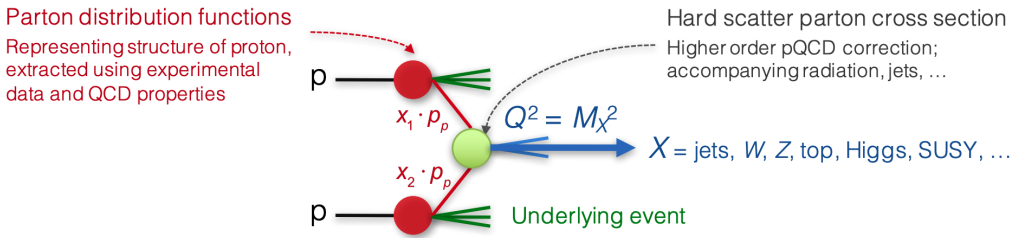


Figure 2.13: Simplified view of a pp collision [141].

1763 **2.2.7.2 Underlaying event**

1764 **2.3 ATLAS**

1765 Installed in its experimental cavern at point 1, ATLAS is the largest de-
1766 tector ever constructed for a particle collider with its 46 m long and 25 m in
1767 diameter. It is designed to record events of high-energy colliding particles
1768 at high luminosities. The thousands of millions of interactions that take
1769 place at the centre of the ATLAS detector are recorded and processed by
1770 the different sub-detectors, which are composed by more than 100 million
1771 sensitive electronic channels. Each ATLAS sub-detector is sensible to a dif-
1772 ferent type of particle and to different properties. Therefore, the layered
1773 structure allows for effective particle identification, as well as enables accu-
1774 rate measurements of energy and momentum. Figure 2.14 shows an overall
1775 layout of the ATLAS detector and identifies its different sub-detectors. In
1776 the picture can be appreciated that the cylindrical shape of ATLAS is di-
1777 vided into two parts: the “barrel” (curved parts) and the two “end-caps”
1778 (bases). In the barrel region, the sub-detectors are built as coaxial layers
1779 around the beam pipe (see memo 2.15). As one moves away from the axis,
1780 it finds the Inner Detector (ID), the solenoid magnet, the Electromagnetic
1781 (ECAL) and Hadronic (HCAL) Calorimeters, and the Muon Spectrometer
1782 (MS) in the outermost layer. The technical details of these sub-detectors
1783 are presented in the coming sections.

1784 ATLAS is able to explore a wide range of phenomena with high pre-
1785 cision, including new physics events. Even though it is a general-purpose
1786 experiment, it was designed taking into account the Higgs searches that
1787 were carried out at LHC. This is why, since the mass of the Higgs was not
1788 known at that time, its performance requirements cover a large mass range
1789 for the Higgs decay products.

1790 The stone for the foundations of ATLAS was laid in March 1992 at
1791 the critical ‘Towards the LHC Experimental Programme’ meeting, where
1792 physicists proposed several possible experiments for the LHC [148]. Two

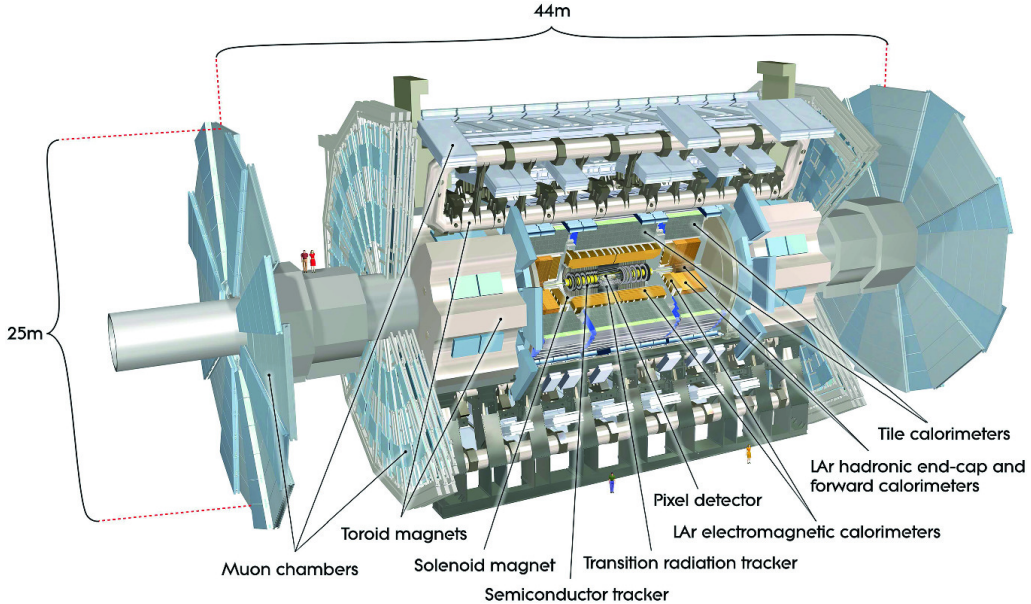


Figure 2.14: Simulated schematic view of the ATLAS detector.

1793 projects based on large toroidal magnet systems were proposed EAGLE
 1794 and ASCOT. By the summer of that year, both experiments merged into
 1795 ATLAS. In October 1992, the letter of intent of the ATLAS Collaboration
 1796 was sent to the LHC Experiments committee and, in 1994, the technical
 1797 proposal [149]. In 1997 the formal approval of the ATLAS experiment
 1798 arrived and one year later the excavation on the cavern began. The cavern
 1799 was inaugurated five years later and the construction of the ATLAS detector
 1800 ended in 2008. Later, in 2009, at $\sqrt{s} = 2.36 \text{ TeV}$, ATLAS records its first
 1801 collisions [150].

1802 One of the most important milestones for ATLAS (and for all science in
 1803 the last decades) was the observation of a particle consistent with the Higgs
 1804 boson in July 2012 (see 1.3.1). In 2016, the combination of ATLAS and
 1805 CMS measurements for Higgs boson production on decay rates with Run-
 1806 1 data was published [151]. After that, the physics programme at 13 TeV
 1807 allowed precision studies of the Higgs boson and other SM particles, as well
 1808 as the search for new particles with higher masses.

1809 Other relevant items in ATLAS timeline are the observation and rate
 1810 measurement of $t\bar{t}$ events [152] or the evidence for rare electroweak $W^\pm W^\pm$
 1811 production [153]. The first evidence of light-by-light scattering at high
 1812 energy was also found with ATLAS [154]. The first $t\bar{t}H$ associate production
 1813 [155] and $H \rightarrow b\bar{b}$ decays [156] were observed for first time by ATLAS too.

1814 The physics programme of ATLAS include precise measurements of the
 1815 SM [157], super-symmetry studies [158], sources of \mathcal{CP} -violation [159], large

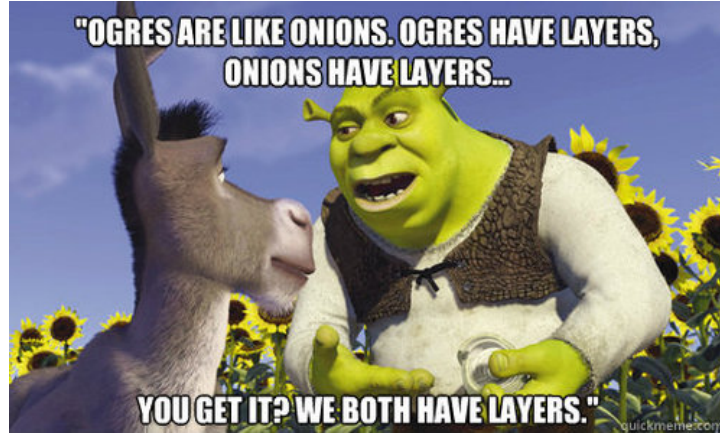


Figure 2.15: Due to its coaxial-layered structure ATLAS can be understood as cylindric onion: “*ATLAS have layers, onions have layers*” [147].

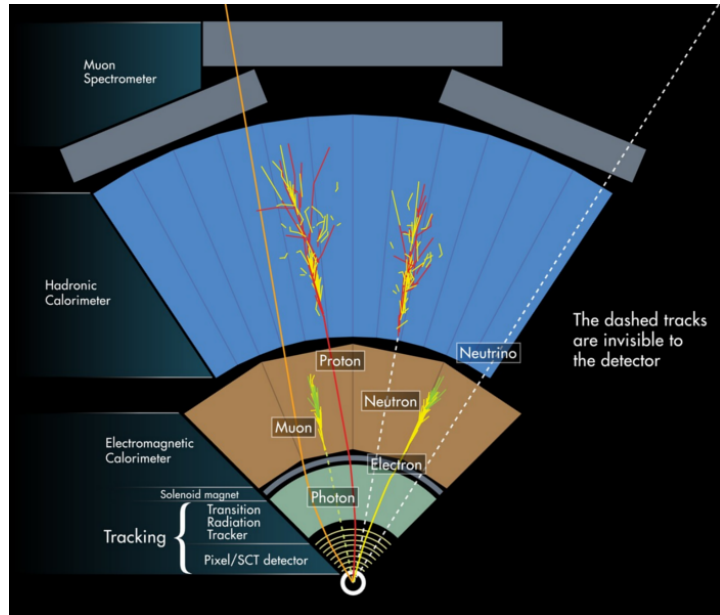


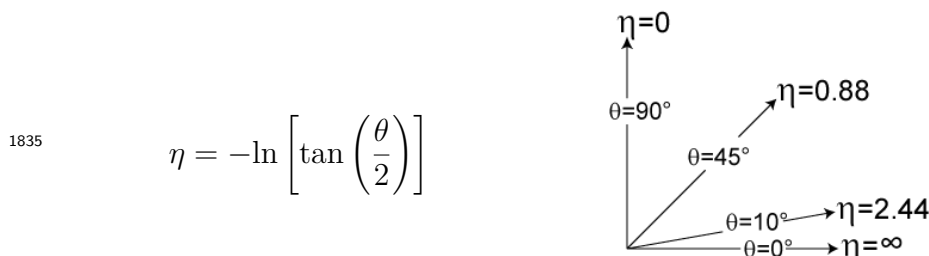
Figure 2.16: Fraction of the transversal plane of ATLAS. Each particle leaves a different signature in each layer. By signature is meant the particular distribution of energy deposition. This scheme is fundamental to understand the object reconstruction in the next chapter.

¹⁸¹⁶ E_T^{miss} dark matter searches [160], astroparticle physics [161], extra dimen-
¹⁸¹⁷ sions [162] and others.

¹⁸¹⁸ ATLAS is not only a detector but also a collaboration of people com-
¹⁸¹⁹ posed of more than 5000 members including physicists, engineers, techni-
¹⁸²⁰ cians, doctoral students and support staff. Working at CERN or at any
¹⁸²¹ of the 181 institutions that constitute ATLAS, the different teams work
¹⁸²² collaboratively to achieve success. Any output by any of the teams com-
¹⁸²³ prising ATLAS is shared with the rest of the collaboration and subjected
¹⁸²⁴ to a strict review process before making the results public, ensuring high-
¹⁸²⁵ quality standards.

¹⁸²⁶ 2.3.1 Coordinate system

¹⁸²⁷ Due to its cylindrical structure, ATLAS uses a right-handed system with
¹⁸²⁸ its origin at the IP where the collisions take place. On one side, there are the
¹⁸²⁹ ($x, y, z,$) Cartesian coordinates. The x -axis is pointing towards the centre
¹⁸³⁰ of the ring circumference, the y -axis is perpendicular to the plane defined
¹⁸³¹ by the LHC ring and it points to the surface, and the z -axis is defined by
¹⁸³² the direction of the beam. On the other side, it is more frequent to employ
¹⁸³³ the cylindrical coordinates (r, ϕ, z) or the system defined by the azimuthal
¹⁸³⁴ angle (ϕ) and the pseudorapidity (η) :



where θ is the polar angle⁴. As the polar angle approaches zero, pseudorapidity tends towards infinity. The change in pseudorapidity $\Delta\eta$ is Lorentz invariant under boosts along the beam axis. The use of η is preferred over θ because the distribution of events typically looks flat with respect to η . In terms of the momentum, the above equation can be expressed as:

$$\eta = -\ln \left(\frac{|\vec{p}| + p_z}{|\vec{p}| - p_z} \right)$$

¹⁸³⁶ being p_z the momentum along the beam direction. The rapidity is used
¹⁸³⁷ when dealing with massive particles and it can be expressed as $y = \frac{1}{2}\log[(E+$

⁴Defined as the angle between the particle three-momentum, \vec{p} and the positive direction of the beam axis.

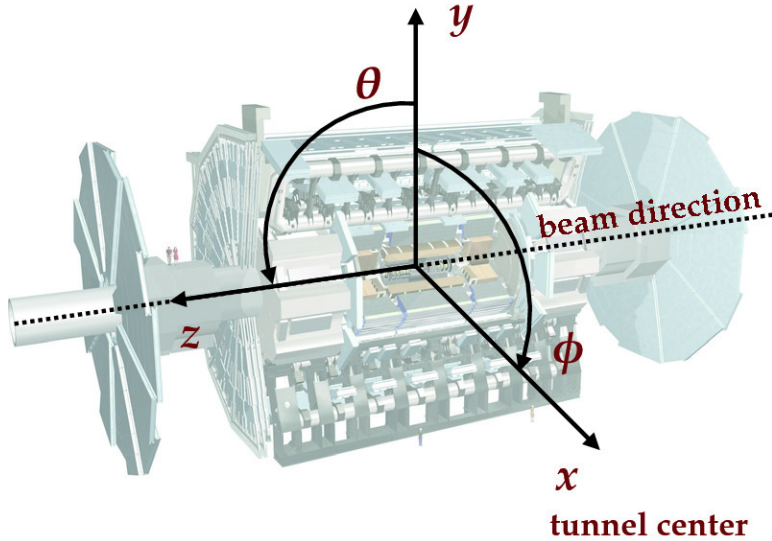


Figure 2.17: Coordinate system of the ATLAS detector.

1838 $p_z)(E - p_z)$], being E the energy projection of the momentum in the z -axis.
 1839 Note that when the particles approach the speed of light, they are in the
 1840 limit $E \approx |\vec{p}|$ and the values for rapidity and pseudorapidity converge. The
 1841 angular distance is measured in units of $\Delta R = \sqrt{(\Delta\eta)^2 + (\Delta\phi)^2}$, which is
 1842 invariant under a boost along the z -axis⁵. Figure 2.17 shows the coordinate
 1843 system of ATLAS for both Cartesian and cylindrical coordinates.

The transverse magnitudes such as the transverse momentum (p_T) and transverse energy (E_T) are defined in the x - y plane. Knowing the p_T , and the η and ϕ angles, the cartesian momentum (p_x, p_y, p_z) can be derived from:

$$\begin{aligned} p_x &= p_T \cos(\phi) & p_y &= p_T \sin(\phi) \\ p_z &= p_T \sinh(\phi) & |\vec{p}| &= p_T \cosh(\phi) \end{aligned}$$

1844 2.3.2 Inner Detector

1845 The ATLAS ID [163][164][123] is the closest sub-detector to the beam
 1846 pipe. Its layout is shown in Figures 2.18 and 2.19. The charged particles
 1847 follow a curved trajectory inside the ID due to the magnetic field of the AT-
 1848 LAS bending magnet (see 2.3.5). The different pieces that comprise the ID
 1849 can reconstruct the traces of these particles with great accuracy allowing,
 1850 thus, to measure its momentum (this is done using the sagitta method de-
 1851 scribed in Section 3.3.1.1). For particles coming from the IP, the geometric
 1852 acceptance of the ID is $|\eta| < 2.5$ for pseudorapidity and full ϕ coverage in

⁵ $\Delta\eta = \eta_2 - \eta_1$ and $\Delta\phi = \phi_2 - \phi_1$.

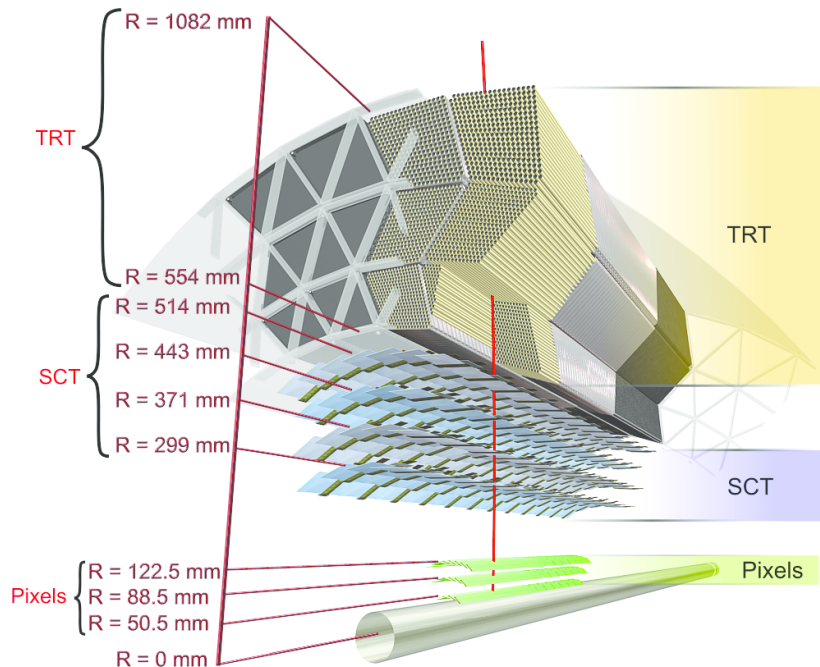


Figure 2.18: Barrel part of ID of the ATLAS experiment with the Pixel, SCT and TRT sub-detectors. The IBL is not shown here.

the azimuthal angle. The ID provides p_T resolution of $\sigma_{p_T}/p_T = 0.05\%$ GeV $\oplus 1\%$ and a transverse impact parameter resolution⁶ of $10 \mu\text{m}$ for particles in the central η region. It is designed to provide excellent momentum resolution, pattern recognition and measurements of both primary and secondary vertex for charged particles above the p_T threshold (nominally 0.5 GeV).

The ID is composed of four complementary sub-detectors: The Insertable B-Layer (IBL), the Pixel Detector, the Semiconductor Tracker (SCT) and the Transition Radiation Tracker (TRT). In the sections that follow, a description of each sub-system is provided.

Depending on the η that a particle has, it will interact with some elements of the detector. Figure 2.19 shows the end-cap elements transversed by two charged particles with $\eta = 2.2$ and 1.4 . The track with $\eta = 1.4$ traverses first the beryllium beam-pipe, then the three cylindrical silicon pixels and the four disks with double layers of the SCT. Finally, this particle travels across approximately 40 tubes in the TRT wheels. In contrast, the particle with $\eta = 2.2$ encounter the first of the cylindrical silicon-pixel layers after leaving the beryllium pipe. Then, the two end-cap pixel disks and the four last disks of the end-cap SCT.

⁶The impact parameter determine the distance of a reconstructed track from a charged particle to the perigee (the closest point of the track to the global z -axis)

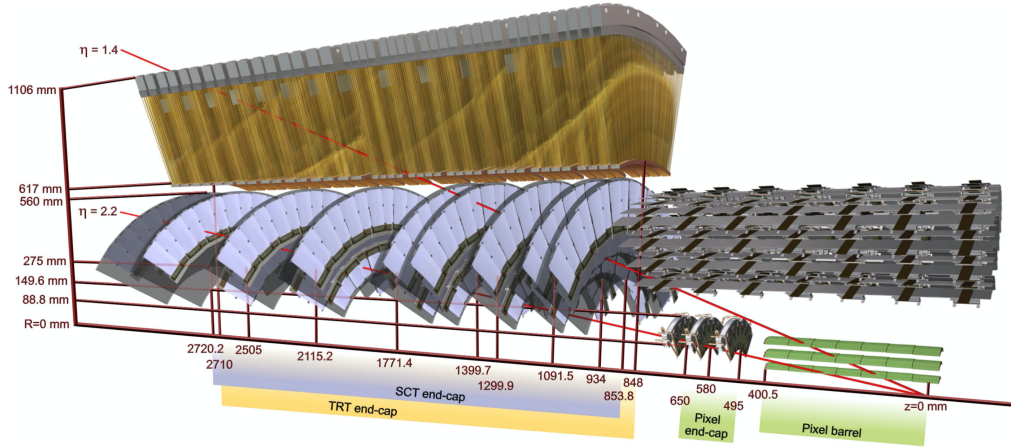


Figure 2.19: End-cap of the ID.

1871 Silicon semiconductors

1872 When a charged particle traverses a doped silicon semiconductor, it creates
 1873 a pair electron-hole by ionisation. An electric field is applied to the active
 1874 part of the detector module so that the electron drifts in oposite direction
 1875 of the electric field and the hole in the field direction. Then, both charges
 1876 are collected by the p-n junctions. The silicon sensors can be shaped either
 1877 as pixels, providing precies 2D space point, or as strips, giving a single
 1878 dimension positioning. On the order of 10^5 electron-hole pairs are liberated
 1879 when a particle crosses the silicon wafer and, with appropriate electronics,
 1880 a clear signal is obtained in the pixel or strip in which the charged was
 1881 collected.

1882 2.3.2.1 Insertable B-Layer

1883 The IBL [165] is the innermost component of the ID. It is located
 1884 between the beam pipe and the pixel detector. Added after Run-1, it
 1885 provides the closest-to-IP measurements. This improves the robustness and
 1886 performance of the ATLAS tracking system. It plays a fundamental role
 1887 for b -tagging efficiency because this tagging relies on precise vertex recon-
 1888 struction. The IBL provides redundancy in the measurements of tracks in
 1889 order to control the fake rate arising from random combinations of clusters
 1890 in events with a high pile-up background.

1891 With a hit resolution of $8\mu\text{m}$ in $r\text{-}\phi$ and $40\mu\text{m}$ along z , the IBL covers
 1892 the $|\eta| < 2.7$ and the entire ϕ range.

1893 The barrel structure if the IBL has a radius of 3.2 cm and is composed
 1894 by 14 carbon fibre staves as it is shown in Figure 2.20. Each stave has

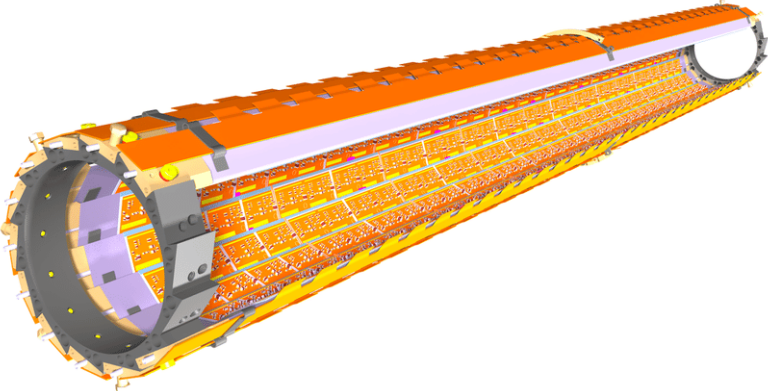


Figure 2.20: Schematic drawing of the ATLAS IBL Detector [165].

incorporated cooling CO_2 circuits, has 32 or 16 modules and uses two types of photodetectors: ATLAS pixel planar sensors and 3D pixel sensors. The used pixels have a size of $50 \times 400 \mu\text{m}^2$. Due to the high luminosity of the LHC, the IBL is built with radiation-tolerant sensors.

2.3.2.2 Pixel Detector

The ATLAS Pixel Detector [166] consists of a strip detector in the outermost layers and a pixel detector in the region which is closer to the IBL. Along with the IBL, it aims to reconstruct the trajectories of the particles traversing it. It provides a full coverage of the azimuthal angle ϕ and a pseudorapidity range of $|\eta| < 2.5$ as well as a resolution of $10 \mu\text{m}$ in $r\text{-}\phi$ and $115 \mu\text{m}$ in the z .

The Pixel Detector and the IBL combined contain 92×10^6 pixels with its respective electronic channels, which cover an area of approximately 1.9 m^2 of silicon consuming 15 kW . The barrel region consists of four concentric layers equipped with 1736 sensor modules and each of the two end-caps has three disks with 2888 modules [167]. Figure 2.22 shows the assembly view and cross section of a module of the ATLAS ID Pixel Detector. Each of these modules consists on a silicon pixel sensor bonded to the front-end electronic chips.

Hits in a pixel are read out if the signal exceeds a tunable threshold. The pulse height is measured using the Time-over-Threshold (ToT) technique.

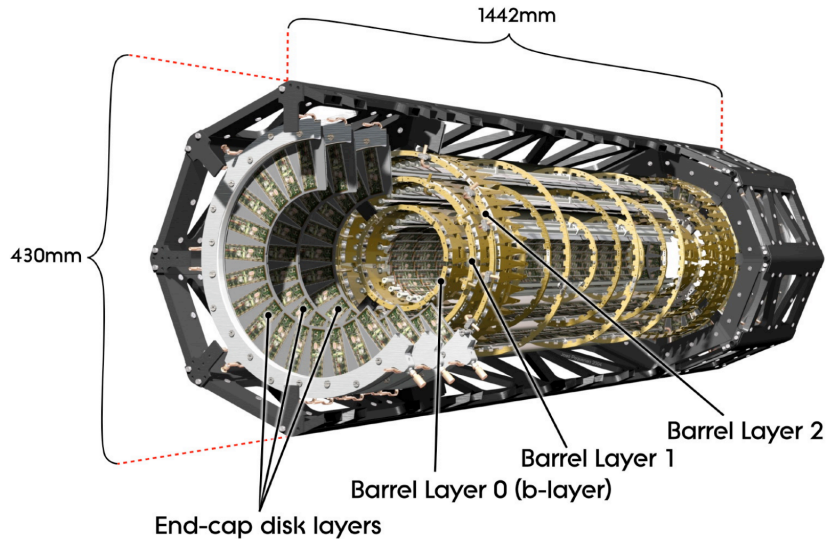


Figure 2.21: Schematic view of the ATLAS pixel detector consisting of individual barrel and end-cap layers [123].

1916 2.3.2.3 Semiconductor Tracker

1917 The SCT consists of 4088 modules tiling four coaxial cylindrical layers
 1918 in the barrel region and two end-caps each containing nine disk layers, all
 1919 of this surrounding the Pixel Detector and providing additional precision
 1920 tracking. The main difference with the Pixel Detector is that the SCT uses
 1921 microstrip sensor technology, which is very similar to that of a pixel but
 1922 being much larger (6 cm). The reason to use microstrips instead of pixels
 1923 is that the strips are more cost-effective than traditional pixels and a good
 1924 spatial resolution can be obtained as well if the strips are arranged with an
 1925 angular offset. Therefore, each SCT detector unit consists on two back-to-
 1926 back silicon-microstrip planes with a relative angle of 40 mrad. Eight strip
 1927 layers (i.e. four space points) are crossed by each track in the SCT providing
 1928 valuable tracking information with resolution of $17 \mu\text{m}$ in $r\phi$ and $580 \mu\text{m}$
 1929 in the z coordinate. The SCT covers the entire ϕ range and up to 2.5 in η .

1930 Figure 2.23 shows an exploded view of the different components of an
 1931 SCT module, including the high thermal conductivity spine, the polyimide
 1932 hybrids and readout chips.

1933 2.3.2.4 Transition Radiation Tracker

1934 The TRT is used in conjunction with the Pixel Detector and silicon micro
 1935 strip (SCT) to extend the η range in which the tracks can be reconstructed to
 1936 $|\eta| = 2$. This part of the ID is formed by a large number of 4 mm straw tubes

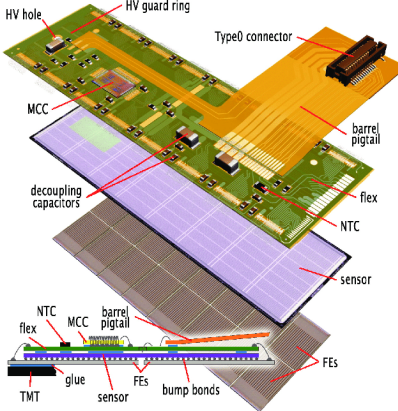


Figure 2.22: Pixel Detector module [166].

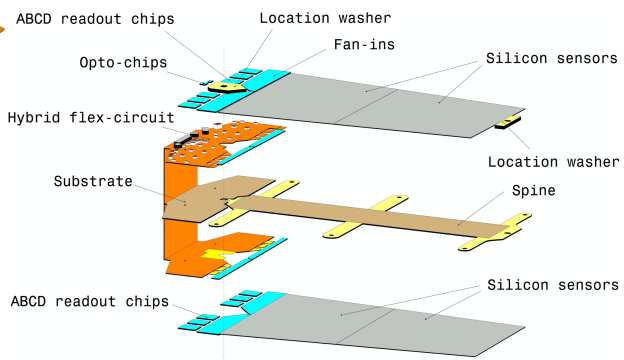


Figure 2.23: SCT detector module [123].

1937 filled with gas. This part of the ID relies both on the collection of primary
1938 ionisation charge and the collection of secondary ionisation charge arising
1939 from the transition radiation to measure the the track of charged particles.
1940 The tube surface functions as a cathode while the wire in the center as
1941 a cathode. When a charged particle pases through the gas in the tube, it
1942 ionises the gas and the freed electrons drift towards the anode, generating an
1943 electrical current. This detector provides a single hit resolution of $170\ \mu\text{m}$ in
1944 $r\text{-}\phi$ but does not have sensitivity in z . The TRT also provides discrimination
1945 between electrons and pions since the later generate a much smaller signal
1946 than the former. When the electrons pass, they produce x-ray photons that
1947 lead to strong avalanches within the tubes and, thus, a great signal.

1948 2.3.3 Calorimeters

1949 After the ID, the next layer of detectors in ATLAS correspond to the
1950 calorimeters (Figure 2.24) [168]. Their purpose is to measure the energy
1951 of the particles (neutral or charged), as well as to help to reconstruct the
1952 path followed by them. Most particles initiate a shower (Section 2.3.3.1)
1953 when they enter into the calorimeter. Part of the energy of these particles is
1954 deposited in the device, then collected and measured by it. Most of calorim-
1955 eters in particle physics are segmented transversely to provide information
1956 about the direction of the particles. Based on how the particle shower devel-
1957 ops, the longitudinal segmentation can provide information for identifying
1958 the particle (a more detailed discussion of how particles are reconstructed
1959 within the ATLAS detector is presented in Section 3.3).

1960 In general, calorimeters can be classified as sampling, when are made of
1961 two types of materials, or homogeneous, built with just one type of material.

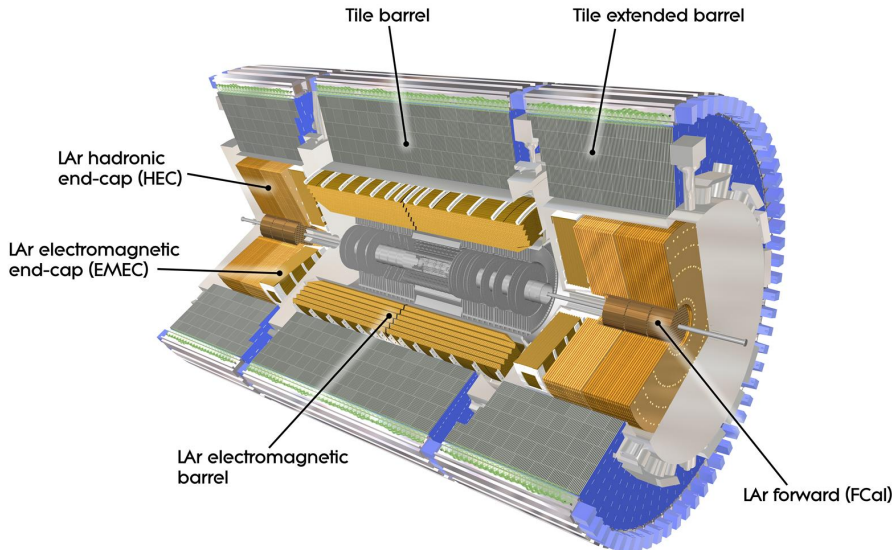


Figure 2.24: Computer generated image of the ATLAS calorimeter [167].

1962 ATLAS uses sampling calorimeters, which consist of alternating layers of
 1963 different materials:

- 1964 • **Passive material:** Also known as absorber, it is a denser material to
 1965 full stop the traversing particles. When a particle interacts with the
 1966 passive material it produces the shower (Figures 2.25 and 2.26). For
 1967 the absorber layers in ATLAS, lead is used for the ECAL and steel
 1968 for the HCAL.
- 1969 • **Active material:** This material detects the particles from the shower
 1970 originated in the absorber. The liquid Argon (LAr) is used as active
 1971 material for ECAL and plastic scintillator for HCAL.

1972 In the homogeneous calorimeters, the material used combines the features
 1973 of an absorber and a detector, performing both tasks.

1974 Since each type of particle interacts differently, there are two main types
 1975 of calorimeters: the electromagnetic calorimeter (ECAL), which measures
 1976 the energy of electrons/positrons and photons, and the hadronic calorim-
 1977 eters (HCAL), which registers the energy of the strongly-interacting particles.
 1978 Both classes are covered in the next sections.

1979 **Scintillator**

1980 The particles from the shower leave some of the molecules of the plastic

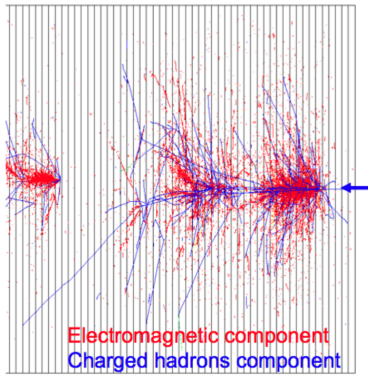


Figure 2.25: EM and hadronic cascades.

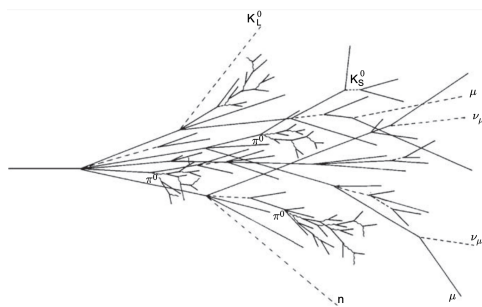


Figure 2.26: Sketch of a hadronic cascade [169].

scintillator in an excited state. The subsequent decay of these molecules produces the emission of photons in the ultraviolet energy region. This light is collected by photomultiplier tubes at the edge of the tiles and converted into a current pulse whose amplitude is proportional to the energy deposited by transversing particle.

2.3.3.1 Particle showering

A particle shower is a cascade of secondary particles produced when a high-energy particle interacts with matter. The first particle interacts with the passive material producing a secondary particle with less energy than the first one. The second particle does the same and, in each step, the particles produced are less and less energetic. For a single incoming particle, this iterative process can continue for thousands of periods [169]. An illustration of the EM and hadronic particle cascades is shown in Figure 2.25.

1995 Electromagnetic shower

The electromagnetic (EM) shower is initiated by a e^- , e^+ or γ , these three particles are the sole components of this type of shower. At energies higher than 100 MeV, the EM showering is based on two main processes: Bremsstrahlung and pair creation. The electrons lose their energy almost exclusively by bremsstrahlung radiation, a process in which the lepton radiates thousands of soft photons because of its interaction with another charged particle. The photons lose their energy by the production of an $e^- - e^+$ pair. At lower energy scales, other processes contribute. In the MeV

range, the Compton scattering⁷ and photoelectric effect⁸ are the dominant interactions for energy loss for photons, while the ionisation and excitation are for the charged particles (e^- and e^+).

Hadronic shower

When a hadron interacts with the passive material, this shower is initialised. Both strong and EM interactions are involved in the development of this type of shower and they present a larger variety of particle components. Therefore, the hadronic showers are significantly more complex than the EM. Figure 2.26 shows the processes leading to a hadronic cascade.

The production of neutral pions represents about a third of the energy loss of hadronic interactions. These pions decay 98.8% of times to two photons [170] that are starting the EM showers. The rest of hadronic interactions consist of the production of charged mesons, nuclear fragments and protons, soft neutrons and photons or unpredictable loss through undetectable processes.

2.3.3.2 Electromagnetic calorimeter

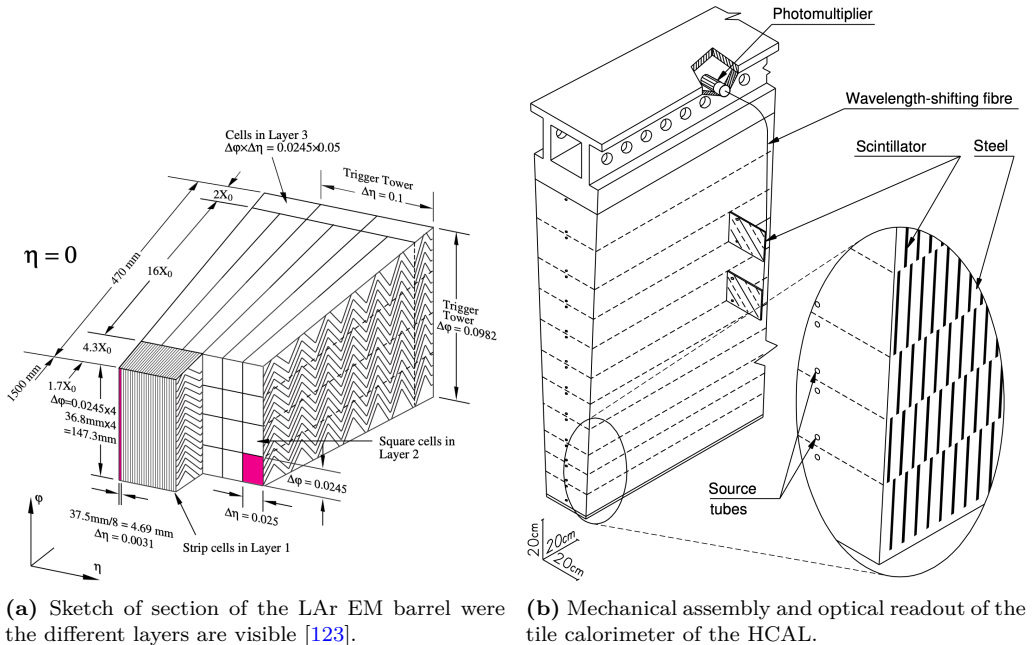
The ECAL [168] absorbs the energy of the e^- , e^+ or a γ covering a pseudorapidity range of $|\eta| < 1.475$ in the barrel. It is made of a lead absorber and LAr detector following an accordion shape, as can be seen in Figure 2.27a, where the different layers are clearly visible. The shower originated at the absorber layer ionise the LAr producing a measurable current proportional to the energy of the original particle. The LAr layer operates at 87 K.

The barrel part is split into two identical half-barrels separated by a small gap at $z = 0$. Each end-cap calorimeter is composed of two coaxial wheels that cover $|\eta| < 1.475$.

The total amount of material in the ECAL corresponds to 25-35 radiation lengths, X_0 , and 2-4 nuclear interaction lengths, λ , over the entire η range. Characteristic of each material, the ration length is the mean distance over which a high-energy electron lose all but $1/e$ of its energy by bremsstrahlung. The radiation length is the mean free path between interactions required to reduce the number of relativistic charged particles by the factor $1/e = 0.37$ as they pass through matter.

⁷Scattering of a photon after interacting with a charged particle, usually an electron.

⁸Emission of photoelectrons when the EM radiation interacts with matter.



(a) Sketch of section of the LAr EM barrel were the different layers are visible [123]. (b) Mechanical assembly and optical readout of the tile calorimeter of the HCAL.

Figure 2.27: Sketch of a section of the ATLAS (a) ECAL and (b) HCAL [123].

The energy resolution of a calorimeter can be parametrised as:

$$\frac{\sigma_E}{E} = \frac{a}{\sqrt{e}} \oplus \frac{b}{E} \oplus c = \frac{10\%}{\sqrt{e}} \oplus \frac{170 \text{ MeV}}{E} \oplus 0.7\%$$

2037 Where a is the stochastic term, b the electronic noise and c a constant that
2038 includes detector instabilities and increases with E [171].

2039 2.3.3.3 Hadronic calorimeter

2040 The ATLAS HCAL [168] is made of a sampling calorimeter of steel and
2041 plastic scintillator tiles covering the pseudorapidity region of $|\eta| < 1.7$ in
2042 the barrels. The end-caps are made of copper and LAr, covering $1.5 < |\eta| <$
2043 3.2, and are emended in the end-caps of the ECAL. This calorimeter uses
2044 9800 electronic channels in the barrel and 5600 in the end-cap. With 2900
2045 tones, the HCAL is the heaviest part of the ATLAS detector. It has 420000
2046 scintillator tiles and 9500 photomultiplier tubes [167]. All these elements are
2047 shown in Figure 2.27b, where the tiles, the fibres and the photomultipliers
2048 are visible.

The contribution of the electronic noise is negligible, therefore, the energy resolution for the tile calorimeter is [168]:

$$\frac{\sigma_E}{E} = \frac{5.9\%}{\sqrt{e}} \oplus 5.7\%$$

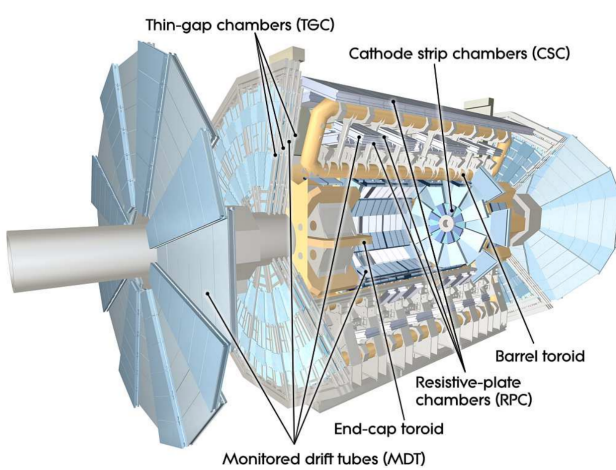


Figure 2.28: Conceptual layout of the MS (blue). The magnet system (yellow) is also shown [123].

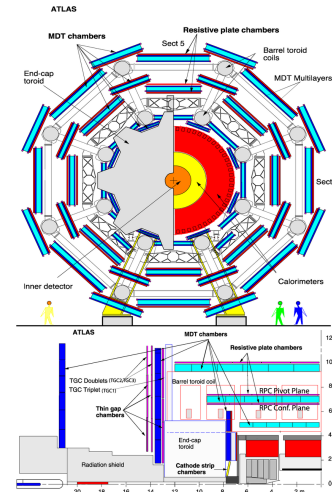


Figure 2.29: ATLAS Muon detectors.

2.3.3.4 Forward calorimeter

In addition to the ECAL and HCAL, a smaller calorimeter is placed in the end-caps surrounding the beam pipe in order to cover the forward region ($3.1 < |\eta| < 4.9$), the forward calorimeter (FCAL). This coverage is required for many physics tasks such as the reconstruction of the E_T^{miss} of the forward-jet tagging.

This calorimeter is a sampling calorimeter based on LAr as active medium and copper as absorber. The thickness of the FCAL is optimised to achieve high absorption, approximately, $10 X_0$ [171].

This detector has a resolution of:

$$\frac{\sigma_E}{E} = \frac{100\%}{\sqrt{e}} \oplus 10\%$$

2.3.4 Muon Spectrometer

The muons can penetrate through calorimeters and reach the last layer of the ATLAS detector, the MS [172]. Figure 2.28 shows a schematic cutaway view of the ATLAS muon system.

The MS surrounds the calorimeters and its aim is to measure the trajectories of muons to determine their direction and momentum with excellent tracking precision as well as their electric charge in a pseudorapidity coverage of $|\eta| < 2.7$. To bend the particle tracks after they exit the HCAL, the MS uses eight large superconducting air-core toroid magnets in $|\eta| < 1.4$

Type	Purpose	Location	Coverage
MDT	Tracking	Barrel + end-cap	$0.0 < \eta < 2.7$
CSC	Tracking	End-cap layer 1	$2.0 < \eta < 2.7$
RPC	Trigger	Barrel	$0.0 < \eta < 1.0$
TGC	Trigger	End-cap	$1.0 < \eta < 2.4$

Table 2.3: ATLAS MS sub-detectors [173].

region. For the $1.6 < |\eta| < 2.7$, the tracks are bent by magnets inserted in the end-caps. In the transition region, $1.4 < |\eta| < 1.6$, the magnetic field responsible of bending the particles is provided by both the air-core toroid magnets and the smaller end-cap magnets. These fields are perpendicular to the trajectory of the muons originated in the IP. More details about the magnet systems of the MS can be found in Section 2.3.5.

The MS instrumentation is based, on one hand, on precision chambers for the coordinate measurements in the bending plane: Monitored Drift Tube chambers (MDT) and Cathode-Strip Chambers (CSC), and, on the other hand, on trigger chambers: Resistive Plate Chambers (RPC) and Thin Gap Chambers (TGC). Table 2.3 gives a summary of the MS detector components. In Figure 2.29 the distribution of the MS detectors is described.

- **Monitored Drift Tube chambers (MDTs)** [174]: The MDT chambers provide precise momentum measurements by determining with high accuracy the curve of the tracks. This part of the MS cover a pseudorapidity range of $|\eta| < 2$. The MDTs are designed to have stand-alone measurement capability in order to safeguard against any unanticipated background and to ensure good discovery potential in the scenario of unexpected topologies. In the barrel region, the MDTs are arranged in three cylindrical stations coaxial to the beam axis and in the end-cal, the MDTs are vertically installed in three layers. An MTD chamber consists of six layers of drift tubes (as depicted in Figure 2.30), each of them with 3 cm of diameter, filled with gas. A tube can achieve a single wire resolution of $80 \mu\text{m}$ [173]. In the entire MDT system, there are 1 171 chambers with a total of 354 240 tubes.
- **Cathode-Strip Chambers (CSC)**: It is the innermost tracking layer of the MS. Due to its higher rate capability and time resolution, it is located close to the beam axis, where the particle fluxes are higher. This component of the muon detector system covers the η range $2.0 < |\eta| < 2.7$. It measures with precision the coordinates at

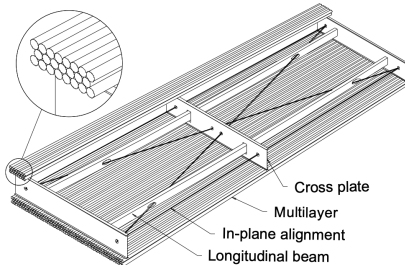


Figure 2.30: Schematic view of an MDT chamber.

2098 the ends of the detector. With its 70 000 electric channel, provides a
 2099 resolution around $60 \mu\text{m}$.

- 2100 • **Resistive Plate Chambers (RPC)** [175]: This is the barrel element
 2101 of the trigger system. These chambers are located on both sides of
 2102 the central CSC and inside the outermost CSC station. The RPCs
 2103 are gaseous detectors used for triggering and for measuring the second
 2104 coordinate in the barrel region. RCPs provide a time-space resolution
 2105 of $1\text{ cm} \times 1\text{ ns}$. The gas gap is of the order of 2 mm and the plate
 2106 external surfaces are coated by thin layers of graphite painting. This
 2107 part of the MS is composed of 3 800 electric channels.
- 2108 • **Thin Gap Chambers (TGC)** [176]: As a first-level trigger, they
 2109 have to provide high efficiency and excellent time resolution for bunch-
 2110 crossing tagging in a high-background environment. The particle flux
 2111 received by the TCG is higher than that of the RPC. The three TGCs
 2112 are located near the middle end-cap MDT station, in the forward
 2113 regions. TGCs measure the second coordinate in the non-bending
 2114 direction with its circa 440 000 electrical channels.

2115 2.3.5 Magnet system

2116 The curvature in the track of the particles is fundamental to measure
 2117 the transverse momentum and the charge of the particles. To bend the
 2118 path of charged particles, these are immersed in a homogeneous magnetic
 2119 field which is produced by the both the toroidal and solenoid magnets.
 2120 The bending power is proportional to $\int B dl$, where B is the magnetic field
 2121 component orthogonal to the charged direction.

2122 ATLAS magnetic system is divided into three subsystems: the central
 2123 solenoid magnet, the barrel toroids (BT) and the end-cap toroid (ECT).

2124 2.3.5.1 Central solenoid magnet

2125 The ATLAS solenoid surrounds the ID providing a 2 T magnetic at
2126 the centre of the tracking volume. This magnet is very thin, having only
2127 4.5 cm thickness, which minimises the interaction of the particles with the
2128 magnet material. It is important to not use a lot of material here because,
2129 otherwise, the interaction of the particles with the solenoid magnet would
2130 impact negatively in the performance of the calorimeters. To achieve such
2131 a field within a small thickness, 9 km of niobium-titanium superconductor
2132 wires into strengthened, pure aluminium strips and cooled down to 4.5 K are
2133 used. The central solenoid magnet has a cylindrical shape with a diameter
2134 of 5.6 m and a length of 2.56 m, and it weights 5 tonnes.

2135 2.3.5.2 Toroid magnets

2136 Three large air-core toroids (one barrel and two end-caps) generate the
2137 magnetic field in the MS. Each toroid consists of eight coils assembled with
2138 cylindrical symmetry (see the yellow elements in Figure 2.28). The coils are
2139 based on an aluminium stabilised Niobium-Titanium alloy (Al/NbTi/Cu)
2140 superconductor operating at 4.5 K. The main difference between the barrel
2141 and end-cap toroids for the cold mass is that the latter has a higher critical
2142 current and less aluminium than the former [177].

2143 Barrel Toroid

2144 The Barrel Toroid magnet is the largest component of the ATLAS magnet
2145 system. It generates a toroidal magnetic field which, as introduced in Sec-
2146 tion 2.3.4, is almost completely perpendicular to the track of the particles.
2147 In order to minimise the impact (i.e. reduce any interaction apart from
2148 applying magnetic field) of the magnet system with the particles, the barrel
2149 toroid is designed as an open and light structure. The barrel toroid coils
2150 are housed in eight individual cryostats, with the linking elements between
2151 them providing the overall mechanical stability. A view of the coils of the
2152 barrel toroid in their cryostats is in Figure 2.31.

2153 The magnetic flux density delivered by this magnet is 3.9 T on the su-
2154 perconductor. For the toroid barrel, the bending power ($\int B dl$) is in the
2155 interval 1.5 Tm to 5.5 Tm in $0 < |\eta| < 1.4$. It is the largest toroidal magnet
2156 ever built (25.3 m in length), being probably the most iconic and character-
2157 istic element of ATLAS. It weights 830 tonnes and uses more than 56 km of
2158 superconducting wire [167].

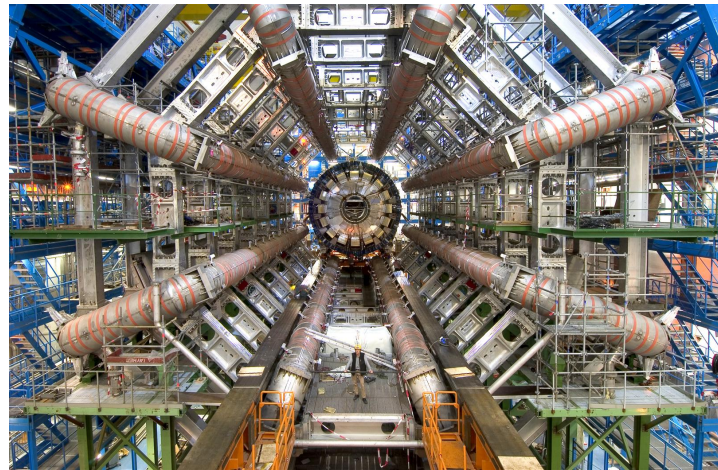


Figure 2.31: Very cool picture of the installation ATLAS calorimeters. The eight coils that compose the ATLAS barrel toroid magnets are already installed in the cryostats. Thus view is one of the most iconic of the ATLAS detector.

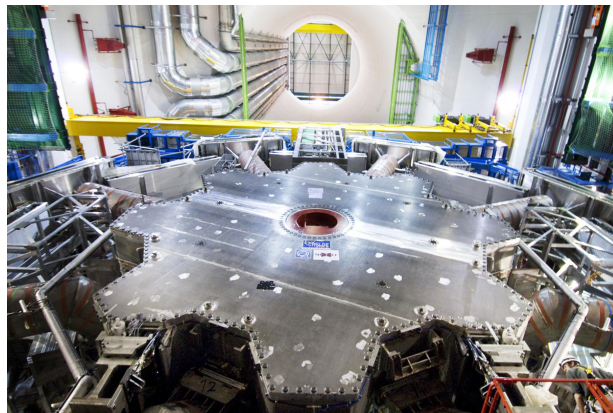


Figure 2.32: One of the two end-cap toroidal magnets. Each is made by eight superconducting coils with a magnetic field peaking at 4.1 T.

2159 **End-cap Toroid**

2160 The end-caps extend the magnetic field of the barrel toroid to the beam pipe.
 2161 These magnets are constrained by the inner radius of the barrel toroid and
 2162 the axial length of the experiment.

2163 As well as in the barrel toroid, it has a 4.1 T magnetic field on the
 2164 superconductor. For the end-cap toroid, the $\int B dl \in [4, 8]$ Tm in the
 2165 pseudorapidity range $1.6 < |\eta| < 2.7$ [177]. In the transition region where
 2166 the end-cap and barrel toroids overlap ($1.4 < |\eta| < 1.6$), the bending power
 2167 is lower. Each end-cap magnet (Figure 2.32) has a diameter 10.7 m and
 2168 weights 240 tonnes [167].

2169 2.3.6 Trigger and Data Acquisition System

2170 The proton bunches cross at the center of the ATLAS detector 40 million
2171 times per second, resulting in approximately (using Run-2 mean pile-up
2172 $\langle\mu\rangle = 33.7$) 1 200 million proton collisions per second. Reading out and
2173 storing all the information from this interactions is not feasible since it has a
2174 combined data volume of more than 60 million megabytes per second. Only
2175 some of these events are of interest to physics studies and, consequently,
2176 only this subset need to be saved into permanent storage for later analysis.
2177 In order to select only interesting data, ATLAS uses a complex and highly
2178 distributed Trigger and Data Acquisition System (TDAQ) [178] that reduces
2179 the rate of recorded data from the initial 1 200 MHz of interactions to just
2180 an average of 1 kHz. The reduction through the trigger is carried in two
2181 steps: The electronic performs an initial selection and, afterwards, a large
2182 computer farm analyses the data that pass the initial filter.

2183 The TDAQ system is an essential component of ATLAS in charge of
2184 processing the events online, selecting the relevant ones and storing them.
2185 To do so, the TDAQ verifies for each bunch crossing if at least one among the
2186 hundred conditions is satisfied. These conditions, also known as “triggers”,
2187 are based on identifying both combinations of candidate physics objects
2188 (“signatures”) and global properties of the events [179]. Figure 2.33 shows
2189 a diagram of the TDAQ system, in this figure can be seen the different
2190 components as well as the detector read-out and data flow.

2191 The first-level trigger (LVL1) is a hardware-based filter performed by
2192 ATLAS sub-detectors. The LVL1 uses the information of the Calorimeters
2193 and the MS to select events up to the maximum-readout rate of the detector
2194 (100 kHz) within a latency of $2.5 \mu\text{s}$. Additionally, the LVL1 identify the
2195 regions of interest (RoI), which includes the position and the p_T of the
2196 candidate objects.

2197 For each event accepted by the LVL1, the Front-End (FE) detector elec-
2198 tronics read the detectors data and pass it to the ReadOut Drivers (ROD).
2199 The ROD performs the initial processing and formatting and the ReadOut
2200 Systems (ROS) buffers this data.

2201 The data from the different sub-detectors is sent from the ROS to the
2202 software-based trigger, the so called “High Level Trigger” (HLT), when is
2203 requested by the HLT. This system is comprised by the second-level trig-
2204 ger (LVL2) and the Event Filter (EF or third-level), both made of several
2205 farms of computers (about 40 000 CPU cores) interconnected by Ethernet
2206 networks. Using modest computing power, LVL2 provides high rejection
2207 power with fast and limited precision algorithms. With higher computing
2208 power, the EF features lower rejection power with slower but higher preci-

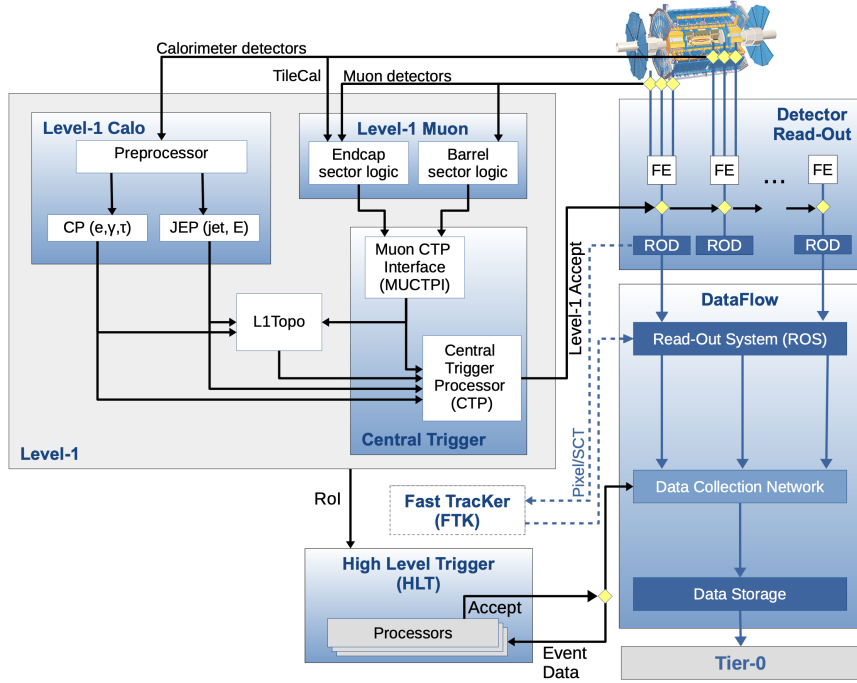


Figure 2.33: The ATLAS TDAQ system in Run-2.

sion algorithms [178]. This combination is a cost-effective and flexible way of implementing the HLT. The ID, which was not used by the LVL1, is of key importance for the HLT because on, one hand, the LVL2 reconstruction algorithms are specifically designed to meet strict timing requirements and, on the other hand, the track reconstruction on the EF is less time constrained. This is done by the ID's Fast TracKer (FTK) as the Figure 2.33 shows.

An average 1.2 kHz output rare for Run-2 pass the HLT (with a latency of just $200\ \mu\text{s}$) and is sent by the Sub-Farm Output (SFO) to the Tier-0 facilities for permanent storage and later offline physics analysis. It is important to highlight that the decisions performed by trigger about whether or not to store an event are irrevocable. If an event does not pass the trigger requirements, it is lost forever.

2.3.7 ATLAS upgrade towards HL-LHC

The LHC Run-3 started on April of this year ([esto está escrito en marzo, así que habrá que ver si es verdad](#)). This is the las data-taking period of the of the collider as it was initially designed. CERN has embarked on a very ambitious project, the High Luminosity Large Hadron Collider (HL-LHC), that will dominate the accelerator-based particle physics scen-



Figure 2.34: Timeline for the LHC and LHC HL projects. The periods of data taking are named Runs and, between runs, there are the Long Shutdowns (LS) in which the different facilities are upgraded.

2228 ario in the years to come. The HL-LHC consists on a luminosity-enhanced
 2229 version of the LHC.

2230 Adding more particles to the bunches and focusing more the beam, would
 2231 result on a grater collision rate (of about a factor 10). This provides the
 2232 different analyses with better statistics, which eventually results in more
 2233 precise searches and measurements. A peak instantaneous luminosity of
 2234 $\mathcal{L} = 7.5 \times 10^{34} \text{ cm}^2 \text{ s}^{-1}$ is expected, this corresponds to between 140 and
 2235 200 inelastic pp collisions per bunch crossing, in contrast to the current 36.1
 2236 recorded during last year of Run-2 (Figure 2.10 shows the $\langle\mu\rangle$ for each year
 2237 of Run-2).

2238 In contrast to the timeline in Figure 2.34, the latest update of the sched-
 2239 ule dates the Long Shutdown 3 (LS3) start in 2026 and the Run-4 start in
 2240 2029. All dates are subject to change as the unexpected events may occur
 2241 or technical/scientific reasons may lead to re-schedules.

2242 Some technologies developed to upgrade the LHC to HL-LHC are:

- 2243 • Shorter bending dipole magnets are going to be installed. The current
 2244 ones have a length of 15 m while the new are only 5.5 m, allowing
 2245 the insertion of the colliamtors of Figure 2.35. The new niobium-tin
 2246 dipole magnets will generate an 11 T magnetic field compared with
 2247 the current 8.3 T.

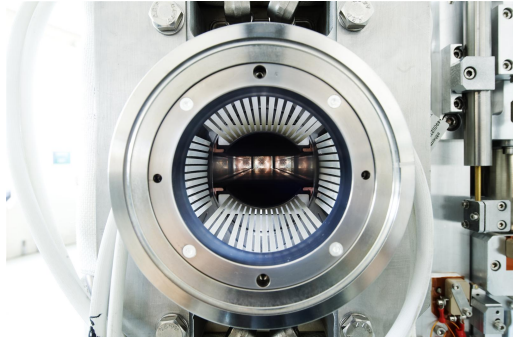


Figure 2.35: HL-LHC Collimator.

- 2248 • Brand new and more powerful superconducting quadrupole magnets
- 2249 (up to 12 T) made of niobium and tin will substitute the current ones
- 2250 (8 T). These magnets will be located at the sides of the ATLAS and
- 2251 CMS detectors
- 2252 • New Beam optics. At present, as bunches cross, the protons collide
- 2253 and disappear and, hence, the luminosity decreases. For the Run-4,
- 2254 in order to keep the luminosity at the same level, the beam focusing
- 2255 is designed to keep the collision rate constant.
- 2256 • Superconducting crab cavities for giving the bunches additional trans-
- 2257 verse momentum in order to increase the probability of collisions.
- 2258 • New collimator sand injection magnets will also improve the perfor-
- 2259 mance of the machine.
- 2260 • Thanks to the new high-temperature superconductors, currents up to
- 2261 10^5 Amperes will be carried over long distances.
- 2262 • New collimators that produce less electromagnetic interference with
- 2263 the beam are being installed. Collimators (Figure 2.35) are important
- 2264 because the machine protection is based on them. This elements of
- 2265 the accelerator absorb particles that stray from the beam trajectory
- 2266 and can harm the devices.
- 2267 • The accelerator chain is improved as well with the use of the linear
- 2268 accelerator LINAC4 and with upgrades in the PSB, PS and PSP.

2269 Although increasing the collision rate of the beams is a crucial goal for
 2270 CERN, improving the accelerator is not enough. The current detectors have
 2271 not been designed for HL-LHC but for the LHC and, thus, cannot handle
 2272 the increased luminosity. By increasing the luminosity while keeping the
 2273 same bunch spacing, a much higher rate of collisions per bunch crossing is

2274 achieved and this implies a higher pile-up. For Run-2, the pile up peaked
2275 around $\mu_{max} \approx 70$ and that was already quite taxing for the system in terms
2276 of tracking and reconstruction, and for Run-4 it may start around 140 and
2277 increase to 200 interactions per bunch crossing.

2278 Next, the main upgrades of the ATLAS detector towards the HL-LHC
2279 project are presented.

2280 **Inner Tracker** The elements in the ID receive a lot of radiation damage
2281 due to the huge rate of particles hitting the detector. This radiation environment
2282 will be even more daunting in the HL project. Therefore, the design
2283 of ATLAS (as well as all other main detectors of LHC) has to be reviewed,
2284 especially for the most central parts of the detector.

2285 To deal with this, ATLAS needs much more capable trackers, therefore,
2286 the entire ID is going to be replaced with a new “inner tracker” (ITk).
2287 This new detector consists of cylinder and end-caps equipped with silicon
2288 detectors covering a geometrical acceptance of $|\eta| < 4$. This expanded
2289 pseudorapidity range introduces many advantages in terms of object recon-
2290 struction and pile-up mitigation by linking objects to the primary vertex
2291 corresponding to the hard-scatter of interest. The new pixel sensors will
2292 be placed very close to the interaction region, where the high fluencies
2293 ($2 \times 10^{16} n_{eq} \text{cm}^{-2}$ in the HL vs the current $10^{15} n_{eq} \text{cm}^{-2}$) have to be tolerated
2294 while maintaining a 96% efficiency of particle detection [166].

2295 As well as the ID, the ITk is divided in two subsystems mounted in
2296 the pixel support tube: the pixel detectors and the strip detectors that
2297 surrounds the pixels. For the strips, there are four barrel layers and six
2298 end-cap petals and for the pixels, five layers are used.

2299 **Calorimeters** Due to radiation tolerance limits, the electronics for the
2300 ECAL and HCAL have to be updated. The on-detector FE electronics
2301 cannot operate with the trigger rates and latencies required for the HL-
2302 LHC luminosities. The FCAL will remain the same as in Run-2.

2303 **Muon Spectrometer** The MS upgrades for the HL-LHC are focused on
2304 the muon trigger chambers. The Level-0 trigger electronics of the RPC and
2305 TCG will be upgraded and for the RPC the pseudorapidity coverage will be
2306 significantly increased. The front-end of the MDT is going to be replaced
2307 as well to address the trigger rate and latency requirements.

2308 **Trigger and Data Acquisition**
 2309 **system** To reconstruct the events
 2310 offline, they have to be recorded in
 2311 the first place, otherwise, it makes
 2312 no sense to have that huge pp col-
 2313 lision rate. This is why while the
 2314 detector hardware is being heavily
 2315 upgraded, a lot of effort is being put
 2316 into the trigger systems. The new
 2317 trigger system is a multistage sys-
 2318 tem that progressively takes more
 2319 and more detailed information and
 2320 each step has more time to make
 2321 this decision. It starts with 40 MHz
 2322 input rate (40^6 input events per
 2323 second). The triggering process
 2324 starts by the Level-0 (Figure 2.36
 2325 in purple) and makes very quick
 2326 decisions ($10\mu s$ latency), reducing
 2327 the rate from 40 to 1 MHz. Af-
 2328 terwards it passes to the event fil-
 2329 ter (Figure 2.36 in orange) which
 2330 takes the 1 MHz down to 10 kHz
 2331 that sends to permanent storage.
 2332 The key part is that these 10 kHz
 2333 are really the most useful 10 kHz
 2334 [180]. For doing so, the perfor-
 2335 mance of the tracking is fundamen-
 2336 tal for things like particle flow identi-
 2337 fication, E_T^{miss} measurements, jet tag-
 2338 ging or tau identification.

2339

2340 **From ATLAS Digest: weekly news – 11 February 2022** "Con-
 2341 cerning the High Luminosity LHC, with the new schedule, LS3 will start in
 2342 2026 and the Run 4 would start in 2029. A new HL-LHC running param-
 2343 eters baseline is under discussion, which leads to new projections foreseeing
 2344 715/fb of pp data collected in Run 4. The beam energy for HL-LHC has
 2345 also been discussed and several scenarios to reach 7 TeV per beam have been
 2346 discussed. The high risk of warm-ups is a main concern and the decision
 2347 will likely be postponed to the end of Run 3. Options to stay at 6.8 TeV or
 2348 even backing off to 6.5 TeV to further avoid warm-ups are still on the table.

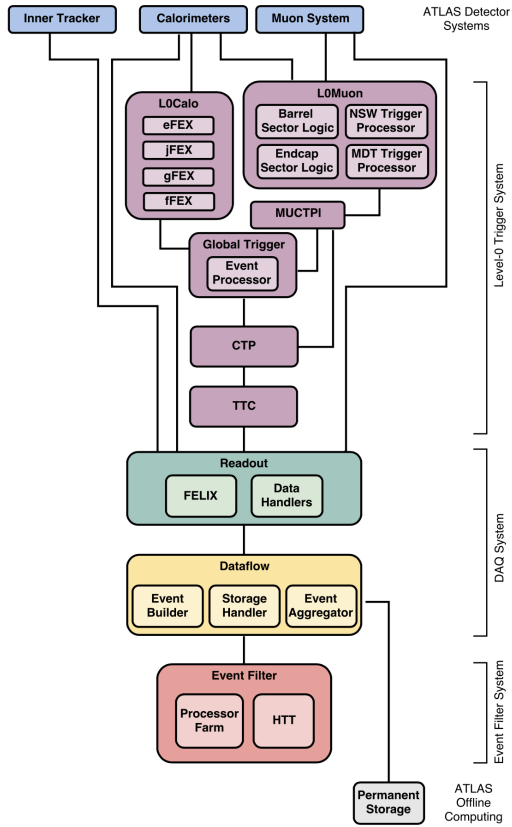


Figure 2.36: Design of the TDAQ Phase-II upgrade architecture, highlighting the organisation of the Upgrade Project in three main systems [180]. Direct connections between each Level-0 trigger component and the Readout system are suppressed for simplicity.

2349 Concerning the Nb3Sn inner triplets, full scale preseries prototypes are in
2350 production."

2351 **2.4 Alignment of the inner detector**

2352 **2.4.1 Alignment requirements**

2353 **2.4.1.1 Local coordinate frame**

2354 **2.4.1.2 Track parameters**

2355 **2.4.1.3 Residuals**

2356 **2.4.2 Track based alignment**

2357 **2.4.2.1 Global χ^2 algorithm**

2358 **2.4.2.2 Weak modes**

2359 **2.4.2.3 Alignment levels and degrees of freedom**

2360 **2.4.3 Alignment results during Run-2**

2361 [Preguntar a Paolo sobre esto](#)

2362 **2.4.4 Alignment towards Run-3**

2363 [Preguntar a Paolo sobre esto](#)

2364 **2.4.4.1 Pseudo-real-time-online monitoring**

2365 **Chapter 3**

2366 **Data and simulated events and
2367 object reconstruction**

2368 [181]

2369 **3.1 Data**

2370 Datasets

2371 **3.2 Monte Carlo**

2372 <https://inspirehep.net/literature/856179> In this section I
2373 should describe the generalities of the MC generators and in the
2374 Section4 the specifics for this analysis

2375 From ATLAS Digest: weekly news – 11 March 2022 (use
2376 to write some comments) Reducing negative weights in Sherpa
2377 (Frank Siegert) With the expected very large increase in size of samples
2378 in future runs, Monte Carlo samples will not be able to scale with the accu-
2379 mulated data, as needed for physics performance, without strong develop-
2380 ments in several areas of the simulation. The event generation is projected
2381 to take approximately 20% of the CPU resources and is the single largest
2382 component in CPU consumption of the simulation. It is therefore extremely
2383 important that strategies, that are not just to produce more since it is not
2384 a computationally viable solution to improve on the statistical uncertainty
2385 of the samples, be pursued. Frank discussed the importance of reducing the

2386 fraction of negative weights to improve the effective statistical uncertainty
2387 of weighted samples in Sherpa.

2388 He described a three-fold solution he has proposed in collaboration with
2389 Sherpa co-authors (available here) to reduce the fraction of negative weights.
2390 The three proposed methods correspond to approximations done for (i) the
2391 generation of events with soft emissions (S), (ii) the generation of events
2392 with hard emissions (H) and (iii) the use of a differential K-factor for leading
2393 order Matrix Elements with large numbers of emissions. Reducing negative
2394 weights necessarily leads to approximations and possible biases. Frank de-
2395 scribed in detail a comparison of the three methods. Differences are within
2396 the systematic uncertainties of the produced samples. These methods show
2397 that an improvement in equivalent statistics of a factor of approximately
2398 two can be achieved. **end of ATLAS Digest**

2399 **3.2.1 MC simulations**

2400 The generation of the simulated event samples includes the effect of
2401 multiple pp interactions per bunch crossing, as well as the effect on the
2402 detector response due to interactions from bunch crossings before or after
2403 the one containing the hard interaction.

2404 **3.2.1.1 Parton shower simulation**

2405 **3.2.1.2 Hadronisation simulation**

2406 **3.2.1.3 Underlying decay simulation**

2407 **3.2.1.4 Hadron decay simulation**

2408 **3.2.1.5 Pile-up simulation**

2409 **3.2.2 MC generators**

2410 **3.3 Object reconstruction and identification**

2411 To reconstruct the physical objects, the information of all the sub-
2412 detectors and systems of ATLAS is employed. A detailed description of
2413 all of them is presented in Section 2.3. After passing the trigger preselec-
2414 tion, the raw data is analysed to build the physics objects that constitute

2415 the subject of the physical analyses. The process of constructing this ele-
2416 ments is known as reconstruction. Figure 2.16 illustrates how each particle
2417 interacts with the different layers of the ATLAS detector. The reconstruc-
2418 tion objects are the particles tracks and vertices, the leptons, the photons,
2419 jets (and their flavour tag) and the missing transverse momentum.

2420 **3.3.1 Tracking**

2421 The detection and measurement od charged particles moment is an es-
2422 sential aspect of any large particle physics experiment. Regardless of the
2423 medium through which a charged particle travels, it always leaves a trails
2424 of ionised atoms and liberated electrons. By detecting this it is possible to
2425 reconstruct the trajectory of a charged particle. ATLAS does this trough
2426 its silicon detectors.

2427 The trajectories followed by particles are referred as “tracks”. For
2428 charged particles, the tracks are reconstructed using, mainly, the inform-
2429 ation of the ID and, in the case of muons, the MS. A charged particle
2430 passing thought the ID will interact with its active sensors, the pixel detector
2431 and SCT (Figures 2.22 and 2.23 respectively) providing a three-dimensional
2432 measurement of space-points. While each hit in the pixel detector is directly
2433 translated into a space-point, for the SCT two hits are needed to reconstruct
2434 one space-point. These space-points can be given by a single pixel activa-
2435 tion or by several neighbouring pixels activated simultaneously. Since the
2436 ID is submerged in a solenoidal magnetic field, the charged particles have
2437 their trajectories curved by the Lorentz force, this allows to calculate its p_T
2438 using the sagitta method. The track reconstruction is performed in two s

2439 **Highlight the importance of the alignment for the object defin-
2440 ition and its reconstruction. Link this section with 2.4**

2441 **3.3.1.1 Sagitta method**

2442 **3.3.2 Vertices**

2443 **3.3.3 Electrons and photons**

2444 **3.3.4 Muons**

2445 **3.3.5 Jets**

2446 At accelerator based detectors, quarks and gluons are detected by the
2447 jets of hadronic particles that they produce in the detector soon after they
2448 are created (remember that, as stated in Section 1.1.4, free quarks are sup-
2449 pressed due to color confinement). An exception to this rule are the top
2450 quarks, whose lifetime is smaller than the hadronisation time by two orders
2451 of magnitude and, hence, they are detected by its decay products. For the
2452 gluons and the rest of quarks, hadronisation showers (Section 2.3.3.1) take
2453 place and jet clustering algorithms merge the clusters and tracks produced
2454 by these jets to reconstruct them. In the majority of ATLAS analyses, the
2455 “Anti- k_t ” algorithm is used [182] to analyse the data from hadronic col-
2456 lisions. Modelling the jet as a cone, the algorithm uses a specific choice
2457 of radius parameter (R) defining the radial size of the jet. The distance
2458 between all pairs of objects i and j (d_{ij}) and the distance between the
2459 objects and beam pipe (d_{iB}) are used in:

$$d_{ij} = \min(k_{ti}^{2p}, k_{tj}^{2p}) \frac{\Delta_{ij}^2}{R^2}$$

$$d_{iB} = k_{ti}^{2p}$$

where

$$\Delta_{ij}^2 = (y_i - y_j)^2 - (\phi_i - \phi_j)^2$$

2460 and k_{ti} , y_i and ϕ_i are respectively the transverse momentum, the rapidity
2461 and the azimuthal angle of object i . The parameter p accounts for the
2462 relative power of the energy versus geometrical (Δ_{ij}) scales. For the Anti-
2463 k_t , p is set to -1 . Other clustering algorithms use different choices of p such
2464 as $p = 0$ (Cambridge/Aachen algorithm) or $p = 1$ (inclusive k_t algorithm).

2465 The algorithm iterates over the topological-cluster (or, simply, top-
2466 clusters) objects of the calorimeter as it follows: First it proceeds to identify
2467 the smallest distances with among all the combinations of d_{ij} and d_{iB} . If
2468 the distance is a d_{iB} , the entity i is labeled as “jet” and removed from the

2469 list of entities. If, on the contrary, it is a d_{ij} , the objects i and j are merged
2470 together. This way, before clustering among themselves, soft components
2471 (low- p_T) tend to be merged to the hard ones (high- p_T). Then the distances
2472 are recalculated and the process repeated. This is done iteratively until all
2473 entities are assigned to a particular jet.

2474 If a hard particle has no hard neighbours within a $2R$ distance, all soft
2475 particles will be assigned to it, resulting in a perfectly conical jet. But if
2476 another hard particle is present in that $2R$ distance, then there will be two
2477 hard jets and it will be impossible for both to be perfectly conical.

2478 **Work in progress**

2479 Typically, the cone size R is selected to be 0.4 or 0.6, though the most
2480 standard used in ATLAS is 0.4. If $R = 1$, the jet is labeled a Large- R and
2481 if $R = 0.4$ then as Small- R jet.

2482 **3.3.5.1 Jet energy calibration and resolution**

2483 **3.3.5.2 Bottom quark induced jets**

2484 In general, it is impossible to determine which quark flavour was pro-
2485 duced or even or whether the jet was originated by a quark or a gluon.
2486 However, if a b quark is created, the hadronisation will produce a jet of
2487 hadrons, one of which will be a b -type hadron (B hadron). The B hadrons
2488 turn out to be relatively-long-lived particles (1.5×10^{-12} s). If this larger
2489 longevity is combined with the Lorentz time-dilation that particles exper-
2490 ience when produced in high energy collisions, it results in the B hadron
2491 traveling on average a few mm before disintegrating.

2492 As a result, the experimental signature of a b quark is a jet of particles
2493 emerging from the point of collision (primary vertex) and a secondary vertex
2494 resulting from b -quark decay that is several mm away from the primary
2495 vertex. Therefore, the capacity to resolve secondary vertices from the parent
2496 vertex is crucial for identifying b -quark jets.

2497 **3.3.6 Missing transverse energy**

2498 **3.3.7 Overlap removal**

2499 **Chapter 4**

2500 **Probing the top-quark
2501 polarisation in the single-top
2502 *t*-channel production**

2503 The polarisation paper: [2504 https://atlas-glance.cern.ch/atlas/
analysis/papers/details.php?id=13286](https://atlas-glance.cern.ch/atlas/analysis/papers/details.php?id=13286)

2505 **4.1 Introduction**

2506 Apart from the studies of the associated production of a top quark and
2507 a Higgs boson, in this thesis is also presented a simultaneous measurement
2508 of the three components of the top-quark and top-antiquark polarisation
2509 vectors in *t*-channel single-top-quark production.

2510 The single-top-quark production and decay via the Wtb vertex, provides
2511 a unique way to study the coupling between the top-quark, the W boson
2512 and the b quarks. This vertex is studied through the measurement of the
2513 polarisation observables for events produced in pp collisions.

2514 Importance of signal selection: In the polarisation analysis we look at an-
2515 gular distributions. The use of a BDT or NN as it is done on the tHq studies
2516 can introduce bias on this angular distribution. This studies are extremely
2517 sensible to any bias introduced on the angular distributions, therefore a
2518 count and cut method for the signal selection is the safest option.

2519 **4.2 Top quark polarisation observables**

2520 **4.3 Simulated event samples**

2521 **4.4 Object reconstruction**

2522 **4.5 Trigger requirements and event preselec-
2523 tion**

2524 **4.6 Top quark reconstruction**

2525 A proper determination of the top quark 4-momentum is crucial to per-
2526 form the polarisation measurements. If this is not done properly, the angular
2527 variables can not be properly obtained and the sensibility of the analysis
2528 is consequently reduced. The top quark is reconstructed using a kinematic
2529 likelihood fit (KLFIT)

2530

Chapter 5

2531

Search for rare associate tHq 2532 production

2533

5.1 Introduction

2534

Describe the strategy for the $2\ell + 1\tau_{\text{had}}$ analysis

2535 The study of the tHq production can be classified attending to the
2536 the number of light-flavour leptons (ℓ), i.e. electrons or muons, and
2537 hadronically-decaying tau leptons (τ_{had}). According to this criteria, the
2538 channels presented in Table 5.1 have been defined. As can be seen in the
2539 table, the study of the 1ℓ channel uses only the $H \rightarrow t\bar{t}$, which is the most
2540 dominant decay mode for the Higgs boson with a 58% BR as is reported in
2541 Section 1.3.3. However, for the multileptonic channels the $H \rightarrow W^+W^-$,
2542 $\rightarrow \tau^-\tau^+$ and $\rightarrow ZZ$ are considered. These three Higgs decay channels
2543 combined account for a total 21% BR.

#	0 τ_{had}	1 τ_{had}	2 τ_{had}
1l (e/μ)	$tHq (b\bar{b})$ 1ℓ		$tHq (WW/ZZ/\tau\tau)$ $1\ell + 2\tau_{\text{had}}$
2l (e/μ)	$tHq (WW/ZZ/\tau\tau)$ $2\ell \text{ SS}$	$tHq (WW/ZZ/\tau\tau)$ $2\ell + 1\tau_{\text{had}}$	
3l (e/μ)	$tHq (WW/ZZ/\tau\tau)$ 3ℓ		

Table 5.1: Different channels for tHq production according to the presence of light-flavoured leptons and hadronically-decaying taus in the final state.

Moreover, depending on the relative charge between the light charged leptons, the $2\ell + 1\tau_{\text{had}}$ channel is further subdivided in two sub-channels. The so-called $2\ell \text{SS} + 1\tau_{\text{had}}$ channel is defined by the events in which the two light leptons have the same electric charge. In contrast, the one in which they have opposite electric charge is known as $2\ell \text{OS} + 1\tau_{\text{had}}$ channel. For simplicity, through this document, these two sub-channels are usually referred just as SS and OS respectively.

The work of this thesis is focused in the $2\ell + 1\tau_{\text{had}}$ channels. To do so, the $2\ell \text{SS} + 1\tau_{\text{had}}$ and $2\ell \text{OS} + 1\tau_{\text{had}}$ are treated separately since they have completely different background compositions, being the $2\ell \text{SS} + 1\tau_{\text{had}}$ the one with the lower background contribution.

- different MVAs trained for each channel

When assuming that one of the light-flavoured leptons is originated from the Higgs-boson decay and the other one from the top-quark decay, the determination of which lepton comes from which particle is direct for the $2\ell \text{OS} + 1\tau_{\text{had}}$ but not for the $2\ell \text{SS} + 1\tau_{\text{had}}$. Since knowing the origin of the light-flavoured leptons can be very useful to define variables with the power to discriminate the tHq signal from the background, tools are developed to associate these leptons to its parent particles.

- The fake estimates are being checked to see if there is anything that has to be treated differently for the two sub-channels.

5.2 Data and simulated events

the tH samples were done with MadGraph5_aMC @ NLO++Pythia8+EvtGen

The underlying event is generally done with Pythia8 in ATLAS. In the tHq samples we used MadGraph5_aMC@ NLO for the calculation of the matrix element and Pythia8 for the hadronisation and parton showering. We are also working on alternative samples with Herwig7 as parton shower generator. **While in section 3 I describe how the events and samples are generally generated and simulated, in this section I should describe what is specifically used in this analysis**

2575 5.3 Object definition and reconstruction

2576 5.4 Signal

2577 In this section, it is discussed how it is find what we know as signal.
 2578 In a particular study, the “signal” is the set of events in the dataset that
 2579 correspond to the process of interest. Therefore, in this case, the signal
 2580 is composed by tHq production events with a $2\ell + 1\tau_{\text{had}}$ final state. In
 2581 contrast, the background processes are those which, a priori, look like the
 2582 signal process but it is not.

2583 5.4.1 Signal generation and validation

2584 **rivet**

2585 5.4.2 Parton-level truth validation

2586 > Describe what are truth level and reconstruction level.
 2587 > The truth information is whatever comes from the generator, the
 2588 physics without taking into account the effects of the detector. The truth
 2589 level does not include the effects of the interaction with matter. The truth
 2590 also includes the parton shower and hadronisation information.
 2591 > $\text{truth} = \text{generator} + \text{parton shower} + \text{hadronisation}$
 2592 > The studies I did were done at generator level
 2593 > Particle level is part of truth information
 2594 > Detector level = reconstruction level + calibration +
 2595 > Creo que esto se explica bien en la tesis de florencia
 2596 (**maybe write the calculations of BR_tHq in the Section 5.4.2**)
 2597)

2598 5.4.3 Lepton assignment

2599 The two light leptons in the final state of the $2\ell + 1\tau_{\text{had}}$ channel can
 2600 originate either from the Higgs boson or the top quark. The ambiguities
 2601 regarding the origin of these light-flavoured leptons, make the reconstruction
 2602 of the top quark and Higgs boson systems extremely difficult. Nevertheless,

2603 the electric charge of these leptons could provide us useful information to
 2604 probe their origins.

2605 To have knowledge of whether the light-flavoured leptons in the final
 2606 state are originated from the Higgs boson or the top quark is very beneficial
 2607 in order to both reconstruct the event and design variables at reconstruction
 2608 level with high discriminant power. As is show in Sections 5.6.3 and 5.6.4,
 2609 the variables using the lepton assignment information play a relevant role
 2610 not only in the definition of the signal-enriched section but also the in
 2611 the determination of the control regions to constrain the most important
 2612 background processes.

2613 According to the calculations performed by combining the BR of the
 2614 Higgs boson, the top quark and all its decay products (see Section 5.4.2),
 2615 in the $2\ell + 1\tau_{\text{had}}$ channel of tHq production, the τ_{had} is produced 83.7% of
 2616 times as a product of the Higgs-boson decay in opposition to the 16% in
 2617 which it comes from the top-quark disintegration.

2618 **Opposite-sign Leptons**

2619 In the dominant scenario (τ_{had} from Higgs) the association of which light-
 2620 flavoured lepton comes from the top-quark decay and which one comes
 2621 from the Higgs-boson decay can be done directly if these two leptons have
 2622 opposite electric charge, i.e. in the $2\ell \text{OS} + 1\tau_{\text{had}}$ channel. Since in Higgs
 2623 boson is neutrally charged, the sum of the charge of its decay products
 2624 should be zero. Therefore, in the OS channel, while the light lepton with
 2625 opposite charge to that of the τ_{had} is the one coming from the Higgs, the
 2626 other lepton, i.e. the one with the same charge as τ_{had} , is the one originated
 2627 from the top-quark decay.

2628 **Same-sign Leptons**

2629 In contrast to the the $2\ell \text{OS} + 1\tau_{\text{had}}$ channel, in the case of τ_{had} from Higgs,
 2630 when the two light leptons have the same electric charge (the so called
 2631 $2\ell \text{SS} + 1\tau_{\text{had}}$) it is not possible to know, a priori, which of the leptons
 2632 comes from the top-quark system and which from the Higgs-boson decay.

2633 In order to perform this association for the $2\ell \text{SS} + 1\tau_{\text{had}}$ several methods
 2634 relying in the truth-level information have been tested. **Describir superficialmente los métodos listados en el ítemize**

- 2636 • First method (Cyrus): Assume that the leading lepton was originated
 2637 from the top
- 2638 • Second method (Mathias): Cut in two variables

- 2639 – Cut 1: $m_{vis,H}(lep(t)) - m_{vis,H}(lep(H)) > 57.0 \text{ GeV}$
 2640 – Cut 2: $m_{pred,t}(lep(H)) - m_{pred,t}(lep(t)) > 0.0 \text{ GeV}$
- 2641 • BDT based method presented in this work

2642 **5.4.3.1 Labelling the $2\ell \text{ SS} + 1\tau_{\text{had}}$ with the reconstruction-level**
 2643 **and truth-level matching**

2644 Even though at reconstruction level it is not known which are the par-
 2645 ents of the particles in the final state, at parton level this informations is
 2646 accesible, in other words, the origin¹ of the light leptons is known. For a
 2647 given event, it is possible to access to both the particle-level and parton-level
 2648 information simultaneously. Having the parton-level leptons, whose parents
 2649 are known, and the reconstruction level leptons, whose parents need to be
 2650 identified, it is possible to compare them to create an association. Specific-
 2651 ally, identify which parton-level lepton correspond to which reconstructed
 2652 lepton. The aim of this relation is to assign the leading (ℓ_1) and sub-leading
 2653 (ℓ_2) light leptons at reconstruction level to the the “lepton from top-quark-
 2654 decay chain” (ℓ_{top}) and “lepton from Higgs-boson-decay chain” (ℓ_{Higgs}) at
 2655 truth level.

2656 In order to link the reconstruction-level light leptons to the parton-level
 2657 light leptons, a $\Delta R < 0.01$ cone around each of the reconstructed leptons
 2658 is built. When inside that cone there one and only one truth-level light
 2659 lepton, there is what is called “a match”. Figure 5.1 presents the possibles
 2660 scenarios of the association. In order to identify properly determine the
 2661 lepton origin in an event, it is required that both leptons at reconstruction
 2662 level have a match. There are two different cases for this. The first situation
 2663 is that in which the leading-light lepton is ℓ_{top} and the sub-leading is ℓ_{Higgs} .
 2664 For the sake of simplicity, this configuration is named Type 1 and it is
 2665 represented in Figure 5.1a. The second double-matching combination is the
 2666 other way around, the leading-light lepton is ℓ_{Higgs} and the sub-leading is
 2667 ℓ_{top} . Pictured in Figure 5.1b, this type of events are called Type 2. On
 2668 the contrary, if only one of the two reconstructed light leptons is matched
 2669 (Figure 5.1c), none of the leptons are classified. If a less strict criteria was
 2670 used, it would be possible requiere only one of the two leptons matching in
 2671 order to classify the event (the unmatched reconstruction-level lepton would
 2672 be assigned to the unmatched parton-level lepton). The problem of the lax
 2673 strategy is that while in cases like that on Figure 5.1c it seems clear that
 2674 unmatched parton correspond to the unmatched reconstructed lepton, for

¹By origin of a light lepton is meant whether it comes from the Higgs-boson-decay chain or the top-quark-decay chain.

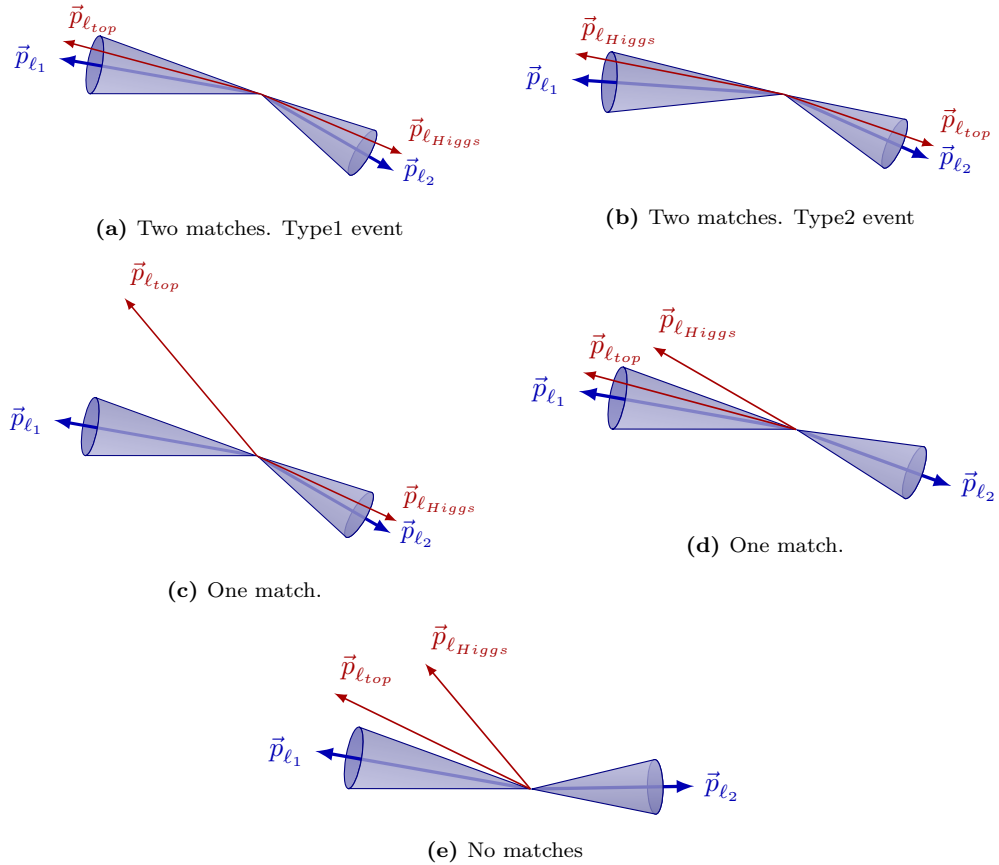


Figure 5.1: Association between reconstruction-level (blue) and parton-level (red) light leptons. Note that the labels ℓ_{top} and ℓ_{Higgs} are only available for the parton-level particles.

events such as the illustrated in Figure 5.1d the unmatched particle does not necessarily belong to the ℓ_2 cone. For this reason, it is mandatory that both reconstructed light leptons have a match. Finally, in the scenario in which none of the parton-level leptons fall into the cones (Figure 5.1e), no assignation takes place.

To perform this labelling, it has been required that the τ_{had} is originated in from the Higgs-boson system. This is imposed in order to guarantee that there are both a ℓ_{top} and a ℓ_{Higgs} . The Higgs-decay channels used for these studies are the $H \rightarrow \tau\tau$ (one τ decaying leptonically and the other hadronically) and the $H \rightarrow WW$. The $H \rightarrow ZZ$ channel has not been included since its impact in the on the $2\ell + 1\tau_{had}$ production when the τ_{had} comes from the Higgs is very tiny. If the τ_{had} is originated in the Higgs system, only a 2.0% of the events correspond to the $H \rightarrow ZZ$ decay channel, contrasting with the 76.5% of the $H \rightarrow \tau\tau$ and the 21.5% of the $H \rightarrow WW$.

2689 **Should add the fraction of events that are labeled from a) the**
2690 **total $2\ell + 1\tau_{\text{had}}$ sample and b) from the total $2\ell \text{SS} + 1\tau_{\text{had}}$.**

2691 **5.4.3.2 BDT-based method for lepton association**

- 2692 • Describe the idea of using reco-level variables to predict (on unlabelled
2693 data) whether it is a Type1 or Type2 event by means of a BDT trained
2694 with labeled data (isLep1fromTop)
- 2695 • Describe with a few words what a BDT is and reference appendix B.
- 2696 • Using root.TMVA - Advantages: Nowadays most of ML frameworks
2697 (keras, pyTorch, scikit-learn, XGBoost, etc..) are based on python.
2698 These libraries expect numpy arrays or panda data-frames as input, so
2699 the first thing to do when using the analysis NTuples is to convert the
2700 ROOT data-frame. An advantage of using TMVA library of ROOT
2701 is that this data conversion is not necessary. is that
- 2702 • Describe the particularities of this gradient BDT with detail
 - 2703 – Programmed in an external-to-tHqLoop script
 - 2704 – Trained only over SS signal events. In contrast to the BDT of
2705 SR that trains over all process, this one trains only over signal
2706 because its objective is to determine which lepton comes from
2707 which particle in the signal events and this classification only
2708 makes sense in signal processes.
- 2709 • Present the feature importance
 - 2710 – Present distributions of used variables and a list with the mean-
2711 ing of this variables
 - 2712 – Present correlations between pairs of used variables. Note that
2713 the correlation maps search for bidimensional correlations (i.e.
2714 between pairs of two variables) and the BDT uses N-dimensional
2715 relations. (Page 26 of the TMVA guide)
- 2716 –
- 2717 • Discuss the negative weight strategy: Present used distributions with
2718 'all weights' and with 'positive weights'
- 2719 • Hyperparameter optimisation
- 2720 • Present BDT response, ROC curve, something else?
- 2721 • Compare to the results using other MVA methods.

- 2722 • The BDT is integrated in tHqLoop (weights.xml) ¿Where do I describe
 2723 what tHqLoop is?
- 2724 • From tHqLoop, the BTD score can be calculated for all the events
 2725 (signal or not) and then the efficiency of the lepton association can be
 2726 calculated depending on the threshold point which is chosen to define
 2727 whether the event is Type1 or Type2. Note that this efficiency is
 2728 computed only over signal events. → Table of 'efficiency vs cutpoint'

2729 **5.4.4 Top quark and Higgs boson reconstruction**

2730 **En aras de que esto es extremadamente complicado y no se**
 2731 **logró hacer ¿tiene sentido redactar una sección?**

2732 **5.5 Background estimation**

2733 The background can be defined as everything in a subset of the data that
 2734 simulates the signal processes without truly being a signal event. In other
 2735 words, in this studies, everything that is not signal, is background. In this
 2736 case, whatever that mimics the signature of an associated tHq production
 2737 with $2\ell + 1\tau_{\text{had}}$ final state is re referred as background.

2738 Signal (aka needle). -> Several needels Background (aka haystack) ->
 2739 Several types of haystacks

2740 The main source of background in the $2\ell + 1\tau_{\text{had}}$ channel is due to jets
 2741 faking τ_{had} **poner las figuras de oleh**

2742 **5.5.1 Fakes estimation**

2743 tau fakes are more important than light lepton fakes

2744 **This is taken from the intNote. I have to reorganise and rephrase this information** The requirements for the objets defined in section
 2745 (ref ref) provide significant suppression of events with jets wrongly selected
 2746 as leptons is achieved by asking electrons and muons to pass the tight
 2747 requirement that combines **tightLH** ID for leptons and **medium** for muons
 2748 and **PLImprovedTight** isolation working points

2750 Similarly, the hadronic taus are required to pass the **medium** requirement
 2751 of the RNN-based discriminator. Even so, the selected data sample
 2752 is expected to be contaminated with such type of reducible background. It

2753 is also expected that the simulation of jets faking leptons (electron, muon,
2754 hadronic tau) in ATLAS detector is imprecise or unreliable. Therefore, an
2755 important step of the analysis is to estimate this background in data.

2756 **Light lepton fakes** Particles in the Feynman diagram are referred as
2757 ‘prompt’ or ‘real’. Acceptance, quality and isolation requirements are ap-
2758 plied to select these leptons Non-prompt leptons and non-leptonic particles
2759 may satisfy these selection criteria, giving rise to so called ‘non-prompt and
2760 fake’ lepton backgrounds. Fake electrons/muons will not be explicitly dis-
2761 tinguished and are referred as fake leptons. The mis-identified lepton back-
2762 ground arises from heavy-flavour (HF) decay leptons and electrons from
2763 γ -conversions. These leptons are mainly produced in $t\bar{t}$, $Z + \text{jets}$ and tW
2764 events.

2765 The estimation of the fake/non-prompt lepton background is done with
2766 the template fit method or via the matrix method

2767 The fake and real lepton efficiencies (fake/real rates) are defined as the
2768 probabilities of a fake or real electron or muon to pass the nominal elec-
2769 tron/muon requirements. They are given by the tight over loose ratio

2770 - Get some ideas from here: [https://cds.cern.ch/record/1951336/
2771 files/ATLAS-CONF-2014-058.pdf](https://cds.cern.ch/record/1951336/files/ATLAS-CONF-2014-058.pdf)

2772 **Tau fakes** In the analysis channels involving hadronic taus, all meth-
2773 ods used for fake background estimation rely on MC-based templates.
2774 These are splits of simulation according to a type of object mimicking the
2775 lepton of interest. Construction of MC templates related to the electron
2776 and muon fakes is based on IFFTruthClassifier tool. [Describe the
2777 IFFTruthClassifier](#)

- 2778 • counting method
2779 • template fit method

2780 The extracted SFs are then applied to the simulated background com-
2781 ponent in the region with taus passing I

2782 5.5.2 Prompt backgrounds

2783 All the processes whose signature is the same as the process of interest
2784 are known as prompt backgrounds as in contrast to the fake or non-prompt
2785 backgrounds described in Section 5.5.1.

Process	SS	OS	SS + OS
tHq	0.9	1.2	2.1
tZq	6.2	32.9	39.1
$t\bar{t}$	47.9	2965.0	3012.9
tW	2.3	118.9	121.2
$W + \text{jets}$	1.9	0.5	2.4
$Z + \text{jets}$	6.7	1956.2	1962.9
diboson	8.9	121.6	130.5
$t\bar{t}W$	21.0	43.4	64.4
$t\bar{t}Z$	17.5	101.2	118.7
$t\bar{t}H$	17.8	43.2	61.0
tWZ	3.1	16.4	19.5
tWH	0.6	1.5	2.1
Other	1.9	9.3	11.2
Total	136.7	5411.3	5548.0
S/B (%)	0.6627	0.0222	0.0379
Significance	0.0771	0.0163	0.0282

Table 5.2: Event yields at preselection level for SS, OS and SS+OS combination.

2786 5.6 Event selection

2787 5.6.1 Preselection

2788 Preselection requirements

2789 5.6.2 BDT

2790 Since a BDT is going to be used for both the lepton assign-
 2791 ment al region definition, it may be interesting to describe the
 2792 technicalities of the BDT in an appendix

2793 Maybe, it can also be a good idea to explain the generalities of
 2794 the BDT for region definition here and then put the BDT results
 2795 into "Signal Region" and "Control Regions" section.

2796 **5.6.2.1 Performance**

2797 **5.6.2.2 Ranking of variables**

2798 **5.6.2.3 Hyperparameter optimisation**

2799 **Grid search**

2800 **Genetic algorithm**

2801 **5.6.2.4 Negative-weights strategy**

2802 **5.6.2.5 k-Folding**

2803 **5.6.3 Signal Region**

2804 **5.6.3.1 Same Sign channel**

2805 **5.6.3.2 Oposite Sign channel**

2806 **5.6.4 Control Regions**

2807 **5.6.4.1 Same Sign channel**

2808 $t\bar{t}$

2809 $t\bar{t}W$

2810 $t\bar{t}Z$

2811 $t\bar{t}H$

2812 **5.6.4.2 Oposite Sign channel**

2813 $t\bar{t}$

2814 $Z +\text{jets}$

2815 **Diboson**

2816 **tW**

2817 5.7 Systematic uncertainties

2818 Particle collision physics distinguish two types of uncertainties, the stat-
2819 istical uncertainty and the systematic uncertainty. The statistical uncer-
2820 tainty is the result of stochastic fluctuations in data and is the result of a
2821 limited size of analysed dataset. It is fully uncorrelated between subsequent
2822 measurements. On the other hand there are the systematic uncertainties,
2823 which are defined as everything that is not a statistical error. These are
2824 fully correlated between subsequent measurements and are associated with
2825 all sort of sources such us the measurement apparatus, the assumptions
2826 made, the model used, the MC generator and many others.

2827 While the statistical uncertainty is usually intrinsically added in the
2828 inference method, the inclusion of the systematic uncertainties and its
2829 propagation through the statistical analysis are not trivial.

2830 Alternative samples are produced to evaluate the systematics: - Herwig⁷
2831 -> parton shower
2832 - asdfas. -> modelling

2833

2834 5.7.1 Theoretical uncertainties

2835 5.7.2 Modelling uncertainties

2836 5.7.3 Experimental uncertainties

2837 5.8 Fit results

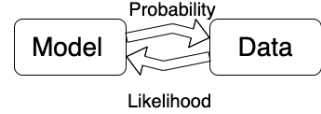
2838 5.8.1 Likelihood fit

2839 **Maybe I move the statistics description to an appendix** The
2840 likelihood fit....

2841 The likelihood function is defined as the probability of observing a cer-
 2842 tain set of data (\vec{x}) given a model or hypothesis with certain parameter
 2843 values ($\vec{\theta}$). It is given by

2844

$$L(\vec{\theta}) = \mathcal{P}(\vec{x}|\vec{\theta}) = \prod_i \mathcal{P}(x_i|\vec{\theta})$$



2845 where i runs over the data points. By maximising the likelihood func-
 2846 tion, the parameters $\vec{\theta}$ of the model that better fit the data are obtained.
 2847 These are known as estimated values. The fit is the parameter estimation
 2848 via the Likelihood maximisation, $\vec{\theta}_{estimated} = \text{argmax}_{\vec{\theta}} L(\vec{\theta})$.

For binned distributions the likelihood function can be written as

$$L(\vec{n}|\vec{\theta}) = \prod_{i \in bins} \mathcal{P}(n_i^{obs}|n_i^{exp}(\vec{\theta})) = \prod_{i \in bins} \mathcal{P}(n_i^{obs}|S_i^{exp}(\vec{\theta}) + B_i^{exp}(\vec{\theta}))$$

2849 Here, i runs over the bins of the histogram, n_i^{obs} and n_i^{exp} are the observed
 2850 and expected number of entries in the bin i . The predicted signal and
 2851 background entries in the bin i are S_i and B_i .

2852 Since particle physics experiments are counting experiments, the dis-
 2853 tribution follows the poissonian statistics. The Poisson distribution is a
 2854 discrete probability distribution that expresses the probability of a given
 2855 number of events occurring in a fixed interval of time or space if these
 2856 events occur with a known constant mean rate and independently of the
 2857 time since the last event

From the frequentist point of view the probability is defined as the fraction of times an event occurs, in the limit of very large number ($N \rightarrow \infty$) of repeated trials

$$\mathcal{P} = \lim_{N \rightarrow \infty} \frac{\text{Number of favorable cases}}{N}$$

2858 where N is the number of trials. Even though this infinity can be concep-
 2859 tually unpleasant, for LHC experiments, the amount of events is so large
 2860 that this \mathcal{P} definition becomes acceptable [183].

2861 Meanwhile, for the Bayesian (or subjective) probability expresses the
 2862 degree of belief that a claim is true. Starting from a prior probability,
 2863 following some observation, the probability can be modified into a posterior
 2864 probability. The more information an individual receives, the more Bayesian
 2865 probability is insensitive on prior probability [183].

The Bayes theorem states that considering two events A and B , the probability of A to happen given that B takes places is

$$\mathcal{P}(A|B) = \frac{\mathcal{P}(B|A)\mathcal{P}(A)}{\mathcal{P}(B)}$$

2866 where $\mathcal{P}(B|A)$ is the conditional probability of B given A and $\mathcal{P}(B)$ the
2867 probability of the event B to happen. Here, $\mathcal{P}(A)$ has the role of prior
2868 probability while $\mathcal{P}(A|B)$ is known as posterior probability.

2869 **5.8.2 Strategy**

2870 **5.8.3 Fit with Asimov data**

2871 **5.8.3.1 Post-fit**

2872 **5.8.3.2 Pruning**

2873 **5.8.3.3 Nuisance Parameters**

2874 **5.8.3.4 Correlation matrix**

2875 **5.8.3.5 Ranking**

2876 **5.8.4 Fit to data**

2877 **5.8.4.1 Post-fit**

2878 **5.8.4.2 Pruning**

2879 **5.8.4.3 Nuisance Parameters**

2880 **5.8.4.4 Correlation matrix**

2881 **5.8.4.5 Ranking**

2882 **5.8.5 Results**

2883 **5.8.6 Data fit**

2884 **5.9 Combination results**

2885 **Discuss results, compare them with CMS, future perspectives**

2886 **...**

2887 **5.10 Conclusions**

²⁸⁸⁸ Chapter 6

²⁸⁸⁹ Conclusion

2890 **Appendix A**

2891 **Effect of negative weights**

2892 **A.1 Negative weights uncertainties**

- 2893 • What is a weight in a MC event?
- 2894 • Why are there negatively weighted events?
- 2895 • Why are negative weights problematic?

2896 **A.2 Statistical uncertainty of negative
2897 weights**

2898 Assume that there is a sample of N Monte Carlo simulated events. Of
2899 these, a fraction x have negative weights and, therefore, a fraction $(1 - x)$
2900 has a positive weight. The effective number of events is $(N_+ - N_-)$, being
2901 $N_+ = (1 - x)N$ the amount of positively weighted events and $N_- = xN$ the
2902 same for the negative weights.

2903 The statistical fluctuations are calculated in terms of x and the standard
2904 deviation ($\sigma_N = \sqrt{N}$). The number of positive and negative events can
2905 fluctuate randomly between $\pm\sigma_-$ for the later and $\pm\sigma_+$ for the former.
2906 Here, $\sigma_- = \sqrt{xN} = \sqrt{x}N$ and $\sigma_+ = \sqrt{1-x}N$

The variance ($V = \sigma^2$) of the sample is then

$$V(N_+ - N_-) = xV(N) + (1 - x)V(N) = V(N)$$

and the fractional uncertainty

$$\frac{\sigma(N_+ - N_-)}{N_+ - N_-} = \frac{\sigma_N}{(1 - x)N - xN} = \frac{1}{1 - 2x} \frac{\sigma_n}{N}$$

- 2907 When the fraction of negative events is $x = 0$, $\frac{\sigma(N_+ - N_-)}{N_+ - N_-} = \frac{\sigma_n}{N}$ as expected.
 2908 In contrast, if $x = 0.5$ the fractional uncertainty is infinite, as expected.

2909 For the signal tHq $2\ell + 1\tau_{\text{had}}$ MC signal sample the fraction of negative
 2910 weights is between 0.3 and 0.4 depending on the production used.

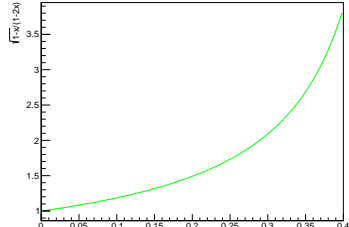
$$2911 \quad \bullet \quad x = 0.3 \rightarrow \frac{\sigma(N_+ - N_-)}{N_+ - N_-} = \frac{1}{0.2} \frac{\sigma_n}{N} = 5.0 \frac{\sigma_n}{N}$$

$$2912 \quad \bullet \quad x = 0.4 \rightarrow \frac{\sigma(N_+ - N_-)}{N_+ - N_-} = \frac{1}{0.4} \frac{\sigma_n}{N} = 2.5 \frac{\sigma_n}{N}$$

2913 The uncertainty of the effective number of events can be compared to
 2914 that of using only the positively weighted events. If the two fractional
 2915 uncertainties are divided:

$$\frac{\frac{\sigma(N_+ - N_-)}{N_+ - N_-}}{\frac{\sigma(N_+)}{N_x}} = \frac{\frac{1}{1-2x} \frac{\sigma_n}{N}}{\frac{1}{\sqrt{(1-x)N}}} = \frac{\sqrt{1-x} \sigma_n}{1-2x} \frac{1}{N} = \frac{\sqrt{1-x}}{1-2x}$$

2916 In the range of x values for the $2\ell + 1\tau_{\text{had}}$ simulated signal events.



$$2917 \quad \bullet \quad x = 0.3 \rightarrow \frac{\frac{\sigma(N_+ - N_-)}{N_+ - N_-}}{\frac{\sigma(N_+)}{N_x}} = 3.9$$

$$\bullet \quad x = 0.4 \rightarrow \frac{\frac{\sigma(N_+ - N_-)}{N_+ - N_-}}{\frac{\sigma(N_+)}{N_x}} = 2.1$$

2918 In Figure A.1, several ΔR distributions generated using all the events
 2919 and just the positively weighted ones. As expected, the uncertainty bands
 2920 are bigger for the 'All events' than for the 'Positive events'. These his-
 2921 tograms were produced to verify that using only the events with positive
 2922 weights in the training of the BDT for lepton assignment in the SS scenario
 2923 (Section 5.4.3) was not biasing the result. The size of the error bands is
 2924 calculated by ROOT as the square root of the quadratic sum of the weights,
 2925 as explained below.

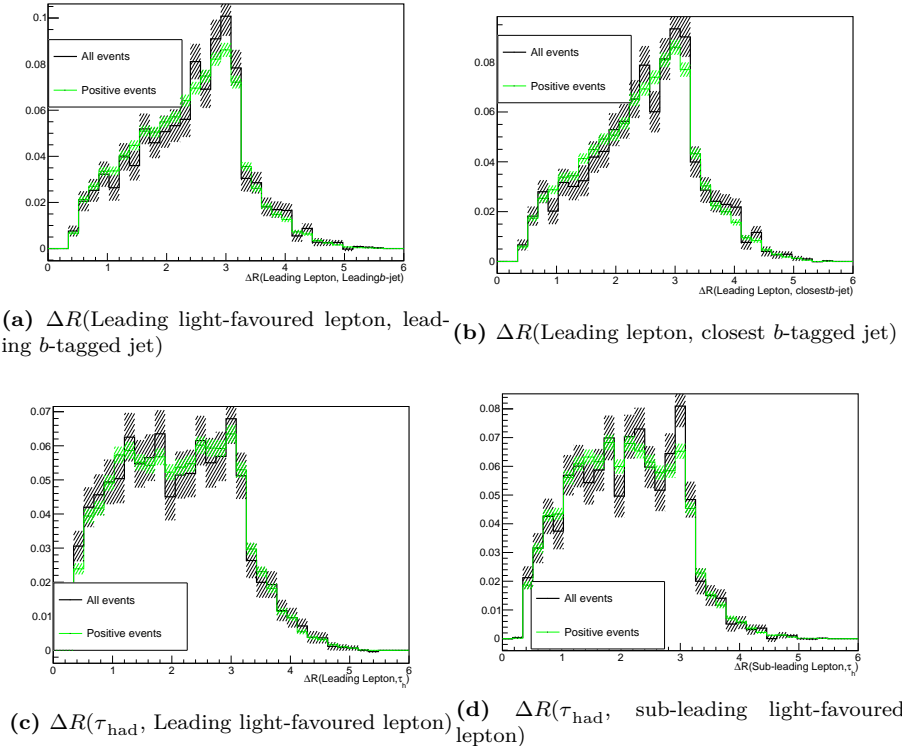


Figure A.1: Some normalised distributions for all the signal events in the $2\ell \text{SS} + 1\tau_{\text{had}}$ (black) and just the positively weighted events (green). For each bin, the error band is calculated as the square root of the quadratic sum of the weights.

2926 A.2.1 Errors in binned histograms

If a bin of a histogram has n entries of weighted events w_i with $i = 1, 2, \dots, n$, the size of the bar is $\sum_{i=1}^n w_i$. Therefore, the error of that bar is

$$\sqrt{\sum_{i=1}^n w_i^2} \quad (\text{A.1})$$

This expression for the error of a bin in a histogram is based on error propagation and intrinsic poissonian statistics only. The variance, i.e. the error on the weighted number of events" in that bin, is given by error propagation:

$$V\left(\sum_{i=1}^n w_i\right) = \sqrt{\left(\sum_{i=1}^n w_i^2\right)^2} = \sum_{i=1}^n w_i^2 = \sum_{i=1}^n V(w_i)$$

2927 The variance of the weight w_i , $V(w_i)$, is determined only by the statistical
2928 fluctuation of the number of events considered: $V(w_i) = w_i^2$.

2929 A.3 Negative weights in MVA methods

2930 Events coming from the MC generator can be produced with (unphys-
2931 ical) negative weights in some phase-space regions. Such occurrences are
2932 frequently inconvenient to deal with, and whether or not they are handled ef-
2933 fectively is dependent on the MVA method's actual implementation. Within
2934 the ROOT TMVA library, probability and multi-dimensional probability
2935 density estimators, as well as BDTs, are among the methods that correctly
2936 include occurrences with negative weights. In cases where a method does
2937 not properly treat events with negative weights, it is advisable to ignore such
2938 events for the training but to include them in the performance evaluation
2939 to not bias the results.

2940 **Appendix B**

2941 **Boosted Decision Tree**

2942 **B.1 Intro**

2943 Paragraphs of section intro

- 2944 • What is Machine Learning and an MVA method
- 2945 • what is a BDT
- 2946 • Uses of the BDT in this thesis: Two different libraries for TMVA
2947 ROOT and XGBoost. For XGBoost we have to convert the data to
2948 `pandas`?`numpy`?
- 2949 • BDT in comparison to NN

2950 **B.2 How does a BDT work**

2951 **B.2.1 Training**

2952 **B.2.2 Evaluation**

2953 Sometimes, MC generators may provide event weights which may turn
2954 out to be extremely small or very high. To avoid artefacts, TMVA can
2955 renormalise the signal and background training weights internally so that
2956 their respective sums of effective (weighted) events are equal. By doing
2957 this, the performance of the BDT can be improved since some classifiers
2958 are sensitive to the relative amount of each category (Type1/Type2 or sig-
2959 nal/background) in the training data. While for the lepton assignment this

2960 renormalisation does not play an important role (the amount of Type1 and
 2961 Type2 signal events is similar), for the the tHq signal discrimination the
 2962 signal sample in the training test has to be reweighted.

2963 B.2.3 Overtraining

2964 Overtraining occurs when a ML model can accurately predict training
 2965 examples but is unable to generalise¹ to new data. When overtraining takes
 2966 place, the ML model has learnt the details of the training data to an extent
 2967 in which these knowledge do not reflect the behaviour of the test sample.
 2968 This results in poor field performance.

2969 When tested on the training sample, overtraining results in an apparent
 2970 improvement in classification or regression performance over the objectively
 2971 achievable one, but an effective performance loss when measured on an
 2972 independent test sample (even though, there is a risk that it can still happen
 2973 even if we use separate test data). Until deployed to real unseen data, there
 2974 is a danger that overtraining will go unnoticed. This makes of overtraining
 2975 one of the greatest dangers in ML. Other names for this phenomenon are
 2976 overfitting and type III error.

2977 Usually, this is a result of too little data or data that is too homogenous.
 2978 Overtraining arises when there are too few degrees of freedom, because too
 2979 many model parameters of an algorithm were adjusted to too few data
 2980 points. Not all MVA methods are equally sensible to overtraining. While
 2981 Fisher discriminant hardly suffers from it, BDTs usually suffer from at least
 2982 partial overtraining, owing to their large number of nodes. Nevertheless,
 2983 for the BDTs some countermeasures can be applied to preserve the ability
 2984 to generalise:

- 2985 • Never test the model on the data used for the training.
- 2986 • The number of nodes in boosted decision trees can be reduced by
 2987 removing insignificant ones (“tree pruning”). There are two types, pre-
 2988 pruning and post-pruning
 - 2989 – Pre-pruning: Refers to the early stopping of the growth of the
 2990 decision tree
 - 2991 – Post-pruning: Allows the decision tree model to grow to its full
 2992 depth, then removes the tree branches to prevent the model from
 2993 overfitting

¹By generalise is meant that the model recognises only those characteristics of the data that are general enough to also apply to some unseen data.

- 2994 • Cross validation is a powerful technique to use all the data for training
2995 at the same time that all the data for testing is employed while
2996 avoiding overfitting. This method is based in cleverly iterating the
2997 test and training split around and it is described in Section B.4.

2998 **B.2.4 Application**

2999 **B.3 Treatment of negative weights**

3000 **B.4 Cross validation and k -folding**

3001 The goal of cross validation is to estimate the performance of a machine
3002 learning model.

3003 Abbreviations

3004

Acronym	Meaning
AD	Antiproton Decelerator
ALICE	A Large Ion Collider Experiment
ATLAS	A Toroidal LArge AparatuS
AWAKE	Advanced Proton Driven Plasma Wakefield Acceleration Experiment
CERN	European Organization for Nuclear Research
CMS	Compact Muon Solenoid
CP	Charge conjugation Parity
CSC	Cathode-Strip Chambers
DAQ	Data Acquisition
ECAL	Electromagnetic Calorimeter
EF	Event Filter
EM	Electromagnetic
EW	Electro Weak
EWSB	Electroweak Symmetry Breaking
FASER	ForwArd Search ExpeRiment
FCAL	Forward calorimeter
FTK	Fast TracKer
GR	General Relativity
HCAL	Hadronic Calorimeter
HLT	High Level Trigger
IBL	Insertable B-Layer
IP	Interaction Point

Acronym	Meaning
IR	Insertion Regions
ISOLDE	On-Line Isotope Mass Separator
ITk	Inner Tracker
LAr	Liquid Argon
LCG	LHC Computing Grid
LEIR	Low Energy Ion Ring
LEP	Large Electron-Positron
LHC	Large Hadron Collider
LHCb	The Large Hadron Collider Beauty
LHCf	Large Hadron Collider forward
LINAC2	Linear Accelerator 2
LINAC3	Linear Accelerator 3
LINAC4	Linear Accelerator 4
3005	LO
	Leading Order
	LVL1
	Level-1 Trigger
	LVL2
	Level-2 Trigger
MATHUSLA	Massive Timing Hodoscope for Ultra Stable neutrAL pArticles
MDT	Monitored Drift Tube
MoEDAL	Monopole and exotic particle detector at the LHC
MS	Muon Spectrometer
NLO	Next-to-Leading Order
NNLO	Next-to-Next-to-Leading Order
PDF	Parton Distribution Function
PS	Proton Synchrotron
PSB	Proton Synchrotron Booster
QCD	Quantum Chromodynamics
QED	Quantum Electrodynamics
QFT	Quantum Field Theory

3006

Acronym	Meaning
RF	Radio Frequency
ROD	ReadOut Drivers
RoI	Regions of interest
ROS	ReadOut Systems
RPC	Resistive Plate Chambers
SCT	Semiconductor Tracker
SFO	Sub-Farm Output
SM	Standar Model
SPS	Super Proton Synchrotron
SSB	Spontaneus Symmetry Breakin
SSC	Superconducting Super Collider
SUSY	Supersimmetry
TGC	Thin Gap Chambers
TI	Transfer Injection

³⁰⁰⁷ Bibliography

- ³⁰⁰⁸ ¹Particle Data Group Web Page, *top-quark Mass (Direct Measurements)*,
³⁰⁰⁹ (2022) <https://pdglive.lbl.gov/DataBlock.action?node=Q007TP>
³⁰¹⁰ (visited on 22/01/2022) (cit. on pp. v, 34).
- ³⁰¹¹ ²Particle Data Group Web Page, *Higgs-boson Mass*, (2022)
³⁰¹² <https://pdglive.lbl.gov/DataBlock.action?node=S126M> (visited
³⁰¹³ on 22/01/2022) (cit. on pp. v, 46).
- ³⁰¹⁴ ³Online Etymology Dictionary, "Physics", (2022)
³⁰¹⁵ <https://www.etymonline.com/word/physics> (visited on 20/01/2022)
³⁰¹⁶ (cit. on p. 1).
- ³⁰¹⁷ ⁴Perseus Digital Library, "fusiko", (2022)
³⁰¹⁸ <https://www.perseus.tufts.edu/hopper/text?doc=Perseus:text:1999.04.0057:entry=fusiko/s> (visited on 20/01/2022) (cit. on p. 1).
- ³⁰²⁰ ⁵C Singer, *A Short History of Science to the Nineteenth Century*, p. 35.
³⁰²¹ (Streeter Press, 2008) (cit. on p. 1).
- ³⁰²² ⁶C. C. W. Taylor et al., *The atomists, leucippus and democritus: fragments: a text and translation with a commentary*, Vol. 5
³⁰²³ (University of Toronto Press, 2010) (cit. on p. 1).
- ³⁰²⁵ ⁷O. Leaman, *Key concepts in eastern philosophy* (Routledge, 2002)
³⁰²⁶ (cit. on p. 1).
- ³⁰²⁷ ⁸A. Einstein, *The Foundation of the General Theory of Relativity*,
³⁰²⁸ *Annalen Phys.* **49** (1916) 769–822, edited by J.-P. Hsu and D. Fine
³⁰²⁹ (1916) (cit. on p. 2).
- ³⁰³⁰ ⁹P. A. M. Dirac, *On the theory of quantum mechanics*,
³⁰³¹ Proceedings of the Royal Society of London. Series A, Containing
³⁰³² Papers of a Mathematical and Physical Character **112** (1926) 661–677
³⁰³³ (1926) (cit. on p. 3).
- ³⁰³⁴ ¹⁰R. Aaij et al., *Observation of a narrow pentaquark state, $P_c(4312)^+$, and*
³⁰³⁵ *of two-peak structure of the $P_c(4450)^+$,*
³⁰³⁶ *Phys. Rev. Lett.* **122** (2019) 222001 (2019) (cit. on p. 4).

- ³⁰³⁷¹¹A. Pich, ‘The Standard model of electroweak interactions’,
 3038 2006 European School of High-Energy Physics (2007) 1
 3039 (cit. on pp. 4, 16).
- ³⁰⁴⁰¹²E. Noether, *Invariante variationsprobleme*, ger,
 3041 Nachrichten von der Gesellschaft der Wissenschaften zu Göttingen,
 3042 Mathematisch-Physikalische Klasse **1918** (1918) 235–257 (1918)
 3043 (cit. on p. 6).
- ³⁰⁴⁴¹³C. A. Moura and F. Rossi-Torres, *Searches for Violation of CPT Symmetry and Lorentz Invariance with Astrophysical Neutrinos*,
 3045 *Universe* **8** (2022) 42 (2022) (cit. on p. 9).
- ³⁰⁴⁷¹⁴J. S. Bell, *Time reversal in field theory*,
 3048 *Proc. Roy. Soc. Lond. A* **231** (1955) 479–495 (1955) (cit. on p. 9).
- ³⁰⁴⁹¹⁵R. F. Streater and A. S. Wightman,
 3050 *PCT, spin and statistics, and all that* (1989) (cit. on p. 9).
- ³⁰⁵¹¹⁶T. D. Lee and C.-N. Yang,
 3052 *Question of Parity Conservation in Weak Interactions*,
 3053 *Phys. Rev.* **104** (1956) 254–258 (1956) (cit. on p. 9).
- ³⁰⁵⁴¹⁷C. S. Wu, E. Ambler, R. W. Hayward, D. D. Hoppes and R. P. Hudson,
 3055 *Experimental Test of Parity Conservation in β Decay*,
 3056 *Phys. Rev.* **105** (1957) 1413–1414 (1957) (cit. on p. 9).
- ³⁰⁵⁷¹⁸R. L. Garwin, L. M. Lederman and M. Weinrich,
 3058 *Observations of the failure of conservation of parity and charge*
 3059 *conjugation in meson decays: the magnetic moment of the free muon*,
 3060 *Phys. Rev.* **105** (4 1957) 1415–1417 (1957) (cit. on p. 10).
- ³⁰⁶¹¹⁹J. H. Christenson, J. W. Cronin, V. L. Fitch and R. Turlay,
 3062 *Evidence for the 2π Decay of the K_2^0 Meson*,
 3063 *Phys. Rev. Lett.* **13** (1964) 138–140 (1964) (cit. on p. 10).
- ³⁰⁶⁴²⁰L.-L. Chau and W.-Y. Keung,
 3065 *Comments on the Parametrization of the Kobayashi-Maskawa Matrix*,
 3066 *Phys. Rev. Lett.* **53** (1984) 1802 (1984) (cit. on p. 11).
- ³⁰⁶⁷²¹J. Hardy and I. Towner, $|V_{ud}|$ from nuclear β decays,
 3068 *PoS CKM2016* (2017) 028 (2017) (cit. on p. 12).
- ³⁰⁶⁹²²D. Pocanic et al.,
 3070 *Precise measurement of the $\pi^+ \rightarrow \pi^0 e^+ \nu$ branching ratio*,
 3071 *Phys. Rev. Lett.* **93** (2004) 181803 (2004) (cit. on p. 12).
- ³⁰⁷²²³R. E. Shrock and L.-L. Wang,
 3073 *New, generalized cabibbo fit and application to quark mixing angles in*
 3074 *the sequential weinberg-salam model*,
 3075 *Phys. Rev. Lett.* **41** (25 1978) 1692–1695 (1978) (cit. on p. 12).

- ³⁰⁷⁶²⁴N. Cabibbo, E. C. Swallow and R. Winston,
³⁰⁷⁷*Semileptonic hyperon decays and CKM unitarity,*
³⁰⁷⁸*Phys. Rev. Lett.* **92** (2004) 251803 (2004) (cit. on p. 12).
- ³⁰⁷⁹²⁵S. Aoki et al.,
³⁰⁸⁰*FLAG Review 2019: Flavour Lattice Averaging Group (FLAG),*
³⁰⁸¹*Eur. Phys. J. C* **80** (2020) 113 (2020) (cit. on p. 12).
- ³⁰⁸²²⁶J. P. Lees et al.,
³⁰⁸³*Measurement of the $D^0 \rightarrow \pi^- e^+ \nu_e$ differential decay branching fraction*
³⁰⁸⁴*as a function of q^2 and study of form factor parameterizations,*
³⁰⁸⁵*Phys. Rev. D* **91** (2015) 052022 (2015) (cit. on p. 12).
- ³⁰⁸⁶²⁷D. Besson et al., *Improved measurements of D meson semileptonic*
³⁰⁸⁷*decays to π and K mesons*, *Phys. Rev. D* **80** (2009) 032005 (2009)
(cit. on p. 12).
- ³⁰⁸⁹²⁸A. Kayis-Topaksu et al.,
³⁰⁹⁰*Measurement of topological muonic branching ratios of charmed hadrons*
³⁰⁹¹*produced in neutrino-induced charged-current interactions,*
³⁰⁹²*Phys. Lett. B* **626** (2005) 24–34 (2005) (cit. on p. 12).
- ³⁰⁹³²⁹P. del Amo Sanchez et al., *Measurement of the Absolute Branching*
³⁰⁹⁴*Fractions for $D_s^- \rightarrow \ell^- \bar{\nu}_\ell$ and Extraction of the Decay Constant f_{D_s} ,*
³⁰⁹⁵*Phys. Rev. D* **82** (2010) 091103, [Erratum: *Phys. Rev. D* 91, 019901
(2015)] (2010) (cit. on p. 12).
- ³⁰⁹⁷³⁰L. Widhalm et al., *Measurement of $D0 \rightarrow \pi l \nu$ ($Kl \nu$) Form*
³⁰⁹⁸*Factors and Absolute Branching Fractions,*
³⁰⁹⁹*Phys. Rev. Lett.* **97** (2006) 061804 (2006) (cit. on p. 12).
- ³¹⁰⁰³¹Y. S. Amhis et al.,
³¹⁰¹*Averages of b -hadron, c -hadron, and τ -lepton properties as of 2018,*
³¹⁰²*Eur. Phys. J. C* **81** (2021) 226 (2021) (cit. on p. 12).
- ³¹⁰³³²A. Abdesselam et al., *Precise determination of the CKM matrix element*
³¹⁰⁴ *$|V_{cb}|$ with $\bar{B}^0 \rightarrow D^{*+} \ell^- \bar{\nu}_\ell$ decays with hadronic tagging at Belle*, (2017)
³¹⁰⁵ (2017) (cit. on p. 12).
- ³¹⁰⁶³³J. P. Lees et al., *Study of $\bar{B} \rightarrow X_u \ell \bar{\nu}$ decays in $B\bar{B}$ events tagged by a*
³¹⁰⁷*fully reconstructed B -meson decay and determination of $\|V_{ub}\|$,*
³¹⁰⁸*Phys. Rev. D* **86** (2012) 032004 (2012) (cit. on p. 12).
- ³¹⁰⁹³⁴B. Colquhoun, R. J. Dowdall, J. Koponen, C. T. H. Davies and
³¹¹⁰G. P. Lepage,
³¹¹¹ *$B \rightarrow \pi \ell \nu$ at zero recoil from lattice QCD with physical u/d quarks,*
³¹¹²*Phys. Rev. D* **93** (2016) 034502 (2016) (cit. on p. 12).
- ³¹¹³³⁵C. W. Bauer, Z. Ligeti and M. E. Luke,
³¹¹⁴*A Model independent determination of $|V(ub)|$,*
³¹¹⁵*Phys. Lett. B* **479** (2000) 395–401 (2000) (cit. on p. 12).

- ³¹¹⁶³⁶R Aaij et al., *Precision measurement of the B_s^0 - \bar{B}_s^0 oscillation frequency*
³¹¹⁷*with the decay $B_s^0 \rightarrow D_s^- \pi^+$* , *New J. Phys.* **15** (2013) 053021 (2013)
³¹¹⁸(cit. on p. 12).
- ³¹¹⁹³⁷M. Misiak et al.,
³¹²⁰*Updated NNLO QCD predictions for the weak radiative B -meson decays*,
³¹²¹*Phys. Rev. Lett.* **114** (2015) 221801 (2015) (cit. on p. 12).
- ³¹²²³⁸T. A. Aaltonen et al., *Tevatron Combination of Single-Top-Quark Cross*
³¹²³*Sections and Determination of the Magnitude of the*
³¹²⁴*Cabibbo-Kobayashi-Maskawa Matrix Element \mathbf{V}_{tb}* ,
³¹²⁵*Phys. Rev. Lett.* **115** (2015) 152003 (2015) (cit. on p. 12).
- ³¹²⁶³⁹V. Khachatryan et al., *Search for the associated production of a Higgs*
³¹²⁷*boson with a single top quark in proton-proton collisions at $\sqrt{s} = 8$ TeV*,
³¹²⁸*JHEP* **06** (2016) 177 (2016) (cit. on pp. 12, 54).
- ³¹²⁹⁴⁰V. M. Abazov et al., *Precision measurement of the ratio*
³¹³⁰ *$B(t \rightarrow Wb)/B(t \rightarrow Wq)$ and Extraction of V_{tb}* ,
³¹³¹*Phys. Rev. Lett.* **107** (2011) 121802 (2011) (cit. on p. 12).
- ³¹³²⁴¹P. A. Zyla et al., *Review of Particle Physics*,
³¹³³*PTEP* **2020** (2020) 083C01 (2020) (cit. on p. 12).
- ³¹³⁴⁴²P. Q. Hung, *The Weak Eightfold Way: $SU(3)_W$ unification of the*
³¹³⁵*electroweak interactions*, (2021) (2021) (cit. on p. 11).
- ³¹³⁶⁴³A. M. Sirunyan et al.,
³¹³⁷*Measurement of the weak mixing angle using the forward-backward*
³¹³⁸*asymmetry of Drell-Yan events in pp collisions at 8 TeV*,
³¹³⁹*Eur. Phys. J. C* **78** (2018) 701 (2018) (cit. on p. 14).
- ³¹⁴⁰⁴⁴O. W. Greenberg, *Spin and Unitary Spin Independence in a Paraquark*
³¹⁴¹*Model of Baryons and Mesons*, *Phys. Rev. Lett.* **13** (1964) 598–602
³¹⁴²(1964) (cit. on p. 15).
- ³¹⁴³⁴⁵D. D. Ryutov, *Using Plasma Physics to Weigh the Photon*,
³¹⁴⁴*Plasma Phys. Control. Fusion* **49** (2007) B429 (2007) (cit. on p. 19).
- ³¹⁴⁵⁴⁶F. J. Yndurain, *Limits on the mass of the gluon*,
³¹⁴⁶*Phys. Lett. B* **345** (1995) 524–526 (1995) (cit. on p. 19).
- ³¹⁴⁷⁴⁷M. Aaboud et al., *Measurement of the W -boson mass in pp collisions at*
³¹⁴⁸ *$\sqrt{s} = 7$ TeV with the ATLAS detector*,
³¹⁴⁹*Eur. Phys. J. C* **78** (2018) 110, [Erratum: *Eur.Phys.J.C* 78, 898 (2018)]
³¹⁵⁰(2018) (cit. on p. 20).
- ³¹⁵¹⁴⁸G. Abbiendi et al., *Precise determination of the Z resonance parameters*
³¹⁵²*at LEP: 'Zedometry'*, *Eur. Phys. J. C* **19** (2001) 587–651 (2001)
³¹⁵³(cit. on p. 20).

- ⁴⁹J. Goldstone, A. Salam and S. Weinberg, *Broken Symmetries*, Phys. Rev. **127** (1962) 965–970 (1962) (cit. on p. 21).
- ⁵⁰D. M. Webber et al., *Measurement of the Positive Muon Lifetime and Determination of the Fermi Constant to Part-per-Million Precision*, Phys. Rev. Lett. **106** (2011) 041803 (2011) (cit. on p. 26).
- ⁵¹M. Aker et al., *Direct neutrino-mass measurement with sub-electronvolt sensitivity*, Nature Phys. **18** (2022) 160–166 (2022) (cit. on p. 27).
- ⁵²N. Aghanim et al., *Planck 2018 results. VI. Cosmological parameters*, Astron. Astrophys. **641** (2020) A6, [Erratum: Astron. Astrophys. 652, C4 (2021)] (2020) (cit. on p. 29).
- ⁵³V. C. Rubin and W. K. Ford Jr., *Rotation of the Andromeda Nebula from a Spectroscopic Survey of Emission Regions*, Astrophys. J. **159** (1970) 379–403 (1970) (cit. on p. 30).
- ⁵⁴A. N. Taylor, S. Dye, T. J. Broadhurst, N. Benitez and E. van Kampen, *Gravitational lens magnification and the mass of abell 1689*, Astrophys. J. **501** (1998) 539 (1998) (cit. on pp. 30, 33).
- ⁵⁵P. A. R. Ade et al., *Planck 2015 results. XIII. Cosmological parameters*, Astron. Astrophys. **594** (2016) A13 (2016) (cit. on p. 30).
- ⁵⁶S. Amoroso et al., *Strategy for ATLAS top quark mass measurements: 2021-2023*, tech. rep., CERN, 2020 (cit. on pp. 33, 34).
- ⁵⁷M. Aaboud et al., *Measurement of the top quark mass in the $t\bar{t} \rightarrow \text{lepton+jets}$ channel from $\sqrt{s} = 8$ TeV ATLAS data and combination with previous results*, Eur. Phys. J. C **79** (2019) 290 (2019) (cit. on p. 34).
- ⁵⁸A. M. Sirunyan et al., *Measurement of the Jet Mass Distribution and Top Quark Mass in Hadronic Decays of Boosted Top Quarks in pp Collisions at $\sqrt{s} = 13$ TeV*, Phys. Rev. Lett. **124** (2020) 202001 (2020) (cit. on p. 34).
- ⁵⁹*Combination of CDF and D0 results on the mass of the top quark using up 9.7 fb^{-1} at the Tevatron*, (2016) (2016) (cit. on p. 34).
- ⁶⁰M. Kobayashi and T. Maskawa, *CP Violation in the Renormalizable Theory of Weak Interaction*, Prog. Theor. Phys. **49** (1973) 652–657 (1973) (cit. on p. 34).
- ⁶¹J. E. Augustin et al., *Discovery of a Narrow Resonance in e^+e^- Annihilation*, Phys. Rev. Lett. **33** (1974) 1406–1408 (1974) (cit. on p. 34).

- ³¹⁹²⁶²S. W. Herb et al., *Observation of a Dimuon Resonance at 9.5-GeV in*
³¹⁹³*400-GeV Proton-Nucleus Collisions,*
³¹⁹⁴*Phys. Rev. Lett.* **39** (1977) 252–255 (1977) (cit. on p. 34).
- ³¹⁹⁵⁶³F. Abe et al., *Observation of top quark production in $\bar{p}p$ collisions,*
³¹⁹⁶*Phys. Rev. Lett.* **74** (1995) 2626–2631 (1995) (cit. on p. 34).
- ³¹⁹⁷⁶⁴S. Abachi et al., *Observation of the top quark,*
³¹⁹⁸*Phys. Rev. Lett.* **74** (1995) 2632–2637 (1995) (cit. on p. 34).
- ³¹⁹⁹⁶⁵M. Czakon and A. Ferroglio, *Chinese Physics C* () 083104
³²⁰⁰(cit. on p. 36).
- ³²⁰¹⁶⁶P. Kant et al., *HatHor for single top-quark production: Updated*
³²⁰²*predictions and uncertainty estimates for single top-quark production in*
³²⁰³*hadronic collisions,* *Comput. Phys. Commun.* **191** (2015) 74–89 (2015)
³²⁰⁴(cit. on p. 38).
- ³²⁰⁵⁶⁷M. Aliev et al.,
³²⁰⁶*HATHOR – HAdronic Top and Heavy quarks crOss section calculatoR,*
³²⁰⁷*Comput. Phys. Commun.* **182** (2011) 1034–1046 (2011) (cit. on p. 38).
- ³²⁰⁸⁶⁸J. A. Aguilar-Saavedra,
³²⁰⁹*Single top quark production at LHC with anomalous Wtb couplings,*
³²¹⁰*Nucl. Phys. B* **804** (2008) 160–192 (2008) (cit. on p. 39).
- ³²¹¹⁶⁹J. Butterworth et al., *PDF4LHC recommendations for LHC Run II,*
³²¹²*J. Phys. G* **43** (2016) 023001 (2016) (cit. on pp. 41, 76).
- ³²¹³⁷⁰A. D. Martin, W. J. Stirling, R. S. Thorne and G. Watt,
³²¹⁴*Parton distributions for the LHC,* *Eur. Phys. J. C* **63** (2009) 189 (2009)
³²¹⁵(cit. on pp. 41, 77).
- ³²¹⁶⁷¹A. D. Martin, W. J. Stirling, R. S. Thorne and G. Watt,
³²¹⁷*Uncertainties on α_S in global PDF analyses and implications for*
³²¹⁸*predicted hadronic cross sections,* *Eur. Phys. J. C* **64** (2009) 653–680
³²¹⁹(2009) (cit. on p. 41).
- ³²²⁰⁷²H.-L. Lai et al., *New parton distributions for collider physics,*
³²²¹*Phys. Rev. D* **82** (2010) 074024 (2010) (cit. on p. 41).
- ³²²²⁷³R. D. Ball et al., *Parton distributions with QED corrections,*
³²²³*Nucl. Phys. B* **877** (2013) 290–320 (2013) (cit. on p. 41).
- ³²²⁴⁷⁴M. Aaboud et al., *Measurement of the Higgs boson mass in the*
³²²⁵ *$H \rightarrow ZZ^*$ → 4ℓ and $H \rightarrow \gamma\gamma$ channels with $\sqrt{s} = 13$ TeV pp collisions*
³²²⁶*using the ATLAS detector,* *Phys. Lett. B* **784** (2018) 345–366 (2018)
³²²⁷(cit. on p. 46).
- ³²²⁸⁷⁵A. M. Sirunyan et al.,
³²²⁹*A measurement of the Higgs boson mass in the diphoton decay channel,*
³²³⁰*Phys. Lett. B* **805** (2020) 135425 (2020) (cit. on p. 46).

- ⁷⁶F. Englert and R. Brout,
Broken symmetry and the mass of gauge vector mesons,
Phys. Rev. Lett. **13** (9 1964) 321–323 (1964) (cit. on p. 46).
- ⁷⁷P. W. Higgs, *Broken symmetries and the masses of gauge bosons*,
Phys. Rev. Lett. **13** (16 1964) 508–509 (1964) (cit. on p. 46).
- ⁷⁸G. S. Guralnik, C. R. Hagen and T. W. B. Kibble,
Global conservation laws and massless particles,
Phys. Rev. Lett. **13** (20 1964) 585–587 (1964) (cit. on p. 46).
- ⁷⁹G. Aad et al., *Observation of a new particle in the search for the Standard Model Higgs boson with the ATLAS detector at the LHC*,
Phys. Lett. B **716** (2012) 1–29 (2012) (cit. on pp. 46, 58).
- ⁸⁰S. Chatrchyan et al., *Observation of a New Boson at a Mass of 125 GeV with the CMS Experiment at the LHC*,
Phys. Lett. B **716** (2012) 30–61 (2012) (cit. on pp. 46, 58).
- ⁸¹T. Aaltonen et al., *Combined search for the standard model Higgs boson decaying to a bb pair using the full CDF data set*,
Phys. Rev. Lett. **109** (2012) 111802 (2012) (cit. on p. 46).
- ⁸²V. M. Abazov et al., *Combined Search for the Standard Model Higgs Boson Decaying to b b-bar Using the D0 Run II Data Set*,
Phys. Rev. Lett. **109** (2012) 121802 (2012) (cit. on p. 46).
- ⁸³D. de Florian et al., *Handbook of LHC Higgs Cross Sections: 4. Deciphering the Nature of the Higgs Sector*, **2/2017** (2016) (2016) (cit. on pp. 48, 49).
- ⁸⁴B. Mellado Garcia, P. Musella, M. Grazzini and R. Harlander,
CERN Report 4: Part I Standard Model Predictions, (2016) (2016) (cit. on p. 49).
- ⁸⁵A. Pich, *Electroweak Symmetry Breaking and the Higgs Boson*,
Acta Phys. Polon. B **47** (2016) 151, edited by M. Praszalowicz (2016) (cit. on p. 50).
- ⁸⁶M. Farina, C. Grojean, F. Maltoni, E. Salvioni and A. Thamm,
Lifting degeneracies in Higgs couplings using single top production in association with a Higgs boson, JHEP **05** (2013) 022 (2013) (cit. on pp. 50, 51).
- ⁸⁷S. Biswas, E. Gabrielli and B. Mele, *Single top and Higgs associated production as a probe of the Htt coupling sign at the LHC*,
JHEP **01** (2013) 088 (2013) (cit. on p. 50).
- ⁸⁸T. Appelquist and M. S. Chanowitz,
Unitarity Bound on the Scale of Fermion Mass Generation, Phys. Rev. Lett. **59** (1987) 2405, [Erratum: Phys. Rev. Lett. 60, 1589 (1988)] (1987) (cit. on p. 51).

- ⁸⁹ M. Aaboud et al., *Observation of Higgs boson production in association with a top quark pair at the LHC with the ATLAS detector*, *Phys. Lett. B* **784** (2018) 173–191 (2018) (cit. on p. 51).
- ⁹⁰ K. Skovpen, ‘First observation of the $t\bar{t}H$ process at CMS’, 11th International Workshop on Top Quark Physics (2018) (cit. on p. 51).
- ⁹¹ G. Aad et al., *Search for $H \rightarrow \gamma\gamma$ produced in association with top quarks and constraints on the Yukawa coupling between the top quark and the Higgs boson using data taken at 7 TeV and 8 TeV with the ATLAS detector*, *Phys. Lett. B* **740** (2015) 222–242 (2015) (cit. on p. 51).
- ⁹² V. Khachatryan et al., *Search for the associated production of the Higgs boson with a top-quark pair*, *JHEP* **09** (2014) 087, [Erratum: *JHEP* 10, 106 (2014)] (2014) (cit. on p. 51).
- ⁹³ F. Demartin, F. Maltoni, K. Mawatari and M. Zaro, *Higgs production in association with a single top quark at the LHC*, *Eur. Phys. J. C* **75** (2015) 267 (2015) (cit. on pp. 52–54).
- ⁹⁴ T. M. P. Tait and C. P. Yuan, *Single top quark production as a window to physics beyond the standard model*, *Phys. Rev. D* **63** (2000) 014018 (2000) (cit. on p. 54).
- ⁹⁵ S. Biswas, E. Gabrielli, F. Margaroli and B. Mele, *Direct constraints on the top-Higgs coupling from the 8 TeV LHC data*, *JHEP* **07** (2013) 073 (2013) (cit. on p. 54).
- ⁹⁶ CERN Web Page, *Our Member States*, (2022) <https://home.web.cern.ch/about/who-we-are/our-governance/member-states> (visited on 11/01/2022) (cit. on p. 58).
- ⁹⁷ T. Fazzini, G. Fidecaro, A. W. Merrison, H. Paul and A. V. Tollestrup, *Electron decay of the pion*, *Phys. Rev. Lett.* **1** (7 1958) 247–249 (1958) (cit. on p. 58).
- ⁹⁸ F. J. Hasert et al., *Observation of Neutrino Like Interactions Without Muon Or Electron in the Gargamelle Neutrino Experiment*, *Phys. Lett. B* **46** (1973) 138–140 (1973) (cit. on p. 58).
- ⁹⁹ P. M. Watkins, *Discovery of the w and 2 bosons*, *Contemporary Physics* **27** (1986) 291–324 (1986) (cit. on p. 58).
- ¹⁰⁰ D. Decamp et al., *Determination of the Number of Light Neutrino Species*, *Phys. Lett. B* **231** (1989) 519–529 (1989) (cit. on p. 58).

- 3309 ¹⁰¹G. Baur et al., *Production of anti-hydrogen*,
3310 *Phys. Lett. B* **368** (1996) 251–258 (1996) (cit. on p. 58).
- 3311 ¹⁰²G. D. Barr et al.,
3312 *A New measurement of direct CP violation in the neutral kaon system*,
3313 *Phys. Lett. B* **317** (1993) 233–242 (1993) (cit. on p. 58).
- 3314 ¹⁰³V. Fanti et al., *A New measurement of direct CP violation in two pion*
3315 *decays of the neutral kaon*, *Phys. Lett. B* **465** (1999) 335–348 (1999)
3316 (cit. on p. 58).
- 3317 ¹⁰⁴R. Aaij et al., *Observation of J/ψ Resonances Consistent with*
3318 *Pentaquark States in $\Lambda_b^0 \rightarrow J/\psi K^- p$ Decays*,
3319 *Phys. Rev. Lett.* **115** (2015) 072001 (2015) (cit. on p. 58).
- 3320 ¹⁰⁵S. Maury, *The Antiproton Decelerator: AD*,
3321 *Hyperfine Interact.* **109** (1997) 43–52 (1997) (cit. on p. 58).
- 3322 ¹⁰⁶R. Alemany et al.,
3323 *Summary Report of Physics Beyond Colliders at CERN*,
3324 (2019), edited by J. Jaeckel, M. Lamont and C. Vallée (2019)
3325 (cit. on p. 58).
- 3326 ¹⁰⁷R. Catherall et al., *The ISOLDE facility*, *J. Phys. G* **44** (2017) 094002
3327 (2017) (cit. on p. 58).
- 3328 ¹⁰⁸E. Gschwendtner et al., *AWAKE, The Advanced Proton Driven Plasma*
3329 *Wakefield Acceleration Experiment at CERN*,
3330 *Nucl. Instrum. Meth. A* **829** (2016) 76–82, edited by U. Dorda et al.
3331 (2016) (cit. on p. 58).
- 3332 ¹⁰⁹M. Aguilar et al.,
3333 *The Alpha Magnetic Spectrometer (AMS) on the International Space*
3334 *Station. I: Results from the test flight on the space shuttle*, *Phys. Rept.*
3335 **366** (2002) 331–405, [Erratum: *Phys.Rept.* **380**, 97–98 (2003)] (2002)
3336 (cit. on p. 59).
- 3337 ¹¹⁰T. J. Berners-Lee and R. Cailliau,
3338 *WorldWideWeb: proposal for a HyperText Project*, tech. rep.,
3339 CERN, 1990 (cit. on p. 59).
- 3340 ¹¹¹CERN Council holds special session on the Large Hadron Collider
3341 project, (1991) 3 p, Issued on 19 December 1991 (1991) (cit. on p. 59).
- 3342 ¹¹²T. S. Pettersson and P Lefèvre,
3343 *The Large Hadron Collider: conceptual design*, tech. rep., 1995
3344 (cit. on pp. 59, 62).
- 3345 ¹¹³S. Myers,
3346 *The LEP Collider, from design to approval and commissioning*,
3347 John Adams' memorial lecture, Delivered at CERN, 26 Nov 1990
3348 (CERN, Geneva, 1991) (cit. on p. 59).

- 3349 ¹¹⁴B. Müller, J. Schukraft and B. Wysłouch,
3350 *First Results from Pb+Pb Collisions at the LHC*,
3351 *Annual Review of Nuclear and Particle Science* **62** (2012) 361–386
3352 (2012) (cit. on p. 61).
- 3353 ¹¹⁵CERN Web Page, *The Large Hadron Collider*, (2022)
3354 <https://home.cern/science/accelerators/large-hadron->
3355 *collider* (visited on 11/01/2022) (cit. on p. 61).
- 3356 ¹¹⁶R. Steerenberg et al., ‘Operation and performance of the cern large
3357 hadron collider during proton run 2’,
3358 *10th international particle accelerator conference* (2019) MOPMP031
3359 (cit. on p. 61).
- 3360 ¹¹⁷by Rende Steerenberg and A. Schaeffer, *LHC Report: The LHC is full!*,
3361 (2018) (2018) (cit. on p. 61).
- 3362 ¹¹⁸*8th International Conference on High-Energy Accelerators*,
3363 CERN (CERN, Geneva, 1971) (cit. on p. 61).
- 3364 ¹¹⁹*LHC Machine*,
3365 *JINST* **3** (2008) S08001, edited by L. Evans and P. Bryant (2008)
3366 (cit. on pp. 61, 64).
- 3367 ¹²⁰*Radiofrequency cavities*, (2012) (2012) (cit. on p. 62).
- 3368 ¹²¹K. Long et al., *Muon colliders to expand frontiers of particle physics*,
3369 *Nature Phys.* **17** (2021) 289–292 (2021) (cit. on p. 63).
- 3370 ¹²²L Lari, H Gaillard and V Mertens,
3371 *Scheduling the installation of the LHC injection lines*, tech. rep.,
3372 CERN, 2004 (cit. on p. 64).
- 3373 ¹²³G. Aad et al.,
3374 *The ATLAS Experiment at the CERN Large Hadron Collider*,
3375 *JINST* **3** (2008) S08003 (2008) (cit. on pp. 64, 83, 87, 88, 92, 93).
- 3376 ¹²⁴S. Chatrchyan et al., *The CMS Experiment at the CERN LHC*,
3377 *JINST* **3** (2008) S08004 (2008) (cit. on p. 64).
- 3378 ¹²⁵A. A. Alves Jr. et al., *The LHCb Detector at the LHC*,
3379 *JINST* **3** (2008) S08005 (2008) (cit. on p. 65).
- 3380 ¹²⁶K. Aamodt et al., *The ALICE experiment at the CERN LHC*,
3381 *JINST* **3** (2008) S08002 (2008) (cit. on p. 65).
- 3382 ¹²⁷O. Adriani et al.,
3383 *The LHCf detector at the CERN Large Hadron Collider*,
3384 *JINST* **3** (2008) S08006 (2008) (cit. on p. 66).

- 3385 ¹²⁸O. Adriani et al.,
3386 *Technical design report of the LHCf experiment: Measurement of*
3387 *photons and neutral pions in the very forward region of LHC* (2006)
3388 (cit. on p. 66).
- 3389 ¹²⁹C. Alpigiani et al., *A Letter of Intent for MATHUSLA: A Dedicated*
3390 *Displaced Vertex Detector above ATLAS or CMS.*, (2018) (2018)
3391 (cit. on p. 67).
- 3392 ¹³⁰J. H. Yoo, *The milliQan Experiment: Search for milli-charged Particles*
3393 *at the LHC*, PoS **ICHEP2018** (2018) 520. 4 p, proceeding for ICHEP
3394 2018 SEOUL, International Conference on High Energy Physics, 4-11
3395 July 2018, SEOUL, KOREA (2018) (cit. on p. 67).
- 3396 ¹³¹A. Ball et al., *Search for millicharged particles in proton-proton*
3397 *collisions at $\sqrt{s} = 13$ TeV*, Phys. Rev. D **102** (2020) 032002 (2020)
3398 (cit. on p. 67).
- 3399 ¹³²V. A. Mitsou, *The MoEDAL experiment at the LHC: status and results*,
3400 J. Phys. Conf. Ser. **873** (2017) 012010, edited by B. Grzadkowski,
3401 J. Kalinowski and M. Krawczyk (2017) (cit. on p. 67).
- 3402 ¹³³G. Anelli et al.,
3403 *The TOTEM experiment at the CERN Large Hadron Collider*,
3404 JINST **3** (2008) S08007 (2008) (cit. on p. 67).
- 3405 ¹³⁴A. Ariga et al., *Technical Proposal for FASER: ForwArd Search*
3406 *ExpeRiment at the LHC*, (2018) (2018) (cit. on p. 67).
- 3407 ¹³⁵A. Ariga et al.,
3408 *Letter of Intent for FASER: ForwArd Search ExpeRiment at the LHC*,
3409 (2018) (2018) (cit. on p. 67).
- 3410 ¹³⁶*LHC computing Grid. Technical design report*,
3411 (2005), edited by I. Bird et al. (2005) (cit. on p. 67).
- 3412 ¹³⁷WLCG Web Page, *Resources*, (2022)
3413 <https://wlcg-public.web.cern.ch/resources> (visited on
3414 31/01/2022) (cit. on p. 68).
- 3415 ¹³⁸*ATLAS computing: Technical design report*,
3416 (2005), edited by G. Duckeck et al. (2005) (cit. on p. 67).
- 3417 ¹³⁹WLCG Web Page, *Tier centres*, (2022)
3418 <https://wlcg-public.web.cern.ch/tier-centres> (visited on
3419 31/01/2022) (cit. on pp. 68, 69).
- 3420 ¹⁴⁰W. Herr and B Muratori, *Concept of luminosity*, (2006) (2006)
3421 (cit. on pp. 70, 71).

- ³⁴²²¹⁴¹A. Hoecker, ‘Physics at the LHC Run-2 and Beyond’,
³⁴²³2016 European School of High-Energy Physics (2016)
³⁴²⁴(cit. on pp. 71, 72, 79).
- ³⁴²⁵¹⁴²M. Aaboud et al., *Luminosity determination in pp collisions at $\sqrt{s} = 8$ TeV using the ATLAS detector at the LHC*,
³⁴²⁶*Eur. Phys. J. C* **76** (2016) 653 (2016) (cit. on p. 71).
- ³⁴²⁸¹⁴³G. Aad et al., *ATLAS data quality operations and performance for 2015–2018 data-taking*, *JINST* **15** (2020) P04003 (2020) (cit. on p. 72).
- ³⁴³⁰¹⁴⁴*Luminosity determination in pp collisions at $\sqrt{s} = 13$ TeV using the ATLAS detector at the LHC*, tech. rep., CERN, 2019 (cit. on p. 72).
- ³⁴³²¹⁴⁵F. S. Cafagna, *Latest results for Proton-proton Cross Section Measurements with the TOTEM experiment at LHC*,
³⁴³³*PoS ICRC2019* (2021) 207 (2021) (cit. on p. 75).
- ³⁴³⁵¹⁴⁶Particle Data Group Web Page,
³⁴³⁶*Data files and plots of cross-sections and related quantities for hadrons*,
³⁴³⁷(2022) <https://pdg.lbl.gov/2021/hadronic-xsections/> (visited on
³⁴³⁸08/02/2022) (cit. on p. 76).
- ³⁴³⁹¹⁴⁷*Shrek*, 2001 (cit. on p. 81).
- ³⁴⁴⁰¹⁴⁸*CERN Council holds special session on the Large Hadron Collider project*, (1991) 3 p, Issued on 19 December 1991 (1991) (cit. on p. 79).
- ³⁴⁴²¹⁴⁹*ATLAS: technical proposal for a general-purpose pp experiment at the Large Hadron Collider at CERN*, LHC technical proposal
³⁴⁴³(CERN, Geneva, 1994) (cit. on p. 80).
- ³⁴⁴⁵¹⁵⁰A. collaboration, ‘First 2.36 TeV Collision Events recorded by the ATLAS experiment, December 8th and 14th, 2009’, 2009 (cit. on p. 80).
- ³⁴⁴⁷¹⁵¹G. Aad et al., *Measurements of the Higgs boson production and decay rates and constraints on its couplings from a combined ATLAS and CMS analysis of the LHC pp collision data at $\sqrt{s} = 7$ and 8 TeV*,
³⁴⁴⁸*JHEP* **08** (2016) 045 (2016) (cit. on p. 80).
- ³⁴⁵¹¹⁵²G. Aad et al., *Measurement of the top quark-pair production cross section with ATLAS in pp collisions at $\sqrt{s} = 7$ TeV*,
³⁴⁵²*Eur. Phys. J. C* **71** (2011) 1577 (2011) (cit. on p. 80).
- ³⁴⁵⁴¹⁵³G. Aad et al., *Evidence for Electroweak Production of $W^\pm W^\pm jj$ in pp Collisions at $\sqrt{s} = 8$ TeV with the ATLAS Detector*,
³⁴⁵⁵*Phys. Rev. Lett.* **113** (2014) 141803 (2014) (cit. on p. 80).
- ³⁴⁵⁷¹⁵⁴M. Aaboud et al., *Evidence for light-by-light scattering in heavy-ion collisions with the ATLAS detector at the LHC*,
³⁴⁵⁸*Nature Phys.* **13** (2017) 852–858 (2017) (cit. on p. 80).

- 3460 ¹⁵⁵M. Aaboud et al., *Search for the standard model Higgs boson produced*
- 3461 in association with top quarks and decaying into a $b\bar{b}$ pair in pp
- 3462 collisions at $\sqrt{s} = 13$ TeV with the ATLAS detector,
- 3463 Phys. Rev. D **97** (2018) 072016 (2018) (cit. on p. 80).
- 3464 ¹⁵⁶M. Aaboud et al., *Observation of $H \rightarrow b\bar{b}$ decays and VH production*
- 3465 *with the ATLAS detector*, Phys. Lett. B **786** (2018) 59–86 (2018)
- 3466 (cit. on p. 80).
- 3467 ¹⁵⁷S. Amoroso, *Precision measurements at the LHC*, tech. rep.,
- 3468 CERN, 2020 (cit. on p. 80).
- 3469 ¹⁵⁸H. Pacey, *EW SUSY Production at the LHC*, tech. rep., CERN, 2021
- 3470 (cit. on p. 80).
- 3471 ¹⁵⁹S. Das Bakshi, J. Chakrabortty, C. Englert, M. Spannowsky and
- 3472 P. Stylianou, *CP Violation at atlas in effective field theory*,
- 3473 Phys. Rev. D **103** (5 2021) 055008 (2021) (cit. on p. 80).
- 3474 ¹⁶⁰B. T. Carlson, *Dark Matter searches with the ATLAS detector*, (2020)
- 3475 (2020) (cit. on p. 82).
- 3476 ¹⁶¹J. L. Pinfold, *ATLAS and astroparticle physics*, Nucl. Phys. B Proc.
- 3477 Suppl. **175-176** (2008) 25–32, edited by K. S. Cheng et al. (2008)
- 3478 (cit. on p. 82).
- 3479 ¹⁶²N. D. Brett et al., *Discovery Reach for Black Hole Production*, (2009)
- 3480 (2009) (cit. on p. 82).
- 3481 ¹⁶³*ATLAS inner detector: Technical Design Report*, 1,
- 3482 Technical design report. ATLAS (CERN, Geneva, 1997) (cit. on p. 83).
- 3483 ¹⁶⁴G. Aad et al.,
- 3484 *The ATLAS Inner Detector commissioning and calibration*,
- 3485 Eur. Phys. J. C **70** (2010) 787–821 (2010) (cit. on p. 83).
- 3486 ¹⁶⁵M Capeans et al., *ATLAS Insertable B-Layer Technical Design Report*,
- 3487 tech. rep., 2010 (cit. on pp. 85, 86).
- 3488 ¹⁶⁶*Technical Design Report for the ATLAS Inner Tracker Pixel Detector*,
- 3489 tech. rep., CERN, 2017 (cit. on pp. 86, 88, 102).
- 3490 ¹⁶⁷ATLAS Experiment Web Page, *Detector and Technology*, (2022)
- 3491 <https://atlas.cern/discover/detector> (visited on 02/02/2022)
- 3492 (cit. on pp. 86, 89, 92, 96, 97).
- 3493 ¹⁶⁸F. Cavallari, *Performance of calorimeters at the LHC*,
- 3494 Journal of Physics: Conference Series **293** (2011) 012001 (2011)
- 3495 (cit. on pp. 88, 91, 92).
- 3496 ¹⁶⁹C. Grupen and B. Shwartz, ‘Calorimetry’, *Particle detectors*, 2nd ed.,
- 3497 Cambridge Monographs on Particle Physics, Nuclear Physics and
- 3498 Cosmology (Cambridge University Press, 2008) 230–272 (cit. on p. 90).

- 3499 ¹⁷⁰Particle Data Group Web Page, *π^0 Decay Modes*, (2022)
3500 <https://pdglive.lbl.gov/DataBlock.action?node=Q007TP> (visited
3501 on 02/02/2022) (cit. on p. 91).
- 3502 ¹⁷¹A. Tarek Abouelfadl Mohamed, ‘The lhc and the atlas experiment’,
3503 *Measurement of higgs boson production cross sections in the diphoton*
3504 *channel: with the full atlas run-2 data and constraints on anomalous*
3505 *higgs boson interactions*
3506 (Springer International Publishing, Cham, 2020) 61 (cit. on pp. 92, 93).
- 3507 ¹⁷²*ATLAS muon spectrometer: Technical design report*, (1997) (1997)
3508 (cit. on p. 93).
- 3509 ¹⁷³K. Ishii, *The ATLAS muon spectrometer*, PoS **HEP2001** (2001) 253,
3510 edited by D. o. Horváth, P. Lévai and A. Patkós (2001) (cit. on p. 94).
- 3511 ¹⁷⁴M Livan, *Monitored drift tubes in ATLAS*, tech. rep., CERN, 1996
3512 (cit. on p. 94).
- 3513 ¹⁷⁵G. Cattani, *The resistive plate chambers of the ATLAS experiment:*
3514 *performance studies*,
3515 *Journal of Physics: Conference Series* **280** (2011) 012001 (2011)
3516 (cit. on p. 95).
- 3517 ¹⁷⁶K. Nagai, *Thin gap chambers in ATLAS*, Nucl. Instrum. Meth. A **384**
3518 (1996) 219–221, edited by F. Ferroni and P. Schlein (1996)
3519 (cit. on p. 95).
- 3520 ¹⁷⁷*ATLAS magnet system: Technical Design Report, 1*,
3521 Technical design report. ATLAS (CERN, Geneva, 1997)
3522 (cit. on pp. 96, 97).
- 3523 ¹⁷⁸*ATLAS high-level trigger, data acquisition and controls: Technical*
3524 *design report*, (2003) (2003) (cit. on pp. 98, 99).
- 3525 ¹⁷⁹G. Aad et al., *Performance of the ATLAS Trigger System in 2010*,
3526 *Eur. Phys. J. C* **72** (2012) 1849 (2012) (cit. on p. 98).
- 3527 ¹⁸⁰*Technical Design Report for the Phase-II Upgrade of the ATLAS TDAQ*
3528 *System*, tech. rep., CERN, 2017 (cit. on p. 103).
- 3529 ¹⁸¹G. Aad et al., *The ATLAS Simulation Infrastructure*,
3530 *Eur. Phys. J. C* **70** (2010) 823–874 (2010) (cit. on p. 105).
- 3531 ¹⁸²P. Mato, *GAUDI-Architecture design document*, (1998) (1998)
3532 (cit. on p. 108).
- 3533 ¹⁸³L. Lista, ‘Practical Statistics for Particle Physicists’,
3534 *2016 European School of High-Energy Physics* (2017) 213
3535 (cit. on p. 125).

³⁵³⁶ **Summary of the results**

3537 **Recerca de la producció
3538 associada de bosó de Higgs i
3539 un quark top amb dos leptons i
3540 tau hadrònic a l'estat final**

3541 **1 Marc teòric**

3542 **1.1 El Model Estàndard**

3543 Maybe, I could translate this for the SM summary:
3544 <https://www.quantamagazine.org/a-new-map-of-the-standard-model->
3545 [of-particle-physics-20201022/](https://www.quantamagazine.org/a-new-map-of-the-standard-model-of-particle-physics-20201022/)

3546 **1.2 La física del quark top**

3547 **1.3 La física del bosó de Higgs**

3548 **2 L'experiment ATLAS del LHC al CERN**

3549 **2.1 El gran col·lisionador d'hadrons**

3550 **2.2 El detector ATLAS**

3551 **3 Mesura de la polarització del quark top al
3552 canal-*t***

3553 Mesura d'observables sensibles a la polarització del quark top

3554 **3.1 Selecció d'esdeveniments**

3555 **3.2 Estimació del fons**

3556 **3.3 Fonts d'incertesa**

3557 **3.4 Resultats**

3558 **4 Recerca de processos tH amb un estat final $2\ell + 1\tau_{\text{had}}$**

3560 **4.1 Selecció d'esdeveniments**

3561 **4.2 Estimació del fons**

3562 **4.3 Fonts d'incertesa**

3563 **4.4 Resultats**

3564 **5 Conclusions**

3565

3566 Contraportada

3567 The discovery of a Higgs boson by the ATLAS and CMS experiments
3568 in 2012 opened a new field for exploration in the realm of particle physics.
3569 In order to better understand the Standard Model (SM) of particle physics,
3570 it is imperative to study the Yukawa coupling between this new particle
3571 and the rest of the SM components. Among these, of prominent interest is
3572 the coupling of the Higgs boson to the top quark (y_t), which is the most
3573 massive fundamental particle and, consequently, the one with the strongest
3574 coupling to the Higgs

3575 The direct measurement of y_t is only possible at LHC via two associated
3576 Higgs productions; with a pair of top quarks ($t\bar{t}H$) and with single-top
3577 quark (tHq). While the $t\bar{t}H$ permits a model-independent determination of
3578 the magnitude of y_t , the only way of directly measuring its sign is through
3579 the tHq production. This is due to the fact that the two leading-order
3580 Feynman diagrams for tHq production interfere with each other depending
3581 on y_t sign. Current experimental constraints on y_t favour the SM predictions,
3582 even though an opposite sign with respect to the SM expectations is not
3583 completely excluded yet.

3584 In this work it is presented a search for the production of a Higgs boson in
3585 association with a single-top quark in a final state with two light-floavoured-
3586 charged leptons and one hadronically decaying tau lepton (named $2\ell+1\tau_{\text{had}}$
3587 channel). This analysis uses an integrated luminosity of 139 fb^{-1} of proton-
3588 proton collision data at centre-of-mass energy of 13 TeV collected by ATLAS
3589 during LHC Run 2.

3590 This search is exceptionally challenging due to the extremely small cross
3591 section of the tHq process (70 fb^{-1}) in general and, more particularly, the
3592 the $2\ell + 1\tau_{\text{had}}$ final-state channel, which only accounts for a 3.5% of the
3593 total tHq production.

3594 Because of this, the separation of the tHq signal events from back-
3595 ground events is done by means of machine-learning (ML) techniques using
3596 boosted-decision trees (BDT) to define both signal and control regions. The
3597 most most relevant background processes are those related to top-pairs pro-

3598 duction (such as $t\bar{t}$, $t\bar{t}H$, $t\bar{t}Z$ and $t\bar{t}W$), Z -boson plus jets and single-top
 3599 processes.

3600 Significant suppression of the background events with jets wrongly selec-
 3601 ted as leptons is achieved by demanding electrons and muons to pass strict
 3602 isolation requirements. Simultaneously, hadronic-tau leptons are demanded
 3603 to pass the requirement of the recurrent-neural-network-based discriminator
 3604 to reduce misidentifications from jets.

3605 The reconstruction of the events is also enhanced by similar ML methods
 3606 since in the scenario in which the light-flavour leptons have the same sign,
 3607 in principle, it is not possible to determine which lepton is originated from
 3608 the Higgs boson and which from the top quark.

3609 The possible observation of an excess of signal events with respect to
 3610 the SM predictions, would be a clear evidence of new physics in terms of
 3611 \mathcal{CP} -violating y_t coupling.

3612 Additionally, the contribution to the single-top-quark polarisation first
 3613 measurement is presented as well. In this other analysis the components of
 3614 the full polarisation vector of the top quark are measured taking advantage
 3615 of the peculiarities of the single-top-quark decay. Benefitting from the fact
 3616 that the top quark lifetime is smaller than the depolarisation timescale, the
 3617 decay products preserve the spin information of the top quark. Via angular
 3618 distributions, it is measured in the top-quark rest frame.